Hygroscopicity and cloud condensation nucleus activity of atmospheric aerosol particles at urban and forest sites and their contribution to cloud droplet formation

都市・森林域における大気エアロゾル粒子の吸湿性・雲凝結核活性およびそれらの雲粒形成への寄与

Kaori Kawana

川名　華織

A dissertation for the degree of Doctor of Science

Department of Earth and Environmental Sciences,

Graduate school of Environmental Studies, Nagoya University

（名古屋大学大学院環境学研究科地球環境科学専攻学位論文　博士（理学））

2015

要旨

大気中のエアロゾル粒子は太陽放射を直接吸収・散乱する事によって、また雲凝結核(CCN)として間接的に雲過程に作用することで、地球の放射収支に影響する。粒子のCCN活性を決定する因子の一つは吸湿性である。大気中における粒子の吸湿性の変化はCCN活性の変化をもたらす。例えば、黒色炭素や炭化水素様化合物からなる疎水性粒子は、水溶性成分(硫酸塩、硝酸塩など)の凝縮や、酸化やその他の化学的変質の過程を経ることによって、これらの粒子は親水性となり、CCNとなりうる。これまで吸湿性あるいは化学組成と粒径分布の情報を組み合わせてCCN数濃度を予測し、実測と比較する研究が室内実験および様々な大気環境下でなされてきた。先行研究では予測が実測をよく再現する事例(~10%)、両者に大きな不一致(>30%)が存在する事例の両方が存在し、予測と実測の不一致の程度は様々である。都市域はエアロゾル粒子、特に有機物を含む低吸湿性粒子の強い供給域である。しかし、CCNおよび雲粒形成に対する吸湿性の重要性について、吸湿性の測定データに基づいて定量的に研究した例はほとんど存在しない。森林域は生物起源二次有機エアロゾル(BSOA)の主要な発生源である。北欧の亜寒帯林におけるいくつかの研究では、新粒子生成(NPF)に伴うBSOAの吸湿性、組成の変化や、そのCCN活性との関連性が報告されているが、温帯のアジア域における観測・報告例はほとんど存在しない。本研究では、エアロゾル粒子のCCN活性およびCCN、雲粒数濃度を規定する要因の解明を目的として、都市域および森林域において大気測定を行った。そして都市大気エアロゾル、森林大気エアロゾルの粒径別の吸湿性とCCN活性の特徴づけを行った。また、粒子の吸湿性パラメータを吸湿成長度、CCN活性化粒径からそれぞれ算出し、水蒸気未飽和条件と過飽和条件下における粒子の吸湿性の違いや有機物の吸湿性について考察した。そして有機物の吸湿性、および吸湿性の時間変動や粒径依存性がCCN数濃度にどの程度影響を及ぼすかを評価した。

2009年9月に行われた名古屋における都市大気エアロゾルの観測では、相対湿度(RH)85%における吸湿成長度分布は低吸湿性粒子と高吸湿性粒子からなる二峰性を示した。観測中、エイトケンモードは有機物に富んだ粒子が多く存在した。RH85%における吸湿成長パラメータκは24–359 nmで0.17–0.33であり、微小粒子は吸湿性が低く粒径が増加するほど吸湿性が高かった。有機物の吸湿性パラメータは0.11–0.19であり、有機物はある程度の吸湿性を持つことが示唆された。水蒸気過飽和条件下(RH: >100%)における粒子の吸湿性は未飽和条件下(RH: 85%)における粒子の吸湿性より37%高く、原因として表面張力低下、吸湿性パラメータの溶質濃度依存性、未飽和条件における不溶な物質の存在、溶質の希釈に伴う水の活量係数の変化、粒子の非球形性が示唆された。37%の差異のうち無機物

による寄与を補正しても、28%の差異が残存する。この結果は、過飽和条件下における粒子の吸湿性の増加に有機物の大きな寄与がありうることを示している。CCN数濃度を予測し、実測値と比較した検討では、有機物を完全に不溶とした場合、予測値は実測値より45%–64%過小評価だった。一方、本研究で算出された有機物の吸湿性を考慮した場合、予測値は実測値と17%以内で一致した。また粒子の吸湿性について、単純化された時間・粒径平均値を適応した場合、予測値は実測値に対して30%以内で一致した。一方、時間・粒径別の吸湿性の違いを考慮した場合、予測値は実測値と19%以内で一致し、予測の実測再現性に改善が見られた。これらの結果は都市大気エアロゾルの場合、有機物の吸湿性および時間・粒径の違いによる吸湿性の変動がCCN数濃度に影響することを示している。

2010年8月に行われた和歌山における森林大気エアロゾルの観測では、湿度85%における吸湿成長度分布は平均的に広がりをもつ一山分布を示した。観測期間は粒径分布の解析に基づき、新粒子生成(NPF)イベント期間とNPFが顕著でない期間に分類された。新粒子生成が顕著でない前半期間における吸湿性分布は一日を通じて類似の分布を示し、時間帯や粒径による違いは明確でなかった。CCN活性化粒径やCCN数濃度にも顕著な日周期性はみられなかった。一方、新粒子生成が顕著だった後半期間における吸湿性分布は明確な日周期パターンを示し、時間帯や粒径による違いも大きかった。9-21時の時間帯では、エイトケンモードにおいて微小な低吸湿性粒子が多く存在し(κ~0.1)、24–359 nmの吸湿成長度は、前半期間に比べて30%低下した。観測された低いκは室内実験生成の純粋な生物起源二次有機エアロゾル(BSOA)の報告値と似た値だった。これらの結果はこの低吸湿性粒子群が新粒子として形成されたBSOAであり、それらが既存粒子の吸湿性の低下に寄与したことを示唆している。一方、21-9時の時間帯では、高吸湿性粒子が多く存在し（κ~0.35)、24–359 nmの吸湿成長度は、前半期間に比べて15%増加した。全粒径範囲でみられた粒子の吸湿性の増加の原因として、粒子のエイジング、液相におけるWSOMの増加、大きな粒径における海洋性起源の高吸湿性粒子の流入が挙げられる。また、粒子の吸湿成長度・吸湿成長度分布の変化と共に、9-21時にはCCN活性化粒径の増大とCCN活性化割合の低下が、21-9時にはCCN活性化粒径の低下とCCN活性化割合の増大が観測され、低吸湿な微小粒子の生成とその成長による高吸湿性粒子の生成がCCN活性に影響したことが示唆された。BSOAの生成が顕著に見られた9-21時の、エイトケンモードにおける粒子の吸湿性パラメータは0.17, BSOAの吸湿性パラメータは0.13であり、この値は室内実験および先行研究で報告されたBSOAの吸湿性パラメータ値に近かった。過飽和条件下における粒子の吸湿性は未飽和条件下における粒子の吸湿性と10%以内で一致し、過飽和条件における有機物や低吸湿性粒子による吸湿性への寄与は小さいことが示唆された。CCN数濃度を予測し、実

測値と比較した検討では、単純化された時間・粒径平均値を用いた予測値は実測とよく一致した(+12%, *r*: 0.90)。この結果は森林内で生成しエイジングした、あるいはバックグラウンド大気中に存在する高吸湿性粒子のCCN数濃度への寄与が大きい事を示している。

粒子の吸湿性と CCN 活性、雲粒生成の関連性をより詳細に理解するために、2010 年に名古屋で都市大気エアロゾルの観測を行った。同観測では粒径別吸湿成長度分布に加えて、一定の *g* をもつ、選別された粒子群の CCN/CN 比が測定された。同観測で取得された吸湿成長度分布は 2009 年の名古屋観測と同様に、低吸湿性と高吸湿性モードからなる二峰性を示した。粒子のそれぞれの *g* から CCN 活性化粒径を予測し、実測と比較したところ、高吸湿性粒子(*g*: 1.25, 1.4)の場合両者は 12%以内で一致したが、低吸湿性粒子(*g*: 1.0, 1.1)の場合、両者により大きな差異(16–41%)が見られた。この結果は 2009 年の名古屋観測と同様に、未飽和・過飽和条件下における粒子の吸湿性の差異に、低吸湿性粒子が大きく寄与することを示している。さらに吸湿性別粒子の CCN および雲粒生成への寄与を調べるため、雲パーセルモデルを用いて吸湿成長度分布から CCN 数濃度、雲粒数濃度、雲粒有効半径が見積もられた。上昇速度が高い条件(>1.0 m s^{-1})下では、全ての吸湿性の粒子を考慮した場合、低吸湿性粒子を含めず高吸湿性粒子($g \geq 1.25$)のみが雲粒形成に寄与するとみなした場合に比べて、CCN、雲粒数濃度はそれぞれ平均で 27%、18%増加した。雲粒有効半径は 5%減少した。この結果は都市域に多く存在する低吸湿性粒子の存在が CCN、雲粒数濃度に大きく寄与し、また小さな雲粒生成をもたらす事を示している。

Abstract

Aerosol particles in the atmosphere affect global climate directly by absorbing and scattering solar radiation and indirectly by acting as cloud condensation nuclei (CCN). One of the factors that determine the CCN activation of particles is hygroscopicity. The hygroscopicity of particles changes in the atmosphere, which results in the changes in the CCN activity. For example, hydrophobic particles composed of BC or HOA become hydrophilic and act as CCN after condensation of hygroscopic secondary particles (e.g., sulfate and nitrate) and oxidation, and other chemical transformation. In previous laboratory studies and atmospheric observation studies, CCN number concentrations (N_{CCN}) were predicted from a combination of hygroscopicity (or chemical composition) of particles and the number-size distributions, and were compared to those measured. Previous studies show that the predicted N_{CCN} agreed (~10%) or disagreed (>30%) to the measured and the degrees of disagreements were various. Urban areas have a large source of aerosol particles, in particular less hygroscopic particles containing organics. However, there are few studies in which the importance of hygroscopicity on CCN and cloud droplet formation were analyzed quantitatively based on the observed data of hygroscopicity. Forest areas have a large source of biogenic secondary organic aerosol (BSOA). Whereas some studies in the boreal forest sites in Northern Europe indicate the changes of hygroscopicity and chemical composition with new particle formation and the relationship to the CCN activity, there are only few reports about the changes for the forest sites in temperate zone in Asia. In this study, to better understand the CCN activity of particles and factors controlling the number concentrations of CCN and cloud droplets, atmospheric observations were performed at urban and forest sites. The size-resolved hygroscopicity and CCN activity of urban and forest aerosols were characterized. Further, hygroscopic parameter κ of the particles were derived from the hygroscopic growth factors (g) and CCN activation diameters (d_{act}). Then, the differences of particle hygroscopicity under sub- and super-saturated conditions and the hygroscopicity of organics were analyzed and discussed. The influences of the hygroscopicity of organics and variations of g with time and particle size on N_{CCN} were assessed.

From observation of urban aerosols over Nagoya in 2009, the g distributions at 85% relative humidity (RH) was on average bimodal with less and more hygroscopic modes. Organic-rich particles were dominant in the Aitken mode range. The κ of particles ranged of 0.17–0.33 at 24–359 nm; smaller particles were less hygroscopic and larger particles were more hygroscopic on average. The mean κ of organics (κ_{org}) was 0.11–0.19, suggesting that organics was moderately hygroscopic. The κ values calculated from CCN activation curves under super-

saturated conditions (RH: >100%) were 37% higher than those derived from g under sub-saturated conditions (RH: 85%). Possible reasons for the discrepancy were a reduction of surface tension, the presence of sparingly soluble materials, the dependence of the activity coefficient of water on the solution concentration, and particle asphericity. The 28% difference of the 37% difference is not explained by the difference of κ of inorganics under sub- and super-saturated conditions, suggesting a large contribution of organics to the difference. In the CCN closure, while the N_{CCN}/N_{CN} values predicted from the composition are underestimated largely if organics are assumed to be insoluble (differences: −64% to −45%), they agree to the measured better if κ_{org} of 0.11 or 0.19 is applied (differences: −17% to +14%). The N_{CCN}/N_{CN} values predicted from the hygroscopicity show fair agreement to the measured if a single averaged g is applied to all particles (differences: −30% to +10%). The agreements improve if size- and time-resolved g or size- and time-resolved g distributions are used (differences: −19% to −3%). The results demonstrate the importance of the hygroscopicity of organics and the dependence of g of particles with time and particle size for CCN number concentrations in the urban atmosphere.

From observation of aerosol particles over a forest site in Wakayama in 2010, the g distributions at 85% RH was on average broad and unimodal. The observation period was categorized to new particle formation (NPF) event days and non-event days, based on the analysis of number-size distributions. On non-event days, g distributions showed similar distributions throughout a day and the differences with time sections and particle size were not clear. The d_{act} and N_{CCN} were almost constant throughout a day. By contrast, on NPF event days, g distributions showed a clear diurnal pattern and the differences with time sections and particle size were large. During 0900-2100 JST, fine less-hygroscopic particles (κ~0.1) were dominant in the Aitken mode range and the mean g at 24–359 nm were ~30% lower than those on non-event days. The observed κ was similar to that of laboratory-generated pure BSOA, indicating that low hygroscopic particles in the Aitken mode range were newly-formed BSOA and they contributed significantly to the decrease of the hygroscopicity of pre-existing particles. On the other hand, during 2100-0900 JST, large and more hygroscopic particles (κ~0.35) were dominant and the mean g at 24–359 nm were ~15% higher than those during non-event days. Possible reasons for the increase of particle hygroscopicity were the aging of particles, the production of water soluble organic matter, and the influence of the inflow of maritime aerosols at large diameter. The CCN activation of the aerosols during 0900-2100 JST was characterized by the small activated fraction and the large d_{act} and those during 2100-0900 JST was characterized by the large activated fraction and the small d_{act} corresponding to the changes of particle hygroscopicity. The result suggests that formation of new particles with less

hygroscopicity and their conversion to more hygroscopic particles by aging affect the CCN activation behavior of the aerosols. The κ calculated for particles in the Aitken mode on NPF event days from g and d_{act} were 0.17 and 0.17, respectively, and κ of newly-formed BSOA was calculated to be 0.13. The calculated κ was similar to the reported κ values of laboratory-generated pure BSOA. The difference of κ values under sub- and super-saturated conditions was within 10% on average, suggesting that the contribution of organics or less hygroscopic particle to the increase of particle hygroscopicity under super-saturated conditions was small. The predicted N_{CCN}/N_{CN} using size- and time-averaged mean g during the observation period agreed well to the measured N_{CCN}/N_{CN} (+12%, r~0.90). The results suggest that locally-formed BSOA particles after aging and particles in the background aerosol contributed to the CCN number concentrations largely.

To understand the relationship of the hygroscopicity of particles and their CCN activity, and cloud droplet formation in detail, another aerosol observation was performed in Nagoya in 2010. Size-resolved measurements of the ratios of CCN to CN for particles with selected different g were performed, in addition to the measurements of g distributions at 85% RH. The obtained g distributions were bimodal with less and more hygroscopic modes on average, as the aerosols observed in 2009. The d_{act} were predicted from the respective g of particles and were compared to the measured. While the differences between the CCN activation diameters predicted from g ($d_{act,g85}$) and those measured ($d_{act,CCN}$) were within 12% for more hygroscopic particles (g: 1.25 and 1.4), the differences were larger (16%–41%) for less hygroscopic particles (g: 1.0 and 1.1). The result suggests that less hygroscopic particles contributed to the difference of hygroscopicity of particles under sub- and super-saturated conditions described above. The number concentrations of CCN and cloud droplets (N_{cd}), and the effective radius of cloud droplets (R_{eff}) were estimated from the g distributions using a cloud parcel model. With high updraft velocity (>1.0 ms^{-1}), the presence of less hygroscopic particles in addition to more hygroscopic particles ($0.8 \leq g \leq 2.2$) led to 27% and 18% increase of N_{CCN} and N_{cd}, respectively, and 5% decrease of R_{eff} as compared to the case that only more hygroscopic particles ($g \geq 1.25$) were present. These results suggested that the presence of less hygroscopic particles can contribute substantially to N_{CCN} and N_{cd} and can lead to smaller cloud droplets.

Contents

1. Introduction

1.1. Climate effect by aerosol particles

Aerosol particles in the atmosphere affect global climate directly by absorbing and scattering solar radiation, and indirectly by acting as cloud condensation nuclei (CCN). The radiative forcing by aerosol particles, in particular by the influence of aerosols on clouds (indirect effects), has large uncertainty and the assessment of future climate change remains a challenge [IPCC, 2013]. The increases of the number concentrations of CCN (N_{CCN}) and cloud droplet (N_{cd}) and the decrease of cloud droplet effective radius (R_{eff}) lead to the increase of cloud albedo and the cooling of the atmosphere, the so-called first indirect effect [*Twomey*, 1977]. Further, the increase of small cloud droplets lead to prolonged cloud lifetime and precipitation reduction, the so-called second indirect effect [*Albrecht*, 1989].

The sources of aerosol particles are mainly categorized as anthropogenic (motor vehicles, industrial activity, and others) and natural (ocean, volcanic activity, and others). The emission of anthropogenic aerosols and their contribution to the climate have increased [*Solomon et al.,* 2007]. Some satellite observations have indicated that cloud droplets in clouds affected by the smoke of biomass burning and anthropogenic activity did not grow even at high altitude, and that precipitation was suppressed as compared to smoke- or plume-free clouds [*Rosenfeld*, 1999; 2000]. Some model calculations have also indicated that the increase of the proportion of anthropogenic aerosols leads to changes in surface air temperature and precipitation [*Ramanathan,* 2001; *Menon et al.*, 2002; *Takemura et al.*, 2005]. Further observation of the burden and the property of both natural and anthropogenic aerosols is required to understand climate change.

1.2. Hygroscopic property of aerosol particles and relation to CCN activity

Hygroscopicity is an important property for the growth of particles by water uptake. Further, the changes of particle hygroscopicity tightly link to the reactivity. The measurement of particle hygroscopicity has been performed using a hygroscopicity tandem differential mobility analyzer (HTDMA) (*Rader and McMurry*, 1986). By the use of the HTDMA, the hygroscopicity of particles in the Aitken and accumulation modes is observed, which provides information on the aerosol mixing state. As an index of the hygroscopicity of particles and chemical components, a hygroscopicity parameter κ [*Petters and Kreidenweis,* 2007] is widely used. The κ values of particles are obtained from the hygroscopic growth factor (g) measured using the HTDMA under sub-saturated water vapor conditions. Further, they are obtained from the CCN activation diameter (d_{act}) measured using a CCN counter under super-saturated conditions. The κ values of chemical components can also be obtained in the case that the chemical composition of particles as well as their κ values are available. The κ parameterization of particle hygroscopicity has been performed in model calculations to evaluate N_{CCN}, N_{cd}, and radiative forcing by aerosols [*Liu and Wang,* 2012].

The hygroscopic growth and subsequent CCN activation of aerosol particles are governed by the chemical composition as well as the size. Among chemical components in atmospheric aerosols, black carbon (BC) and hydrocarbon-like organic aerosol (HOA) compounds are less hygroscopic, secondary organic aerosol (SOA) compounds are moderately hygroscopic, and inorganic salts are highly hygroscopic [*Andreae and Rosenfeld,* 2008]. Changes in the mixing state of chemical components lead to changes in particle hygroscopicity: hydrophobic particles, such as BC or HOA, become

hydrophilic and act as CCN after the condensation of hygroscopic secondary components (e.g., sulfate or nitrate). Additionally, oxidation and other chemical transformation lead to changes in particle hygroscopicity [*Petters et al.*, 2006; *McMeeking et al.,* 2011]. These processes affect particle hygroscopicity and may directly change the total CCN number concentrations. Moreover, the processes may also indirectly affect the abundance of CCN by enhancing aqueous phase reactions that form secondary compounds and by influencing the degree of wet deposition of particles.

1.3. Theory of hygroscopic growth and CCN activation of particles

The growth and CCN activation of particles are explained by Köhler equation (Köhler, 1936), with the saturation ratio of water vapor and the droplet diameter (see chapter 2). The CCN activation of particles under water super-saturated conditions is represented by the theoretical activation curve that considers the Kelvin effect (the increase of the equilibrium water vapor pressure resulting from the curved liquid-vapor interface) and the Raoult effect (the decrease of the equilibrium water vapor pressure by the presence of solute). The diameter at the maximum in the curve is called a critical diameter (D_{crit}). The SS condition corresponding to the saturation ratio at the maximum in the curve is called a critical supersaturation (S_{crit}).

1.4. CCN closure study

To assess the relationship between CCN activation of aerosols and their properties, the characteristics of CCN activation (N_{CCN}, d_{act}, and S_{crit}) were predicted from the hygroscopicity/chemical composition and the number-size distributions based on the Köhler theory, and were compared to the measured values, which is called CCN

closure study. In early laboratory studies, CCN activation was investigated for model particles whose physical and chemical parameters (i.e., molecular weight, density, ratios of mole) and composition (inorganic salt, organic, and mixtures of organic and inorganic salt) are known, which revealed non-ideal behavior of particles composed of organics or organic-inorganic salts. The effects caused by organics lead to both the increase and the decrease of CCN activity of particles and they often lead to the difference between predicted and measured values. For example, the surface tension reduction by surfactants leads to a decrease of S_{crit} and an increase in N_{CCN}. By contrast, the presence of solid core and low solubility components, and low accommodation coefficient of water by the film-forming compounds suppress activation and lead to a decrease in N_{CCN} [*Shulman et al.*, 1996; *Bilde et al.*, 2004; *Broekhuizen et al.*, 2004; *Abbatt et al.*, 2005; *Henning et al.*, 2005; *Sjogren et al.*, 2007].

In the last several decades, CCN closure was performed for atmospheric aerosol particles in addition to laboratory-generated model particles. The degrees of the agreement or disagreement and the reasons for the disagreement were discussed for different environments: urban [*Lance et al.,* 2009; *Asa-Awuku et al*., 2011], remote [*Chang et al.,* 2007], forest [*Rissler et al.,* 2004], ocean [*Mochida et al.,* 2011], polar region [*Lathem et al.,* 2013], and high elevation [*Jurányi et al.,* 2010] sites. In previous studies, the degrees of the difference of the predicted and measured values were various; they agreed (~10%) [*Jurányi et al.,* 2011; *Bougiatioti et al.,* 2009, 2011] or disagreed (>30%) [*Gasparini et al.,* 2006; *Vestin et al.,* 2007; *Irwin et al.,* 2011]. The various degrees of discrepancy between predicted and measured values shed light on the importance to understand the following three key subjects that relate to CCN activation.

One of the key subjects is the hygroscopicity of organics. It is important because

the prediction of N_{CCN} and that of aerosol indirect radiative forcing are sensitive to the hygroscopicity of organics if the fraction of organics in aerosols is large [*Wang et al.,* 2008; *Mei et al.,* 2013a]. The hygroscopicity parameter of organics (κ_{org}) can be calculated from the hygroscopicity and composition of particles, by regression analyses for particle hygroscopicity versus the mass fractions of organics [*Shinozuka et al.,* 2009; *Rose et al.,* 2011] or by analyzing the hygroscopicity and volume fractions of chemical components based on the Zdanovskii-Stokes-Robinson (ZSR) mixing rule [*Petters and Kreidenweis,* 2007]. The estimated κ_{org} for atmospheric aerosol particles is variable: <0.1 for fresh HOA and biomass burning OA (BBOA) [*Petters and Kreidenweis*, 2007; *Martin et al.,* 2011], ~0.1–0.2 for SOA [*Mei et al.,* 2013b], and ~0.2–0.3 for water soluble organic matter [*Asa-Awuku et al.,* 2010]. To date, the relation of the κ_{org} values and the types of organics is not well understood. Although correlations of κ_{org} to the O/C ratio or the signal of m/z 44 in the total signal of OA (f_{44}), both of which relate to the degree of oxygenation and were obtained using an aerosol mass spectrometer (AMS), were reported from laboratory and field studies [*Aiken et al.,* 2008; *Jimenez et al.,* 2009; *Chang et al.,* 2010], the degrees of correlations and the slopes of the regression lines largely differed among studies [*Duplissy et al.,* 2011; *Moore et al.,* 2011; *Alfarra et al.,* 2013; *Lathem et al.,* 2013; *Mei et al.,* 2013a, 2013b].

The second subject to investigate is the difference of particle hygroscopicity under sub- and super-saturated conditions. Whereas some studies report that particle hygroscopicity under sub- and super-saturated conditions agreed (within 30%) [*Dupllisy et al.,* 2008; *Carrico et al.,* 2008], those in other studies disagreed (>30%). Possible reasons for the disagreements include a reduction of surface tension, the presence of sparingly soluble materials, the dependence of the activity coefficient of water on the

solution concentration [*Wex et al.,* 2009; *Good et al.,* 2010a, 2010b]. These factors may largely be attributed to organics, and their contributions are difficult to determine from theories. This is because a large fraction of organics (~80%) cannot be identified at the molecular level, although their chemical and physical properties should strongly depend on the species.

Furthermore, the contribution of size, chemical composition, and mixing state to CCN number concentrations is among the key subjects. Some studies suggest that number-size distributions are more important than the composition and the solubility of organics for the prediction of N_{CCN} [*Ervans et al.,* 2007] and that the CCN activation is well represented using an average κ [*Rose et al.,* 2010, 2011]. By contrast, some other studies suggest that considering of size- and time-dependent κ is necessary for the consistency of CCN closure [*Kammermann et al.,* 2010; *Kim et al.,* 2011].

1.5. Importance of atmospheric aerosol particles at an urban area

Urban areas are regarded as a large source of anthropogenic aerosol particles, according to the satellite observation and emission inventory calculations. The contribution of urban aerosol particles to N_{CCN} may be large because of large emission of N_{CN}. However, prediction of N_{CCN} in urban sites is more difficult than that in other sites in most cases. One possible reason is that the properties of aerosols (chemical composition, hygroscopicity, and mixing state) are complicated and they frequently change depending on the aging process and particle emission in an urban site. *Ervens* et al. [2010] report that the influence of the consideration of chemical properties on N_{CCN} were assessed at six different locations (urban and remote site) and suggest that the size-resolved chemical properties (composition or hygroscopicity) of particles and organics

and mixing state information were needed for the prediction of N_{CCN} in the environments near sources (e.g., urban sites), whereas N_{CCN} can be predicted without the detailed chemical properties and mixing state in remote sites. In the case of urban aerosols, the variations of chemical components, hygroscopicity, and mixing state may greatly affect CCN closure. *Wex et al.* [2010] reported that considering externally mixed conditions in addition to size-resolved chemical composition is necessary for agreement between the prediction and the measurement in the presence of less- and more-hygroscopic modes in urban environments. However, there is also a report that the agreement between the prediction and the measurement is independent of the mixing state assumption [*Fors et al.,* 2011]. To date, different types of assumptions have been suggested for the agreement between predicted and measured N_{CCN} values of urban aerosols, and the cause of the difference is unclear. Hence, further investigation is required to better understand what factors contribute to CCN number concentrations.

1.6. Importance of atmospheric aerosol particles in forest areas

Forests constitute a part of the Earth's ecosystem and play an important role in the atmosphere as a main source of biogenic secondary organic aerosol (BSOA) particles formed by the photochemical oxidation of biogenic volatility organic compounds (BVOCs). The series of aerosol processes in forest areas, starting from the oxidation of BVOC and the formation of SOA, followed by the growth to CCN and cloud droplets, and deposition by precipitation, are important for climate [*Kulmala et al.,* 2004; *Andreae and Rosenfeld,* 2009; *Pöschl et al.,* 2010; *Martin et al.,* 2010]. Whereas BSOA was regarded to contribute to a large part of the total SOA flux on a global scale [*Kanakidou et al.,* 2005; *Hallquist et al.,* 2009], the estimate of the amount of SOA has

large uncertainty. The SOA flux estimated from the model calculation is largely different from that observed [*Volkamer et al.,* 2006], which have been attributed to the underestimation of anthropogenic SOA flux [*Spraclen et al.,* 2011] and the SOA yield [*Song et al.,* 2007; *Dzepina et al.,* 2009], and the contribution of isoprene [*Henze and Seinfeld,* 2006].

The hygroscopicity and CCN activity of BSOA formed from BVOCs have been investigated in laboratory studies under different conditions (e.g., NOx concentrations and methods of particle generation) [*VanReken et al.,* 2005; *Huff Hartz et al.,* 2005; *Varutbangkul et al.,* 2006; *Engelhart et al.,* 2008, 2011; *Lang-Yona et al.,* 2010]. Previous studies showed that laboratory-generated BSOA is slightly hygroscopic with g of ~1.1 and κ of ~0.1–0.2. The κ values of atmospheric forest aerosols were calculated to be 0.1–0.2 [*Gunthe et al.,* 2009; *Dusek et al.,* 2010; *Cerully et al.,* 2011; *Sihto et al.,* 2011; *Levin et al.,* 2014]. The changes of the hygroscopicity and CCN activity of aerosol particles through photochemical aging was investigated based on laboratory experiments, and contrasting results were obtained from different studies: a decrease in d_{act} with an increase in f_{44} [*Huff Hartz et al.,* 2005; *Engelhart et al.,* 2008, 2011] or an increase in d_{act} [*VanReken et al.,* 2005]. Although some laboratory studies showed that particle hygroscopicity κ changed by aging processes with the increase of f_{44} or O/C, there is no comprehensive view on the changes; the sensitivity of κ to the increase of f_{44} or O/C are various depending on the initial concentrations of VOC and NO_x, the presence/absence of seed particles [*King et al.,* 2009; *Alfarra et al.,* 2012] and the type of precursor BVOC [*Frosch et al.,* 2013]. Moreover, there are also some reports that κ is insensitive to f_{44} or O/C [*Alfarra et al.,* 2013]. *Engelhart et al.* [2008, 2011] suggest that BSOA aged by photochemical reactions partly contributed to WSOC (~30%), and that

they should have enhanced the soluble fraction and the hygroscopicity of particles. So far, the change of hygroscopicity and CCN activity with aging processes were investigated mainly under controlled conditions in laboratories, and investigations of the changes in the atmosphere are limited.

Some studies on forest aerosols showed that the chemical and physical properties of aerosols were influenced largely by new particle formation (NPF) events. Frequent NPF events in some forest areas have been reported (e.g., in the boreal forest of Hyytiälä in North Europe). It has also been reported that newly formed particles may largely contribute to the increase of the mass and number concentrations of aerosol particles (N_{CN}) and N_{CCN} [*Turnved et al.,* 2006; *Riipinen et al.,* 2011]. *Sihto et al.* [2011] reported based on atmospheric observation that newly formed particles contributed to 70%–110% increase of $N_{CCN,}$ compared to those during non-event days. Previous studies showed that particles formed by nucleation were grown up rapidly by condensation of sulfuric acid and organic vapors with the changes of particle size and their hygroscopicicty and CCN activity [*Hämeri et al.,* 2001; *Kulmala et al.,* 2001; *Boy et al.,* 2004; *Ehn et al.,* 2007]. Model calculations also showed the large contribution of newly-formed particles to N_{CCN}, based on the model estimation [*Pierce et al.,* 2007; *Spracklen et al.,* 2008; *Yu and Luo,* 2009; *Merikanto et al.,* 2009], and based on results from observations [*Slowik et al.,* 2010; *Pierce et al.,* 2012; *Westervelt et al.,* 2014]. Additionally, NPF influences on cloud droplet number concentrations and cloud albedo [*Makkonen et al.,* 2009; *Wang and Penner,* 2009], resulting in the radiative forcing. The increase of N_{CCN} from newly-formed particles was estimated to be ~50%, although the degree of their contribution was different depending on the mechanism of NPF (e.g., water-sulfuric acid binary nucleation, water-sulfuric acid-ammonia ternary nucleation,

and ion-induced nucleation) and the conditions during NPF events (e.g., initial gaseous concentrations, growth rates, condensation rates, and coagulation rates).

Understanding the state of SOA by in-situ observation and modeling studies, and the relationship between BSOA and CCN activity (i.e., their contribution to N_{CCN}) is a critical task at present. The investigation of the hygroscopicity, CCN activity, and chemical composition of aerosol particles and newly-formed BSOA were performed in North and South America and Europe and in laboratories under controlled conditions. However, there are few reports in Asia [*Irwin et al.,* 2011; *Miyazaki et al.,* 2012a, b; *Jung et al.,* 2013]. As far as I know, for Asian forests, there is no report on the changes of the hygroscopicity and CCN activity and the κ of BSOA with the formation of new particles and their subsequent growth, and on their contribution to N_{CCN}. Hence, an observation study focusing on the hygroscopicity and CCN activity of forest aerosols and BSOA therein is important.

1.7. **Investigation of cloud droplet activation based on aerosol properties**

The influences of the number-size distributions, hygroscopicity, and chemical composition of the aerosols on the cloud droplet number concentrations and indirect radiative forcing are also investigated in addition to the CCN activity of particles. Some studies have shown that the influences of chemical properties of aerosol particles and the effects of organics on the cloud formation are particularly significant in polluted environments [*Lance et al.*, 2004; *Leaitch et al.*, 2010]. *Leaitch et al.* [2010] found that large fraction of OC lead to the increase of cloud albedo and that the consideration of the solubility of organics and the aerosol mixing state is necessary for the accurate prediction of N_{cd}. In contrast, other studies have shown that the number concentrations

of aerosol particles determine N_{cd} that the effects of chemical properties and organics are small even in polluted areas [*Fountoukis et al.*, 2007; *Reutter et al.*, 2009]. In the discussion of hygroscopicity and N_{cd}, *Anttila et al.* [*2009*] calculated the activated fractions of particles from HTDMA-derived *g* at ~90% relative humidity (RH) and investigating the size distributions of cloud droplets during cloud events; they reported that slight changes of the fit-based mean *g*, to 0.95 or 1.05 times and to 0.9 or 1.1 times the original values, resulted in changes in the soluble volume fractions (16%–33%) and N_{cd} (10%–50%). *Liu and Wang* [2010] calculated that changing κ of primary organic aerosol (POA) from 0 to 0.1 and κ of SOA from 0.14 to 0.07 or 0.21 (±50%) resulted in a 40%–80% increase and ≤40% change, respectively, of the global average N_{CCN} at 0.1% SS. These results indicated that the hygroscopicity of aerosol particles has a large impact on particle activation. However, few studies have quantitatively investigated the influences and contributions of aerosol properties on cloud properties based on detailed hygroscopicity data, such as the *g* distributions and the CCN activity.

1.8. Objective of this study

In this study, to better understand the critical factors for CCN activation and the number concentrations of CCN and cloud droplets, and the reasons that lead to the differences of the prediction and the measurement of N_{CCN}, atmospheric observations were performed at urban and forest sites. The size-resolved hygroscopicity and CCN activity of urban and forest aerosols were characterized and the relationship between their properties and the chemical composition and the number-size distributions were investigated. Further, hygroscopic parameter κ were derived from the hygroscopic growth factors, CCN activation diameters, and the chemical composition, and the

differences of particle hygroscopicity under sub- and super-saturated conditions and the hygroscopicity of organics were discussed. Then, the influences of the considerations of the hygroscopicity of organics and variations of g with time and particle size on N_{CCN} were investigated. Additionally, to investigate the influences of the difference of particle hygroscopicity on the CCN activation, the respective CCN efficiency spectra of particles with different g were measured individually. Then, the cloud droplet formation was analyzed based on the g distributions using a cloud parcel model.

The background of this study is described in Chapter 1. The principles and configurations of instruments, the methods of calibration and data processing, and some theoretical equations are explained in Chapter 2. The results and discussion from the measurements of urban aerosol particles in Nagoya in 2009 are described in Chapter 3. The characterization of size-resolved hygroscopicity and hygroscopic growth factor distributions are the main topics, and the linkage to the CCN activity, chemical composition, and number-size distribution are discussed, and the information needed for the achievement the accurate prediction of CCN number concentrations are investigated. The results and discussion from the measurements of forest aerosol particles in Wakayama in 2010 are described in Chapter 4. In this Chapter, the influence of the bursts of nanoparticles and their growth on the hygroscopiciy and CCN activity is discussed based on the diurnal variation. Chapter 5 includes the results and discussion from the measurements of CCN activity with less and more hygroscopic particles and the model simulation for cloud droplet formation based on the g distributions. Finally, the summary and conclusions are presented in Chapter 6.

2. Methodology

2.1. Instruments

2.1.1. Differential Mobility Analyzer (DMA)

Differential mobility analyzers (DMA) were used as a part of a scanning mobility particle sizer (SMPS) and a hygroscopicity tandem differential mobility analyzer (HTDMA), both of which are described below. The DMAs are used to classify particles with a specific mobility diameter, based on the relationship between the size and the electrical mobility of the particles in the electrical flow field. Prior to the classification, sample aerosol is passed through an impactor and is neutralized electrically by an ^{241}Am radioactive charger. The aerosol flows from the top to the bottom of the DMA column, in a high voltage field therein. The track of the particles in the DMA column depends on the flow rate and the particle electrical mobility. Particles with a specific electrical mobility are taken from the exit of the DMA.

2.1.2. Condensation Particle Counter (CPC)

A condensation particle counter (CPC) is used to measure the particle number concentrations of a sample aerosol, based on the optical detection of particles grown by the condensation of water/alcohol. Aerosol particles are introduced to a heated saturator, where the condenser evaporates at high temperature (39 degree), and to a cooled saturator, where the vapors condense on the particles. By passing through the heated and cooled saturators, particles can grow up enough to be detected by the light scattering. The number concentrations are obtained by counting the light scattering using a detector.

2.1.3. Scanning Mobility Particle Sizer (SMPS)

A scanning mobility particle sizer (SMPS) is composed of a DMA and a CPC. Aerosol particles with a specific mobility diameter are selected using the DMA and the number concentrations of particles with the selected diameter are measured using the CPC downstream of the DMA. The number-size distribution of the aerosols is obtained by changing the DMA voltage continuously and counting particles using the CPC.

2.1.4. Hygroscopicity Tandem Differential Mobility Analyzer (HTDMA)

A hygroscopicity tandem differential mobility analyzer (HTDMA) is composed of two DMAs and a CPC, and one/multiple humidifier(s) and /or a dehumidifier. Here, a HTDMA system using a humidifier is described. After drying processes (see experimental parts described in section 2.2.1, 2.3.1, and 2.4.1), aerosol particles with a specific dry mobility diameter are selected in the first DMA of the HTDMA. A humidifier with Nafion tubing is placed between the first and the second DMAs. In the Nafion tubing, the aerosol is humidified by the supply of water vapor from the outside of the tubing. Particles therein are grown by the water uptake depending on the hygroscopicity, and possibly to the exposure time. Particles are then introduced to the second DMA coupled to a CPC, and the number-size distributions as a function of particle hygroscopicity and dry mobility diameters are obtained [*Mochida and Kawamura*, 2004].

2.1.5. Cloud Condensation Nuclei Counter (CCNC)

A cloud condensation nuclei counter (CCNC) is used to measure the number of particles that act as CCN under supersaturated conditions in the continuous-flow

thermal-gradient diffusion chamber. In the CCN column, water vapors are provided from the walls. Diffusion of water is faster than that of heat, and the maximum of the supersaturated condition is established at the centerline of the column. The supersaturated condition in the column depends on the difference of temperature between the top and bottom of the column. Aerosol particles passed along the centerline of the CCNC column, and are grown by the uptake of water vapors. Then, particles in 20 size bins from 750 nm to 10 μm are measured based on the light scattering [*Robarts et al.,* 2005; *Lance et al.,* 2006].

2.1.6. High Resolution Time-of-Flight Aerosol Mass Spectrometer (HR-ToF-AMS)

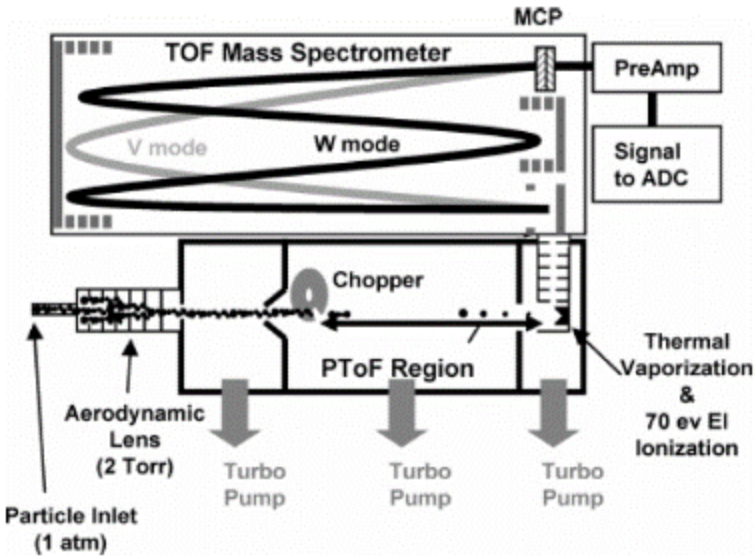

Figure 2.1. The schematic of AMS. Reproduced from *Decarlo et al.,* 2006.

A high resolution time-of-flight aerosol mass spectrometer (HR-ToF-AMS) is used to measure the mass spectra of non-refractory chemical components in submicron aerosol particles. Aerosol particles are introduced to the AMS and are focused to a

narrow particle beam through the critical orifice and the aerodynamic lens. The particles passed the chopper and ToF regions, and chemical components in the particles are vaporized by the impaction to the vaporizer (~600 degree), and are ionized by electron impaction (70eV). The measurement of mass spectra can be performed either of two different modes (V- and W-modes). In the V mode, mass spectra are collected with high sensitivity but with less mass resolution. By contrast, in the W mode, mass spectra are collected with high mass resolution but less sensitivity. Size- and time-averaged mass spectra (MS mode) and size-resolved mass spectra (PTOF mode) can be obtained by different operations of the chopper. [*Decarlo et al.,* 2006].

2.2. Atmospheric observation of aerosol particles at an urban site in Nagoya

2.2.1. Experimental setup

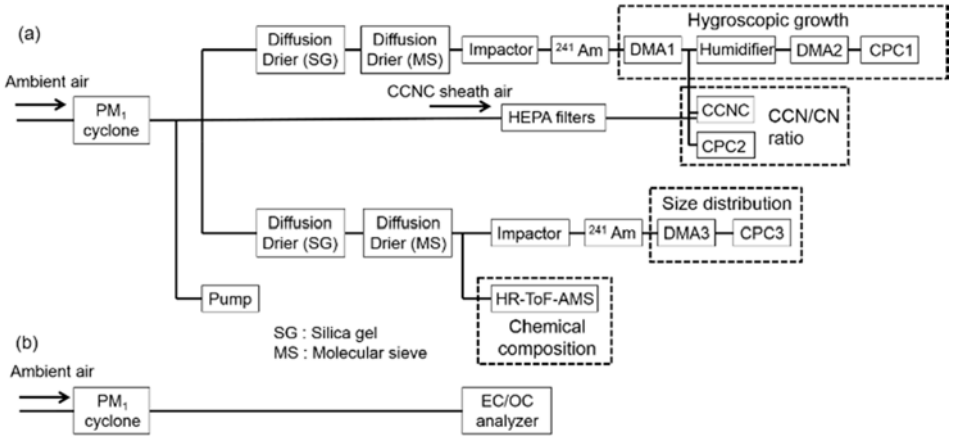

Figure 2.2. Schematic of the instruments.

The observation of atmospheric aerosol particles was conducted at the Higashiyama campus, Nagoya University (35°09′ N, 136°58′ E) in the city of Nagoya, Japan, from September 14 to 24, 2009. Nagoya is the third largest city in Japan

(population: 2.3 million), which located at the center of the Cyukyo metropolitan area (population: 9.1 million). The schematic of the instruments for the observation is presented in Figure 1.

Aerosols were aspirated at two inlets placed at 9.5 m above ground level (AGL) and were passed through a PM_1 cyclone (URG2000-30EHB, URG) at a flow rate of 16.7 L min^{-1}. After the removal of coarse mode particles, the aerosol in one of the sampling lines were introduced to a system composed of a HTDMA and a CCN counter (CCNC, Droplet Measurement Technologies), a high-resolution time-of-flight aerosol mass spectrometer (AMS, Aerodyne Research) and a scanning mobility particle sizer (SMPS, DMA3: model 3080 and 3081, TSI, CPC3: model 3025A, TSI). In the sampling line for the HTDMA-CCNC system, aerosol was dried (RH<1%) in two diffusion driers, one with a silica gel and the other with molecular sieve (13X/4A mixture, Spelco and Sigma-Aldrich). After the aerosol was passed through the impactor and neutralizer, particles with a specific of dry mobility diameter ($d_{p,dry}$, from 24.1 to 359 nm) were selected into the first DMA (DMA1, Model 3081, TSI) of the HTDMA. After humidification of the monodisperse aerosol in Nafion tubing (MD110-24S-4, Perma Pure LLC), the particles were introduced to the second DMA (DMA2, Model 3080 and 3081, TSI) and a condensation particle counter (CPC1, Model 3775, TSI). Then, size-resolved g distribution of particles at 85 ± 1% RH (at the exit of the DMA2 column, with consideration of the accuracy of the sensors) were measured. The mean particle residence time in the sample line downstream of the humidifier and upstream of DMA2, where RH was expected to be stabilized to ~85% was estimated to be 12 s. Particles selected in DMA1 were also introduced to the CCNC and another CPC (CPC2, Model 3025A, TSI), and the size-resolved ratios of CCN to CN were measured under

supersaturation (SS) conditions of 0.12%, 0.24% and 0.43%. The time for one cycle of the measurements of *g* distributions and ratios of CCN to CN was 3 h. The measurements were performed for 34 sizes in $d_{p,dry}$ from 24.1 to 359 nm; the sets of $d_{p,dry}$ depend on the SS conditions. The ratios of the sheath to sample flow rates for the DMAs in the HTDMA and CCNC were 10:1. The sample flow rates of DMA1 in the HTDMA and CCNC were 0.65 and 0.05 L min^{-1}, respectively. The sample flow rates of DMA2 in the HTDMA was 0.3 L min^{-1}. The sample flow exiting DMA1 in HTDMA (upstream of the humidifier and after passing line to CCNC) was verified to be dried (RH<1%) and that the sample and sheath flows entering DMA2 and the sheath flow exiting DMA2 in HTDMA were conditioned to ~85% RH, using temperature and humidity sensors (HMT 337, Vaisala).

In the sampling line for the AMS and SMPS, aerosols were dried (RH<1%) by the passage of two diffusion driers as in the case of the HTDMA-CCNC line. Using the AMS (vaporizer temperature: ~600°C), the size-averaged (MS mode) and resolved (PTOF mode) mass concentrations of non-refractory submicron components (NR-PM_1), i.e., organic matter (OM), sulfate, nitrate, ammonium, and chloride, were measured every 5 min in the V mode. The number-size distributions from 14.1 to 735 nm were measured every 5 min using the SMPS. The sample flow rates of the AMS and SMPS were 0.3 and 0.3 L min^{-1}, respectively. The ratio of the sheath to sample flow rates in the SMPS was 10:1. The sheath flow exiting DMA3 in SMPS was verified to be dried (RH<1%) using a sensor (HMT 337, Vaisala). The excess flow at the inlet of the AMS was also verified to be dried (RH<8%) using another sensor (TR77Ui, T&D).

The PM_1 aerosol in the second sampling line was introduced to an EC/OC analyzer (model 4, Sunset Laboratory) at a sample flow rate of 7.4 L min^{-1}. Mass

concentrations of elemental carbon (EC) and organic carbon (OC) were obtained using a modified version of the protocol from the National Institute for Occupational Safety and Health (NIOSH) every 90 min [*Nakayama et al.,* 2014]. Also, aerosol samples for the off-line analysis were collected on quartz fiber filters (2500QAT–UP, Pall) every two days using a high volume air sampler (Model 120B, KIMOTO) with an impactor whose 50% cut-off diameter is 0.95 μm (TE-230, Tisch Environmental Inc.), to compare the mass concentrations derived from the on-line and off-line analyses. EC and OC in filter samples were quantified using a thermal/optical carbon analyzer (model 2001, Desert Research Institute), and the mass concentrations in the amtosphere were calculated. Ionic species (SO_4^{2-}, NO_3^-, Cl^-, and NH_4^+) in filter samples were quantified using an ion chromatograph (ICS-1000, Dionex).

2.2.2. Calibration and data processing

Standard polystyrene spherical latex (PSL) particles (STADEX, JSR, mean diameter ± the expanded uncertainty (CV): 48 ± 1 nm (15.57%), 100 ± 3 nm (2.47%), 309 ± 9 nm (1.13%)) were introduced to the three DMAs in the HTDMA and the SMPS to examine instrument performance prior to making field measurements. The mode diameters of the log-normal functions fitted to the measured number-size concentrations for 100 nm and 309 nm PSL particles, with the consideration of the width of the DMA transfer function, were on average within the range of mean diameter ± the expanded uncertainty described above, while those of the 48 nm PSL particles were 1 nm off from the range described above.

Size-resolved g distributions were derived as function of particle number concentrations in the bins of g and $d_{p,dry}$, $n(\log d_{p,dry}, \log g)$. The raw data observed in

HTDMA show broaded distributions caused by the width of the transfer functions in DMAs and the calculation of g without the corrections may be led to biases [*Gysel et al.,* 2009]. At first for the calculations in this study, the kernel functions that express the posibility of particle penatration in DMA1 were obtained in the bins of 1/64 decade from 24 to 359 nm. Then, the inversion calculation to correct for the widths of the transfer functions of the DMAs using the Twomey algorithm was performed for each g distributions [*Mochida et al.,* 2010]. Here, the double integral of $n(\log d_{p,dry}, \log g)$ in the $\log d_{p,dry}$-$\log g$ plane corresponds to the number concentrations of aerosol particles within the range of $d_{p,dry.}$ The hygroscopic growth factor g is defined by the following equation:

$$g = \frac{d_{p,\,wet}}{d_{p,\,dry}} \tag{1}$$

Here, $d_{p,dry}$ and $d_{p,wet}$ are the electrical mobility diameter of particles under dry and wet conditions, respectively. In the calculation of g, sizing based on DMA2 was slightly corrected (<2%) so that log-normal fittings for g distributions of dry ammonium sulfate particles (99.999% purity, Sigma-Aldrich) has maxima at g of unity. The g distributions of ammonium sulfate particles at 85% RH were measured using the HTDMA to check the performance before and after ambient aerosol measurements. If the mode values of the log-normal fitting are used as representative g of ammonium sulfate at 85% RH, the values of 24–359 nm particles (16 sizes) agreed with g calculated based on the literature of *Tang and Munkelwitz* [1994] within 6%. For atmospheric aerosol particles, the mean of g for g distributions measured every 3h for respective $d_{p,dry,}$ g_m ($d_{p,dry}$), and the average g that corresponds to the mean volume of the retained water by particles, g_{m_water} ($d_{p,dry}$), were calculated by the following equations:

$$g_{\mathrm{m}}(d_{\mathrm{p,dry}}) = \frac{\sum n(\log d_{\mathrm{p,\,dry}}, \log g) \bullet g}{\sum n(\log d_{\mathrm{p,\,dry}}, \log g)} \qquad (0.8 \leq g \leq 2.2) \qquad (2)$$

$$g_{\mathrm{m\_water}}(d_{\mathrm{p,dry}}) = \left[\left(\frac{\sum n(\log d_{\mathrm{p,\,dry}}, \log g) \bullet (g^3 - 1)}{\sum n(\log d_{\mathrm{p,\,dry}}, \log g)} \right) + 1 \right]^{\frac{1}{3}} \qquad (0.8 \leq g \leq 2.2) \qquad (3)$$

For g distributions measured every 3h for respective $d_{\mathrm{p,dry}}$, mean values for the ranges of $0.8 \leq g \leq 1.1$ and $1.1 \leq g \leq 2.2$ ($g_{\mathrm{l}}(d_{\mathrm{p,dry}})$ and $g_{\mathrm{h}}(d_{\mathrm{p,dry}})$, respectively) were also calculated.

The CCN efficiency spectra (the size-resolved ratios of CCN to CN) of singly-charged particles were derived with the corrections for diffusion losses in the sampling line, the presence of multiply-charged particles, and the width of transfer functions [*Mochida et al.,* 2010, 2011; *Kawana et al.,* 2014]. The CCN activation parameters, $F_{\max}$, d_{act}, and σ were derived by a fitting using the equation in *Rose et al.* [2008]:

$$f_{n\mathrm{CCN}\,/\,n\mathrm{CN}} = \frac{F_{\max}}{2}\left[1 + \mathrm{erf}\left(\frac{d_{\mathrm{p,\,dry}} - d_{\mathrm{act}}}{\sigma\sqrt{2}}\right)\right] \qquad (4)$$

Here, $F_{\max}$ is the value that $f_{n\mathrm{CCN}/n\mathrm{CN}}$ approaches as $d_{\mathrm{p,dry}}$ increases and σ is the standard deviation (SD). The fittings using equation 4 were performed with considerations of the broadening due to the widths of transfer functions of DMA1 using Matlab programs (Mathworks, ver. R2008a). Briefly, the calculation was based on an optimization to obtain equation 4 with which the CCN/CN ratios calculated in the following manner are close to the measured: (1) the curve that is the product of the distribution of the DMA transfer function for the diameter subjected to the CCN/CN measurement, the hypothetical number-size distribution of singly-charged particles introduced to the CCNC and CPC2 if the DMA was absent, and equation 4 was integrated along the axis of particle diameter in logarithmic scale; (2) the curve that is

the product of the distribution of the transfer function, the hypothetical number-size distribution of singly-charged particles if the DMA was absent was integrated as (1); (3) the integrated value from (2) divided by the integrated value from (1) was calculated for respective diameter for measurements, and was regarded as the estimated ratio of CCN to CN at the diameter. The SSs in the CCNC were determined to be 0.12%, 0.24%, and 0.43% from d_{act} of ammonium sulfate particles based on the Köhler equation incorporating the Pitzer equation [*Mochida et al.,* 2010]. In the CCNC, the particles larger than 1 μm (0.12% SS) and particles larger than 0.75 μm (0.24% and 0.43% SS) were counted as CCN at 0.12% SS, and 0.24% and 0.43% SS, respectively. For the analysis of atmospheric aerosols, 3-min data were used for the calculation of the ratios of CCN to CN at respective sizes. The data collected under unstable flow conditions were omitted.

Size calibration of the PToF mode of the AMS was performed using 59 ± 2.5, 97 ± 3, 200 ± 6, 300 ± 6, 498 ± 5, and 799 ± 9 nm PSL particles (Duke Scientific, Thermo Fisher). The single ion value (SI) was determined based on the peak area of $^{184}W^{+}$. Ionization efficiency (IE) and the relative ionization efficiency (RIE) of ammonium were determined using ammonium nitrate particles (>99% purity, Sigma-Aldrich). The mass concentrations and the mass size distributions of NR-PM_1 components were calculated using a ToF-AMS Data Analysis Toolkit, SQURREL (ver, 1.55D) with Igor Pro 6.34 (Wavemetrics Inc.). For the processing of mass spectrum signals, some factors in the fragment table, those origined from air and carbon dioxide in the gas phase, i.e., $^{16}O^{+}$, $^{14}N^{14}N$, $^{15}N^{14}N$, and $^{44}CO_2$, were corrected based on the spectra during the particle-free air measurement using a HEPA filter (TSI). The mass ratios of OM/OC and the molar ratios of O/C, H/C, N/C, and S/C were calculated from data collected in the V

mode (m/z <116) with a high-resolution analysis using a ToF-AMS Data Analysis Toolkit, PIKA (ver, 1.14D). RIE values of 1.4, 1.2, 1.1, and 1.3 were applied for organics, sulfate, nitrate, and chloride [*Sun et al.,* 2009], respectively. RIE of 5.5 was applied for ammonium based on the experiment using ammonium nitrate. Collection efficiency (CE) of 0.5 was used for quantification (see section S1 in Supporting Auxiliary Material).

Calibration for the quantification of the EC/OC analyzer was performed using a filter on which a sucrose solution was dropped. Uncertainty associate with the calibration was estimated to be 12%. Further, blank measurements were performed before and after the atmospheric observation. The detection limits (± 3 SD) for EC and OC were estimated as 0.01 and 0.20 μg m^{-3}, respectively, based on the blank measurements.

2.2.3. Calculation of hygroscopicity parameter

The saturation ratio of water vapor (S) and droplet diameter is explained by the following equation:

$$S = a_{\mathrm{w}} \exp\left(\frac{4\sigma_{\mathrm{s}} M_{\mathrm{w}}}{RT\rho_{\mathrm{w}} d_{\mathrm{p,\,wet}}} \right) \tag{5}$$

Here, a_w is the activity of water in solution, σ_s is the surface tension, M_w is the molecular weight of water, R is the universal gas constant, T is the absolute temperature, and ρ_w is the density of water. The hygroscopicity parameter κ is defined by the following equation [*Petter and Kredenweis,* 2007]:

$$\frac{1}{a_{\mathrm{w}}} = 1 + \kappa \cdot \frac{V_{\mathrm{s}}}{V_{\mathrm{w}}} \tag{6}$$

Here, V_s and V_w are the volumes of dry particle matter in the solute and water, respectively. The S is expressed using κ as:

$$S = \frac{d_{p,wet}^3 - d_{p,dry}^3}{d_{p,wet}^3 - d_{p,dry}^3(1-\kappa)} \exp\left(\frac{4\sigma_s M_w}{RT\rho_w d_{p,wet}}\right) \quad (7)$$

In this study, the κ of particles under sub- and super-saturated conditions were calculated from the HTDMA and CCNC data, respectively. The κ of particles from the HTDMA (κ_{HTDMA}) were calculated based on size-resolved g at 85% RH, with equations 6 and 7 and the following equation:

$$g^3 - 1 = \frac{V_w}{V_s} \quad (8)$$

$$\kappa_{HTDMA} = \left(g^3 - 1\right)\left[\frac{\exp\left(\frac{4\sigma_s M_w}{RT\rho_w d_{p,wet}}\right)}{0.85} - 1\right] \quad (9)$$

On the other hand, the κ of particles from the CCNC (κ_{CCNC}) were calculated using equation 5 with CCN activation diameters d_{act} as inputs of $d_{p,dry}$. For the calculation of κ_{HTDMA}, T was assumed to be 301 K, the mean temperature of the sheath flow exiting DMA2 during the observation. For the calculation of κ_{CCNC}, T was assumed to be 302 K, the mean temperature of the top of the column of the CCNC during the observation. For both calculations, σ_s were assumed to be the same as that of pure water; they were calculated with consideration of the dependence on temperature [*Hänel,* 1976].

2.2.4. CCN closure

The ratios of N_{CCN} to N_{CN} were predicted based on the hygroscopic growth factors and the number-size distributions, and were compared to the measured N_{CCN}/N_{CN}. This

comparison was made to investigate the influences of the hygroscopicity of organics and particles to N_{CCN}. In the CCN closure, the distributions of g in 76 size bins of $d_{p,dry}$ from 24 to 359 nm were considered, so that the bins are identical to those for SMPS data (64 bins per decade). For the size bins in which the distributions of g were obtained by the HTDMA, the distributions were used for the bins. For the other bins, the distributions were assumed so that the probability density functions of g are same as those in the nearest bins at which g distributions were measured and that the integration of the distributions along the axis of log$g$ equals to dN/dlog$d_{p,dry}$ from the SMPS. For the size bins in which the ratios of CCN to CN were obtained by the CCNC, the ratios were used for the bins. For the other bins, the ratios at the midpoint diameter of the bins in the logarithmic scale were estimated by linear interpolation, and were used for the bins. Then, the CCN number concentrations were calculated from the ratios and dN/dlog$d_{p,dry}$ from the SMPS.

The influence of the hygroscopicity of organics on N_{CCN} was examined with (1) assumed κ_{org} based on literature (0, 0.1, and 0.2), and (2) size-averaged and (3) size-resolved κ_{org} from HTDMA data. In the analysis, the κ of particles was calculated using the κ_{org} from the ZSR approach (see section 3.4). Then, the CCN activation diameters of particles at 0.12%, 0.24%, and 0.43% SS were estimated and particles larger than the diameters were considered as CCN. Further, the contribution of the variations of g with size and time, and g distributions on N_{CCN} was examined with (1) a constant mean bulk g throughout the observation period, (2) time-resolved bulk g, (3) time-averaged and size-resolved g, (4) time- and size-resolved g and (5) time- and size-resolved g distributions. For these analyses, g in 76 dry diameter bins were used for the size-resolved calculations, and g every 3h were used for the time-resolved calculations. The

time-resolved bulk g in case 2 corresponds to the average of g in terms of the volume of the retained water relative to that of solute in the range from 24.1 to 359 nm:

$$g_{\mathrm{m\_water\_aver}} = \left[\left(\frac{\sum_{\log d\mathrm{p,dry}} \sum_{\log g} n(\log d_{\mathrm{p,\,dry}}, \log g) \bullet (g^3 - 1)}{\sum_{\log d\mathrm{p,dry}} \sum_{\log g} n(\log d_{\mathrm{p,\,dry}}, \log g)} \right) + 1 \right]^{\frac{1}{3}} \tag{10}$$

The constant mean bulk g of 1.27 in case 1 is the time average of the time-resolved bulk g in case 2. The maximum of S (S_{crit}) for particles were computed using equation 5. Then, particles having S_{crit} lower than SS in the CCNC were considered as CCN.

2.3. Atmospheric observation of aerosol particles at a forest site in Wakayama

2.3.1. Experimental setup

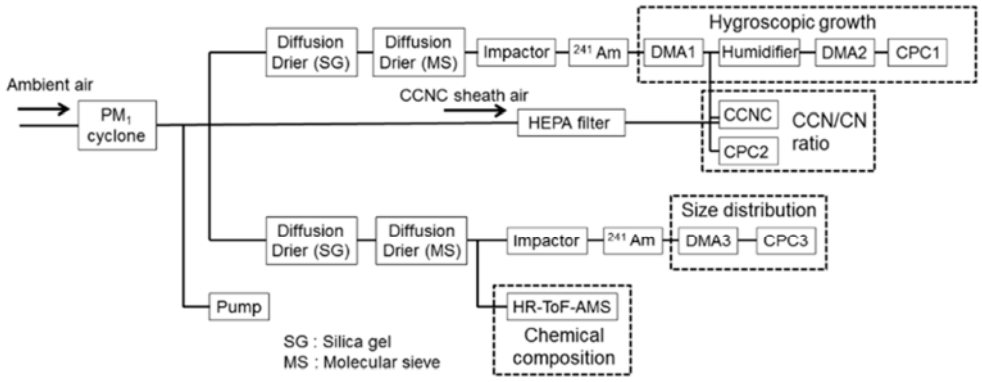

Figure 2.3. Schematic of the instruments.

The observation of atmospheric aerosols was performed at Wakayama Research Forest station of Field Science of Kyoto University at a forest site of Wakayama, Japan, from 20 to 30 August, 2010. The instrument scheme (Figure 2.3) was similar to the

measurements of urban aerosols in Nagoya, in 2009 as described in section 2.2.1. The measurement of chemical composition and number-size distributions were described in *Han et al.,* [2013, 2014]. Here, the measurement of the sampling line composed of an HTDMA and a CCNC are described briefly. Aerosol particles were passed through PM_1 cyclone (flow rate: 16.7 L min^{-1}) from the inlet at 7.5 m AGL. After a drying process, the particles (RH<2%) in the aerosols were classified with a specific $d_{p,dry}$ from 24 to 359 nm in DMA1. The classified aerosol was humidified by passing a Nafion tubing at ~85% RH, and were introduced to DMA2 coupled to CPC1 to obtain resulting size-resolved *g* distributions at 85% RH. Particles selected in DMA1 were also introduced to the CCNC and CPC2 to obtain size-resolved CCN/CN ratios. One cycle of HTDMA-CCNC measurement for 34 sizes from 24 to 359 nm, was 3 h.

2.3.2. Calibration and Data processing

The details of the methods of calibration and data processing are described in section 2.2.2. The classification performance of DMA1 and DMA2 was examined using standard PSL particles with the diameters of 48 ± 1, 100 ± 3, and 309 ± 9 nm (STADEX, JSR). The *g* distributions as a function of particle number concentrations in the bins of *g* (0.8<g<2.2) and $d_{p,dry}$ (24.1–359 nm) were obtained after the corrections for the difference of the sizing of DMA1 and DMA2 and the width of the transfer function, as described in section 2.2.2. The *g* was defined as the ratio of the electrical mobility diameter under a humidified condition ($d_{p,wet}$, ~85% RH) to that under a dry condition ($d_{p,dry}$, RH<2%). The *g* values were obtained by the fitting of a log-normal function to *g* distributions. The *g* distribution for ammonium sulfate particles (99.999% purity, Sigma-Aldrich) were examined under dry and humidified conditions using the

HTDMA before and after the observation. The g values measured for ammonium sulfate particles agreed to the literature values in *Tang and Munkelwitz* [1994], within 10%

The CCN efficiency spectra as a function of the ratios of N_{CCN} to N_{CN} and $d_{p,dry}$ (24.1–359 nm) were obtained with the corrections of the diffusion losses, the presence of multiply-charged particles, and the width of transfer functions [*Rose et al.,* 2008; *Mochida et al.,* 2010, 2011; *Kawana et al.,* 2014]. The CCN activation curves for singly-charged particles under three SS conditions were obtained by the fitting function described in *Rose et al.* [2008]. The SS in the CCNC were determined to be 0.12%, 0.23%, and 0.41%, from d_{act} of ammonium sulfate particles.

2.3.3 Calculation of hygroscopicity parameter

As seen in section 2.2.3, the κ values of forest aerosol particles under the sub-saturated condition (85% RH), κ_{HTDMA}, was calculated based on the size-resolved g and κ-Köhler theory. Further, κ values under the super-saturated conditions, κ_{CCNC}, were also obtained so that the maximum of S corresponds to the SS conditions (0.12%, 0.23%, and 0.41%) with $d_{p,dry}$ of the CCN activation diameters. In the calculations of κ_{HTDMA} and κ_{CCNC}, T were assumed to be 298K (the mean temperature of the sheath air exiting DMA2 in HTDMA) and 300K (the mean temperature of the top of the CCNC column), respectively. The σ_s value was assumed to be that of pure water in both calculations; they were calculated taking temperature dependence into consideration [*Hänel,* 1976].

2.3.4. CCN closure

In CCN closure for forest aerosol particles, N_{CCN}/N_{CN} was predicted using (1) a representative parameter g during observation, (2) size-averaged g in four time sections

non-event/NPF-event days, daytime/nighttime), (3) time-averaged g in four time sections, (4) size-averaged g for every 3 h, (5) size- and time-resolved g, and (6) size- and time-resolved g distributions. In the analysis, the maximum supersaturation S_{crit}, corresponding to the maximum of S from the Köhler equation was calculated iteratively with κ_{HTDMA} at each diameter. Then, particles having S_{crit} lower than the SS in the CCNC (0.12%, 0.23%, and 0.41%) were regarded as CCN.

2.4. CCN activity of aerosol particles with different hygroscopicity in Nagoya

2.4.1. Experimental setup

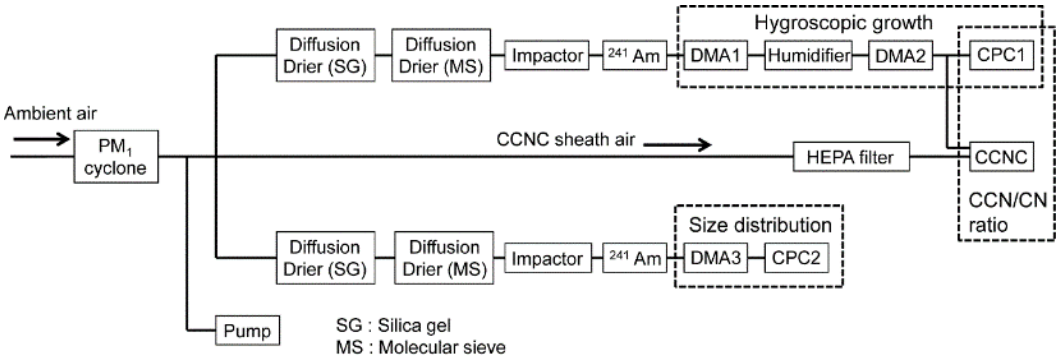

Figure 2.4. Schematic of the instruments.

Atmospheric observation of aerosol particles was made at Higashiyama campus, Nagoya University in Nagoya, from July 29 to August 3, 2010. The schematic of the instruments is shown in Figure 2.4. Aerosol particles were introduced into a PM_1 cyclone (URG) from the inlet at 9.5m AGL at a flow rate of 16.7 L min^{-1}. After aerosols were dried (RH<2%), particles were passed through the impactor and the neutralizer, and those having $d_{p,dry}$ from 24.1 to 359 nm were separated in the first DMA (DMA1,

Model 3081, TSI Inc.) of the HTDMA. After humidification in Nafion tubing (MD110-24S-4, Perma Pure LLC), the particles were further separated in the second DMA (DMA2, Model 3080 and 3081, TSI Inc.) at 85 ± 1% RH to select particles with specific g (g_{set}) around 1.0, 1.1, 1.25, and 1.4. The particles with the selected $d_{p,dry}$ and g_{set} were introduced to the CCN counter (CCNC, Droplet Measurement Technologies) and the condensation particle counter (CPC1, Model 3775, TSI Inc.). The number concentrations of CCN ($n_{DMA2,CCN}$) and CN ($n_{DMA2,CN}$) for particles with g_{set} of 1.0, 1.1, 1.25, and 1.4 were measured by the CCNC and CPC1, respectively, under supersaturation (SS) conditions of 0.18%, 0.49% and 0.95%. Measurements were performed four times for particles with g_{set} of 1.0, 1.1, 1.25, and 1.4 at 0.18%, 0.49% and 0.95% SS. The g distributions were obtained for 16 sizes, from 24.1 to 359 nm, for particles in the range of $0.8 \leq g \leq 2.2$ as averages of the results from two measurements during 0600−0900 JST and those during1800−2100 JST. Measurements were performed for 11 time periods during the observation. Temperature and humidity in the HTDMA were monitored using sensors (HMT 337, Vaisala). The sample flow exiting DMA1 (upstream of the humidifier) was verified to be dried (RH<2%), and the sample and sheath flows entering DMA2 and the sheath flow exiting DMA2 were also verified to be humidified (~85% RH). The sample flow rates of the DMAs in the HTDMA were 0.35 L min^{-1}. The ratios of the sheath to sample flow rates for the DMAs were 10:1.

A portion of the sample aerosols that passed through the PM_1 cyclone was subjected to number-size distribution measurements using a scanning mobility particle sizer (SMPS). The SMPS is composed of a DMA (DMA3, Model 3080 and 3081, TSI) with a temperature and humidity sensor at the exit of the sheath line (HMT 337, Vaisala) and a CPC (CPC2, Model 3025A, TSI). The size distributions from 14.1 to 711 nm were

measured every five minutes. The sheath flow exiting DMA3 was confirmed to be dried (RH<5%) during the observation. The sample flow rate of the SMPS was 0.3 L min^{-1}. The ratio of the sheath to sample flow rate was 10:1.

2.4.2. Calibration and data processing

The details of the methods of calibration and data processing are described in section 2.2.2. The classification performance of DMA1 and DMA2 was examined using the standard PSL particles with the diameters of 48 ± 1, 100 ± 3, and 309 ± 9 nm (STADEX, JSR). Ammonium sulfate particles were introduced to the HTDMA before and after atmospheric observation, to examine the *g* distributions at 16 sizes, from 20.2 to 359 nm, under dry and humidified conditions. Inversion calculation [*Mochida et al.*, 2010] and log-normal fittings were used to calculate the ratios of fitted mode diameters under humidified versus dry conditions (i.e., *g* at ~85% RH). In most cases, the obtained *g* agreed with the values from *Tang and Munkelwitz* [1994] within 5%. The setting diameters of DMA2 were corrected based on the differences of sizing between DMA1 and DMA2. This was determined by introducing ammonium sulfate particles to the HTDMA under the dry condition of DMA2 and calculating the size dependence using a third degree polynomial before the observation. Ammonium sulfate particles were introduced again after the observation and *g* for 16 sizes were found to agree within 1% of those before the observation.

The actual *g* of the particles selected according to g_{set} had some variation because of the width of the DMA transfer function. This was accounted for as follows. First, the *g* distributions in 11 time periods (Figure 5.2) for 16 sizes were retrieved using the Twomey algorithm, according to the work by *Mochida et al.* [2010]. Figure 2.4.2

show the probability density functions of g (gf-PDF) for particles with $d_{p,dry}$ of 28.9, 49.6, 102, and 209 nm and the HTDMA kernel functions, which represent the transfer function of the HTDMA for singly-charged particles, with g_{set} of 1.0, 1.1, 1.25, and 1.4. Different from the work by *Mochida et al.* [2010], the kernel functions and distributions of g in the bins of 1/1024 per decade were used without the conversion to coarse bins. Next, the gf-PDF for particles classified according to g_{set} (gf-PDF$_{gset}$) was obtained by multiplying gf-PDF by the kernel functions of g_{set} and by normalizing the resulting distributions, as shown in Figure 2.5. The mean of g of particles selected in DMA2 (g_m) varied with the time and dry particle diameter; the mean ± standard deviation (or ranges) of g_m at g_{set} of 1.0, 1.1, 1.25, and 1.4 for 16 sizes were calculated to be 1.023 ± 0.006 (1.011–1.034), 1.081 ± 0.009 (1.065–1.094), 1.265 ± 0.011 (1.250–1.291), and 1.393 ± 0.032 (1.330–1.449), respectively. The differences of g_m from g_{set} depended on the particle size (from 24.1 to 359 nm), and were up to 2%. The differences of g_m averaged for different sizes (from 24.1 to 359 nm) from g_{set} were up to 9%.

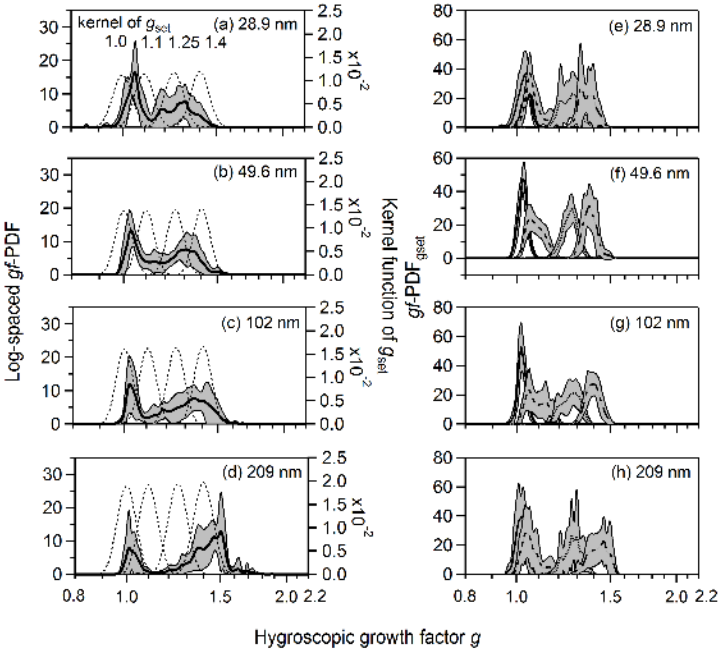

Figure 2.5. (a–d) Log-spaced probability density functions of hygroscopic growth factors (*gf*-PDF) (mean: solid line, range of standard deviation: shaded area) and the HTDMA kernel functions for g_{set} of 1.0, 1.1, 1.25, and 1.4 and dry mobility diameter ($d_{p,dry}$) of (a) 28.9 nm, (b) 49.6 nm, (c) 102 nm, and (d) 209 nm. (e–h) The estimated *gf*-PDF_{gset} of particles downstream of the DMA2 with $d_{p,dry}$ of (e) 28.9 nm, (f) 49.6 nm, (g) 102 nm, and (h) 209 nm. The lines represent *gf*-PDF_{gset} for particles with g_{set} of 1.0 (solid), 1.1 (dotted), 1.25 (dashed), and 1.4 (dashed-dotted). The shaded areas represent the range of the standard deviation. The shaded areas with negative values of *gf*-PDF and *gf*-PDF_{gset} are not shown.

Ammonium sulfate particles (99.999% purity, Sigma-Aldrich) were also introduced to the CCNC to calibrate the SS conditions before and after atmospheric observation. The CCN efficiency spectra of singly charged particles were obtained with consideration of the presence of multiply charged particles. The influences of the presence of multiply charged particles on the data of hygroscopic growth and CCN activation and the method to correct CCN efficiency spectra are described in Appendix A1 at the end of this chapter. The CCN activation diameters d_{act} were calculated from CCNC data using the function proposed by *Rose et al.* [*2008*]. The SS in the CCNC were calculated to be 0.18%, 0.49%, and 0.95% from $d_{act,CCN}$ of ammonium sulfate particles. For the atmospheric data, the CCN efficiency spectra of singly-charged particles were obtained for particles at four g_{set} values (1.0, 1.1, 1.25, and 1.4) under three SS conditions (0.18%, 0.49%, and 0.95%). The corrections were the same as those used for calibration with the ammonium sulfate particles. In the data analysis, $n_{CN,\,DMA2}$ that correspond to <50 counts in 210 seconds were not used because of large uncertainties.

In this study, the CCN efficiency spectra for particles with g_{set} were predicted from the measured distributions of g to assess the prediction of CCN activation of aerosol particles from the hygroscopicity data. The values of the CCN efficiency spectra (i.e., $n_{CCN,DMA2}/n_{CN,DMA2}$ of particles at each dry diameter and at specific g_{set}) were calculated by integrating gf-PDF_{gset} over bins having S_{crit} smaller than the SS conditions in CCNC (0.18%, 0.49%, and 0.95%). κ-Köhler theory using a single hygroscopic parameter κ (proposed by *Petters and Kreidenweis* [2007]), as expressed by equation 3 described in section 2.2.3, is used for the prediction.

S_{crit} of CCN was calculated as follows. First, κ was calculated with S of 0.85 and $d_{p,dry}$ and $d_{p,wet}$, the mobility diameters of particles in DMA1 and DMA2 of HTDMA, respectively. Next, the maximum of S (i.e., S_{crit}) was computed iteratively using the calculated κ. For this calculation of κ from g at 85% RH, T was assumed to be 301 K, the mean temperature of the sheath flow exiting DMA2 during the observation. For the calculation of S_{crit}, T was assumed to be 302 K, the mean temperature of the top of the CCNC column during the observation. For both of the calculations, σ_s were assumed to be that of pure water. The CCN activation diameters ($d_{act,g85}$) were then predicted using equation 3. Strictly, the distributions of dry mobility diameters of particles selected in DMA2 could skew as compared with those selected in DMA1 depending on the g distributions of particles selected in DMA1 and g_{set}. This effect was not taken into account in the analysis. The relative standard deviation of Gaussian curves fitted to the transfer functions of DMA1 at 16 $d_{p,dry}$ settings, that is, the indicator of the size distributions of dry particles selected in DMA1, is small (3%) as compared with the variations of CCN activation diameters calculated by different methods. Therefore, the above effect was presumably not important for the main discussion.

2.4.3. Cloud parcel model

The cloud parcel model has been explained elsewhere [*Takeda and Kuba*, 1982; *Kuba and Takeda*, 1983; *Kuba et al.*, 2003]. Here, the calculation scheme has been modified from the previous versions by calculating the growth and activation of particles by κ-Köhler theory.

In the cloud parcel model, N_{cd} and R_{eff} were calculated at updraft velocities (v) of 0.1, 0.5, 1.0, and 5.0 m s^{-1} as an air parcel rises 100 m adiabatically from the cloud base at 500 m AGL. The input data to the model were the cumulative number-size distributions of aerosol particles, based on the HTDMA and SMPS data. In the base case of the model, all the aerosol particles in the range of $0.8 \leq g \leq 2.2$ were considered. In the model calculations of the base case, corrections for the difference of the CCN activation diameters using the HTDMA and CCNC and the presence of CCN-inactive particles were made based on the results from the HTDMA and CCNC. In some cases, only a portion of particles in specific ranges of g were assumed to be present. The hygroscopic parameter κ of all particles with $d_{p,dry}$ from 20.2 to 359 nm was converted to that of pure ammonium sulfate (κ: 0.61) [*Petters and Kreidenweis*, 2007], with the conversion of the diameter so as to have the same S_{crit} based on the κ-Köhler theory. The conversion was performed for particles with g and $d_{p,dry}$ in the resolutions of 64 and 16 bins per decade, respectively. For each bin, the midpoint values of g and $d_{p,dry}$ on the log-scale were used. The cumulative number-size distributions for these particles were then calculated based on the conversion. For particles larger than 359 nm (up to 18.8 μm), the cumulative number-size distributions were estimated by extrapolation using log-normal fittings to the number-size distributions measured using the SMPS (from

14.1 to 711 nm). All particles larger than 359 nm were treated as ammonium sulfate without the conversion of the diameters. Based on the above calculations, the contribution of particles with different hygroscopicity to the cloud droplet formation was evaluated.

In the case where the difference of the CCN activation diameters was considered in the model, κ at 85% RH (κ_{85}) and κ_{CCN} with different g were calculated from HTDMA-derived and CCNC-derived activation diameters. With the series of corrections as described in section 2.4.2 and above, the difference of the CCN activation diameters predicted from the HTDMA data and those measured using the CCNC was discussed.

3. Characterization of urban aerosol particles in Nagoya

3.1. Meteorological conditions, gaseous pollutants, and air mass origin

During the study period, little precipitation was observed (Figure 3.1a). The mean ± standard deviation (SD) of mixing ratios of gaseous pollutants, NO, NO_2, NO_x, SO_2, and oxidant (O_x) were 2 ± 3, 13 ± 8, 15 ± 9, 2 ± 1 ppb, and 35 ± 19 ppm, respectively (Figures 3.1c and 3.1d). The concentration of O_x shows diurnal variation pattern with a miximum in the afternoon, indicating that O_x was influenced by local photochemical activity (Figure 3.1d). The time series of wind direction and wind speed show that the northerly wind was predominant during the first six days and that no specific wind direction were observed during the last four days (Figure 3.1b). Five-day backward trajectories suggest that the air masses during the first six days were from the Japan sea and the Asian continent (Figure 3.2). They also suggest that air masses during the last four days passed over the coastal region of Japan that faces on the Pacific Ocean.

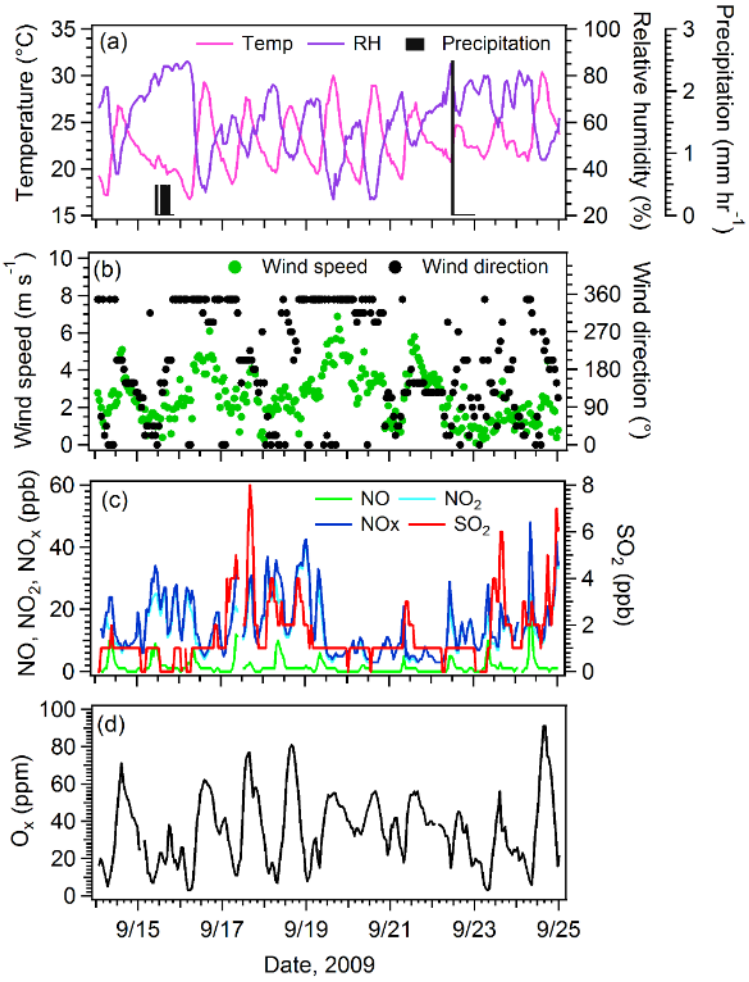

Figure 3.1. Time series of (a) air temperature, relative humidity, and precipitation rate, (b) wind speed and wind direction, (c) NO, NO_2, NO_x, and SO_2 and (d) O_x. The meteorological conditions and the mixing ratios of gaseous species were measured at Nagoya Meteorological Observatory (~1.5 km from the observation site at Nagoya University) and National Atmospheric Monitoring Station (~2.6 km from the observation site at Nagoya University), respectively. The meteorological data were obtained from Japan Meteorological Agency. The data of gaseous species were obtained from the database of National Instistute for Environmental Studies.

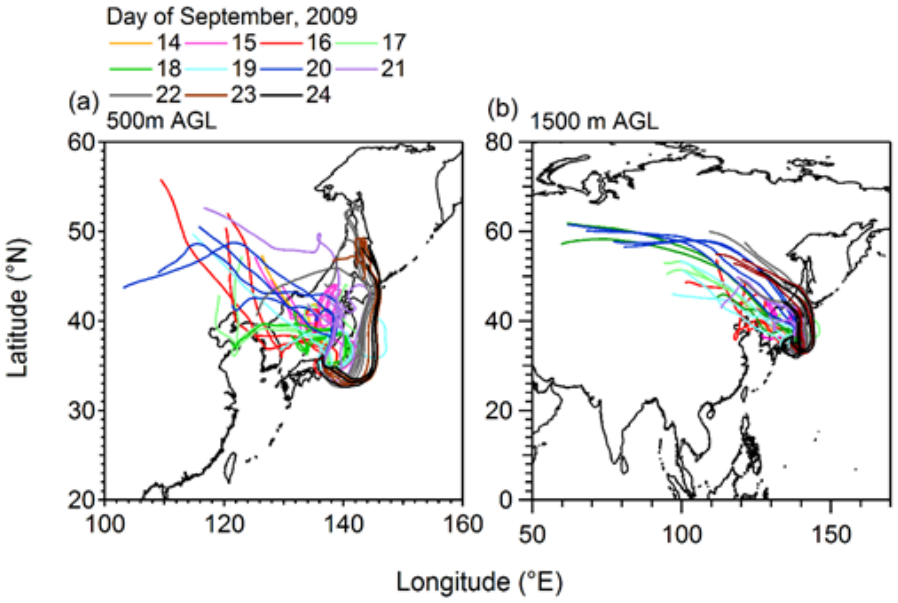

Figure 3.2. Five-day backward air mass trajectories from the observation site, with the start heights of (a) 500 and (b) 1500 m above ground level at 0000, 0800 and 1600 LT (JST) during the observation period. The trajectory analysis was performed using the HYbrid Single-Particle Lagrangian Integrated Trajectory (HYSPLIT) model from National Oceanic and Atmospheric Administration (NOAA) Air Resources Laboratory [*Draxler and Rolph*, 2003]. The meteorological data is from Global Data Assimilation System (GDAS) of National Centers for Environmental Prediction (NCEP).

3.2. Number-size distributions

The time series of the number-size distribution of aerosol particles is presented in Figure 3.3a. The distributions were characterized by the dominance (mean: 76%) of the Aitken mode particles ($d_{p,dry}$<100 nm). The mode diameters derived from fittings with a single log-normal curve are also shown in Figure 3.3a. The mean ± SD of the mode diameters was 59 ± 10 nm. The time series of the total number concentrations of aerosol particles (N_{CN}) is depicted in Figure 3.3b. The mean ± SD of N_{CN} were 4101 ± 1983 cm^{-3}. The increase of N_{CN} accompanying a small mode diameter (~30 nm) around noon, and subsequent increases in the mode diameter in the afternoon were observed on 20

and 21 September. This phenomenon can be explained by the occurrence of formation of new particles [*Salma et al.,* 2011] and/or the emission of primary fine particles, such as HOA and BC [*Zhang et al.,* 2005a, 2005b], followed by their growth due to coagulation and condensation.

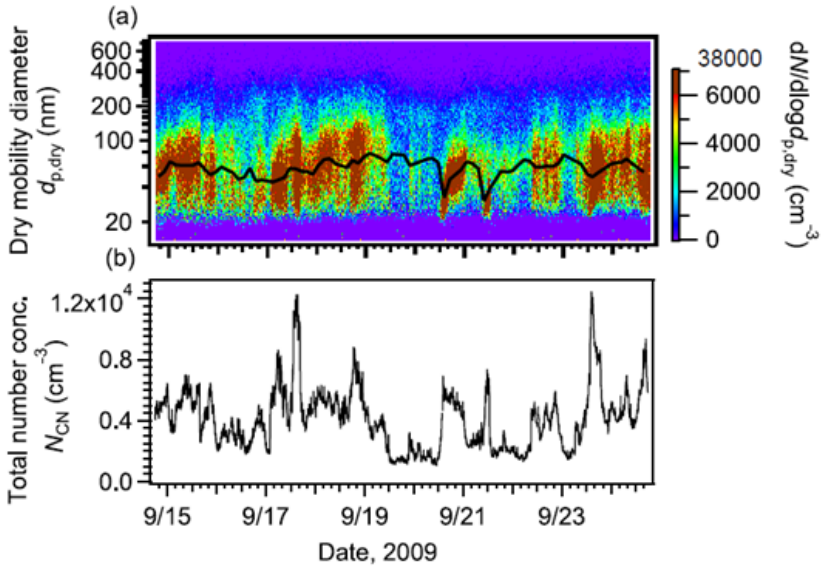

Figure 3.3. Time series of (a) the number-size distributions and (b) the total number concentrations of aerosol particles (N_{CN}) at 14.1–735 nm. The black line in 2a represents the mode diameters of fitted single log-normal functions.

3.3. Chemical composition

The time series of the mass concentrations of NR-PM_1 and carbonaceous components are presented in Figures 3.4a and 3.4b, respectively. The mean ± SD of the mass concentrations of the sum of NR-PM_1 components (OM, sulfate, ammonium, nitrate, and chloride) and EC was 8.1 ± 3.5 μg m^{-3}. The time series of the mass fraction is shown in Figure 3.4c. The mean ± SD of the mass fractions of OM, sulfate, ammonium, nitrate, chloride, and EC were 53% ± 9%, 23% ± 8%, 10% ± 2%, 7% ± 5%, 0.1% ± 0.1%, and 8% ± 4%, respectively. Organics was dominant, as observed at other

urban sites [*Zhang et al.,* 2007; *Jimenez et al.,* 2009]. The mass fractions from the average mass-size distributions of NR-PM_1 components are presented in Figure 3.4d. The time series of f_{43}, f_{44}, and f_{57} (the ratios of the signal intensities of m/z 43, 44, and 57, respectively, to those of the total OA) are presented in Figures 3.5a. The mass and volume fractions of particles, f_{43}, and f_{44} in different size range are summarized in Table 3.1. Figure 3.4d shows that the mass fraction of organics was relatively large in small diameters and the mass fraction of inorganics tended to be larger at larger diameters. Further, the larger the diameter, the smaller f_{43}, a characteristics peak of HOA. An opposite size dependence was observed for f_{44}, a characteristics peak of OOA (Figure 3.5c and Table 3.1). These results are explained by the dominance of freshly emitted primary components (e.g., HOA and BC) in the Aitken mode range and the presence of secondary components (e.g., OOA and inorganics) in the accumulation mode range, as reported for urban aerosols [*Takegawa et al.,* 2006; *Kondo et al.,* 2007]. The time series of the ratios of OM/OC, O/C, and H/C is presented in Figures 3.5b. The mean ± SD of OM/OC, O/C, and H/C were 1.62 ± 0.09, 0.37 ± 0.07, and 1.56 ± 0.08, respectively. The mean value of OM/OC was in the range reported for ambient aerosols, from 1.6 (in urban areas) to 2.1 (in non-urban areas) [*Pang et al.,* 2006].

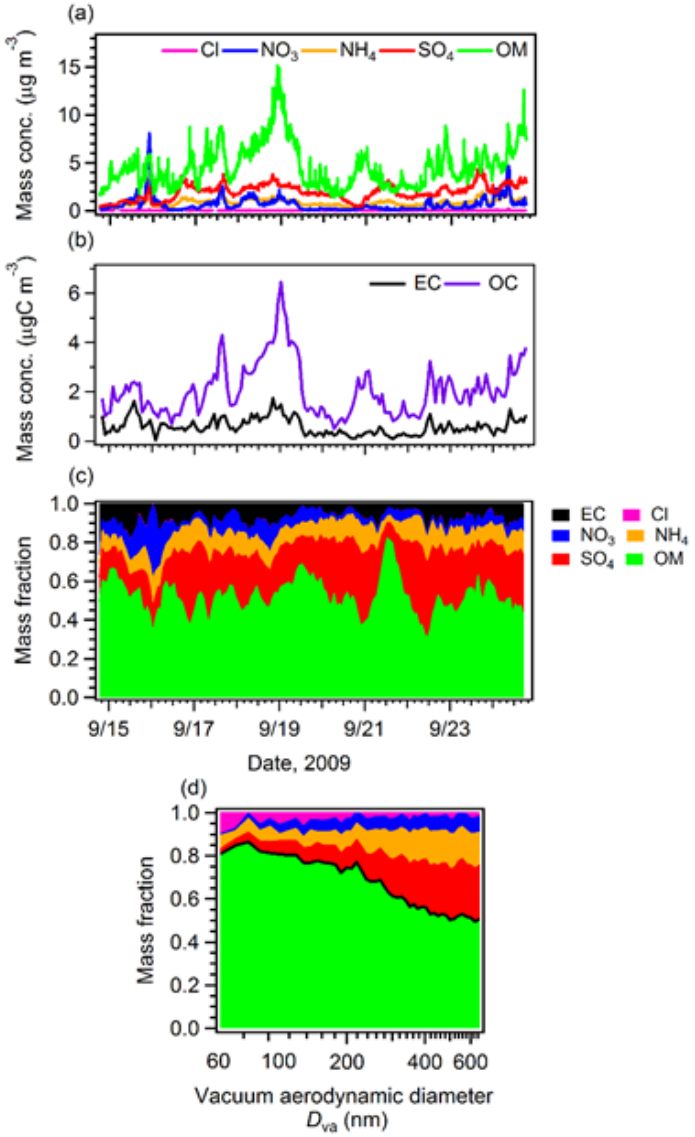

Figure 3.4. Time series of (a) the mass concentrations of non-refractory submicron ($NR\text{-}PM_1$) components, (b) the mass concentrations of EC and OC, and (c) the mass fractions of $NR\text{-}PM_1$ components and EC. (d) The mass fractions from the average of the size-resolved mass distributions of $NR\text{-}PM_1$ components.

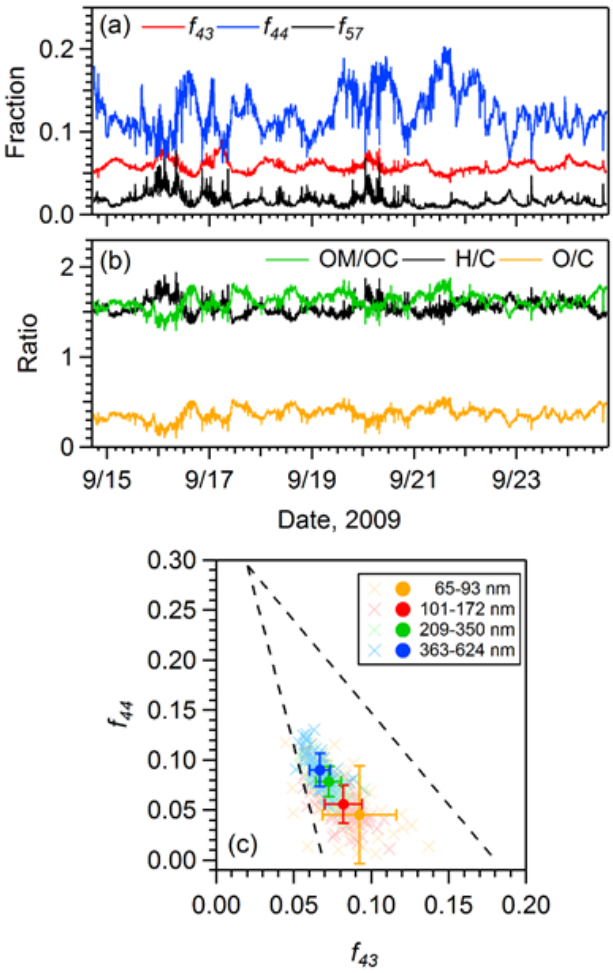

Figure 3.5. (a) Time series of f_{43}, f_{44}, and f_{57} from the AMS mass spectra. (b) Time series of OM/OC (mass ratio), and H/C and O/C (molar ratio) calculated from the AMS mass spectra collected in the V mode. (c) A scatterplot of f_{44} versus f_{43} for different size ranges. Crosses represent individual values, and solid circles and bars represent the mean and the standard deviation for respective size ranges. The dashed lines are the guidelines from *Ng et al.,* [2010, 2011].

Table 3.1. Values associated with chemical composition.

d_{va} ($d_{p,dry}$), nm	f_{org}[a]	ε_{org}[a]	f_{44}[a]	f_{43}[a]
65-93 (60)	0.77 ± 0.13	0.86 ± 0.08	0.053 ± 0.024	0.085 ± 0.018
101-172 (100)	0.72 ± 0.09	0.81 ± 0.07	0.054 ± 0.018	0.080 ± 0.011
209-350 (200)	0.48 ± 0.09	0.69 ± 0.08	0.078 ± 0.015	0.072 ± 0.008
363-624 (359)	0.49 ± 0.09	0.59 ± 0.09	0.090 ± 0.017	0.067 ± 0.007
all[b]	0.65 ± 0.15	0.74 ± 0.13	0.079 ± 0.015	0.071 ± 0.008

[a] Mean ± SD.
[b]Values obtained by using all data points in four size ranges.

3.4. Size-resolved distributions of hygroscopic growth factors

The average of two-dimensional g distributions with axes of $d_{p,dry}$ and g ($d_{p,dry}$: 24.1–359 nm, $0.8 \leq g \leq 2.2$) and that normalized are presented in Figures 3.6a and 3.6b, respectively. In Figure 3.6b, the size-resolved mean g for $0.8 \leq g \leq 2.2$, $0.8 \leq g < 1.1$, and $1.1 \leq g \leq 2.2$ (g_m ($d_{p,dry}$), g_l ($d_{p,dry}$), and g_h ($d_{p,dry}$), respectively) are also presented. Other parameters related to hygroscopicity of particles (for selected 8 dry diameters) are summarized in Table 3.2. As seen in Figure 3.5, the distribution of g was on average characterized as bimodal with less and more hygroscopic modes. Bimodal g distributions, as observed in this study, were commonly observed in urban environments [*McFiggans et al.,* 2006; *Massling et al.,* 2009]. The mean ± SD of g_m and κ_{HTDMA} from 24 to 359 nm were 1.27 ± 0.08 and 0.22 ± 0.06, respectively. The mean κ_{HTDMA} (0.22) in this study is within the range of κ obtained from several other observations (0.3 ± 0.1) [*Andreae and Rosenfeld,* 2008] and from a model calculation (0.27 ± 0.21 under super-saturated condition) [*Pringle et al.,* 2010] for continental sites. Further, it is similar to κ

of Asian continental aerosols from a model calculation (0.22 ± 0.15 under super-saturated condition) [*Pringle et al.,* 2010] and from some observations at urban sites (0.12–0.27 using HTDMA) [*Jurányi et al.,* 2013]. Although a caution should be made on the fact that κ under sub- and super-saturated conditions are not identical, the above comparison shows that the mean κ from this study were close to κ for urban and continental aerosols in literature.

The time series of the g distributions of particles with the values of g_m, g_l, g_h at 50, 102, 209, and 359 nm are presented in Figures 3.7a–3.7d. As described in Figure 3.6, the distributions of g in the small (50, 102 nm) and large (209, 359 nm) diameters had bimodal characteristics in most of the time, indicating the externally-mixed conditions of the aerosols. As presented in Table 3.2, both g_m and κ_{HTDMA} tended to be larger at larger diameters. The g_h values were substantially size-dependent as g_m and κ_{HTDMA}, whereas g_l values were not. The g_m at 8 sizes in Table 3.2, all correlate substantially with g_h (r: 0.55–0.92), whereas the correlations with g_l were weakly negative (r: −0.07 – −0.23); the result indicates that the temporal variations of the g distributions of more hygroscopic particles ($1.1 \leq g \leq 2.2$) contributed more strongly to the variation of g_m than those of less hygroscopic particles. The variations of the number fractions of more hygroscopic particles should also contributed to the variation of g_m, as suggested from the correlations between g_m and the fractions at 8 sizes in Table 3.2 (r: 0.66–0.89). The time series of the standard deviation of the g distributions (σ_g), which explains the width of less and more hygroscopic modes and indicates the heterogeneity of hygroscopicity of particles, is also presented in Figure 3.7, which will be discussed the relation to the CCN activation of particles later.

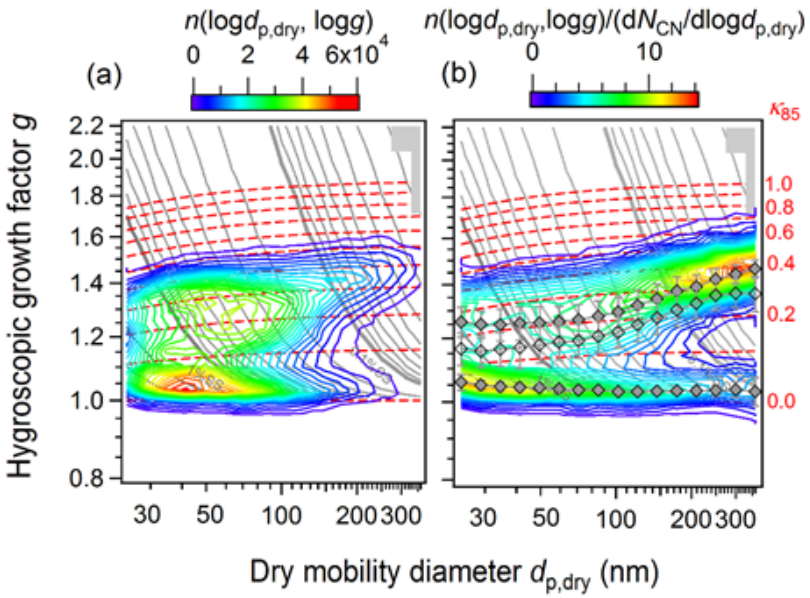

Figure 3.6. The Averages of (a) two-dimensional distribution of the number concentrations of aerosol particles as a function of hygroscopic growth factors (g) and dry mobility diameter ($d_{p,dry}$) at 85% RH and (b) normalized distributions by N_{CN}. The open and solid symbols in 4b represent the mean g in the range of $0.8 \leq g \leq 2.2$ and those in the ranges of $0.8 \leq g < 1.1$ and $1.1 \leq g \leq 2.2$, respectively. The bars represent the standard deviation. The dashed red lines represent contours of κ at 85% RH (κ_{85}). The gray contours show critical SS estimated from the κ-Köhler theory [*Mochida et al.*, 2011].

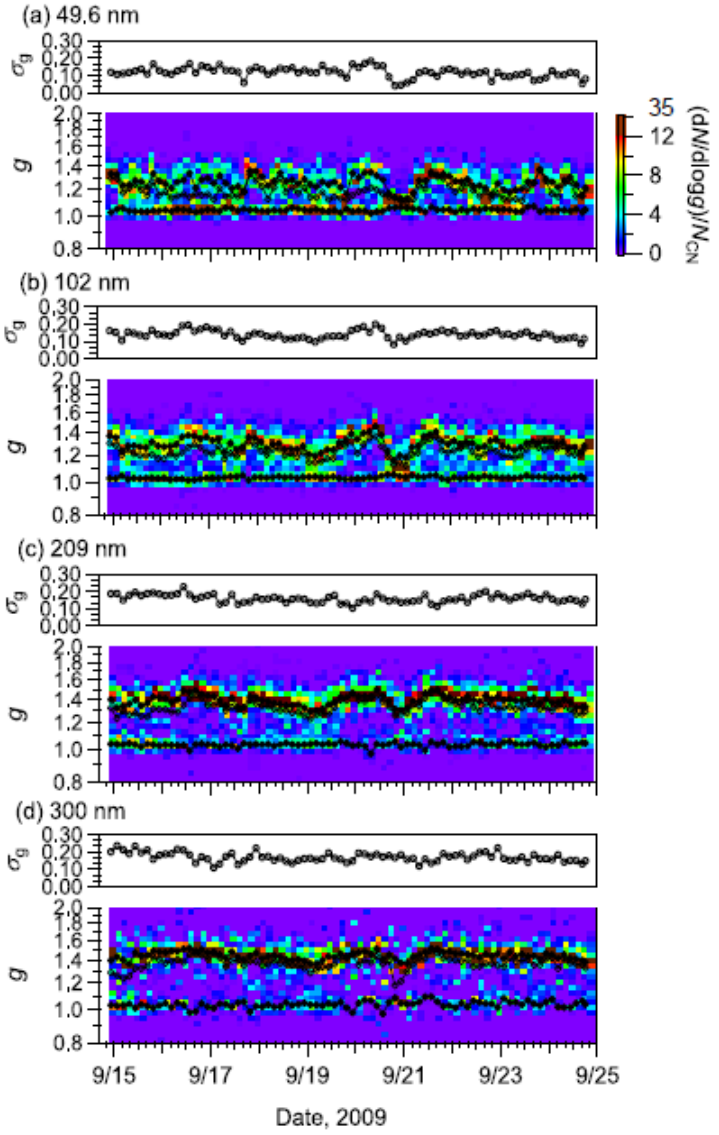

Figure 3.7. Time series of g distributions and the standard deviation σ_g at 85% RH for $d_{p,dry}$ of (a) 49.6 nm, (b) 102 nm, (c) 209 nm, and (d) 300 nm. The open and solid symbols represent the mean g in the range of $0.8 \leq g \leq 2.2$ and those in the ranges of $0.8 \leq g < 1.1$ and $1.1 \leq g \leq 2.2$, respectively.

Table 1. Values associated with the hygroscopicity of aerosol particles at 85% RH[a].

$d_{p,dry}$ (nm)	g_m[b]	g_l[c]	g_h[d]	σ_g[e]	g_{m_water}[f]	κ_{HTDMA}[g]
28.9	1.17 ± 0.05	1.05 ± 0.02	1.25 ± 0.05	0.11 ± 0.03	1.18 ± 0.05	0.17 ± 0.03
49.6	1.19 ± 0.06	1.04 ± 0.01	1.26 ± 0.06	0.12 ± 0.03	1.20 ± 0.06	0.17 ± 0.03
71	1.21 ± 0.06	1.04 ± 0.01	1.27 ± 0.06	0.13 ± 0.03	1.22 ± 0.06	0.17 ± 0.03
102	1.24 ± 0.05	1.03 ± 0.01	1.30 ± 0.06	0.14 ± 0.02	1.26 ± 0.06	0.19 ± 0.02
146	1.29 ± 0.06	1.03 ± 0.01	1.35 ± 0.06	0.15 ± 0.02	1.31 ± 0.06	0.24 ± 0.03
209	1.34 ± 0.06	1.03 ± 0.01	1.40 ± 0.05	0.16 ± 0.02	1.36 ± 0.05	0.28 ± 0.03
300	1.38 ± 0.06	1.04 ± 0.02	1.45 ± 0.04	0.17 ± 0.03	1.40 ± 0.05	0.32 ± 0.03
359	1.39 ± 0.07	1.03 ± 0.04	1.47 ± 0.04	0.18 ± 0.04	1.41 ± 0.05	0.33 ± 0.03

[a] Mean ± SD.

[b] Mean hygroscopic growth factors for particles in the range of $0.8 \leq g \leq 2.2$.

[c] Same as b, but for particles in the range of $0.8 \leq g < 1.1$.

[d] Same as b, but for particles in the range of $1.1 \leq g \leq 2.2$.

[e] Standard deviation of g distributions in the range of $0.8 \leq g \leq 2.2$.

[f] Average hygroscopic growth factors from equation 3.

[g] The hygroscopicity parameter calculated from g_{m_water}.

The number-size distributions and number fractions of particles in four different ranges of g were calculated to investigate the size dependence of particles hygroscopicity (Figure 3.8). In the Aitken mode range, particles in the range of $0.8 \leq g < 1.25$ was dominant (mean: 65%). By contrast, in the accumulation mode range, particles in the range of $1.25 \leq g < 2.2$ was dominant (mean: 70%). A similar characteristics was found in a different urban site: the fraction of less hygroscopic and insoluble particles was relatively large in the Aitken mode range and that more hygroscopic and soluble particles was relatively large in the accumulation mode range in Beijing [*Massling et al.,* 2009].

The dominance of particles with relatively low hygroscopicity ($0.8 \leq g < 1.25$) in the small diameter range and that of relatively high hygroscopicity ($1.25 \leq g < 2.2$) in the large diameter range is explained in view of their chemical composition, sources, and

aging processes. The size-resolved chemical composition in Figure 3.4 and charateristics of size-resolved hygroscopicity in Figures 3.5–3.7 indicate that Aitken mode particles were composed of freshly emitted organics such as POA and HOA with low hygroscopicity and accumulation mode particles were composed of inorganic salts and oxidized organics such as SOA and OOA with high hygroscopicity. Further, freshly-emitted BC might be regarded as a part of particles with relatively low hygroscopicity. The above assignment is similar to that by *Massling et al.* [2009], who reported that nearly hydrophobic (g: 0.96–1.07) and less hygroscopic particles (g: 1.06–1.29) were composed of freshly emitted soot and carbonaceous particles and that more hygroscopic particles (g: 1.26–1.62) were composed of secondary formed sulfate. Further, the assignment is also similar to that by *Mochida et al.* [2008], who reported that particle with $g<1.11$ was associated with primary compounds and that particle with $g>1.29$ was associated with secondary or oxidized compounds based on an observation in summer in Tokyo. Note that g of smaller particles were presumably affected by the curvature effect (Kelvin effect) more strongly (see the contour lines of κ_{85} in Figure 3.6), which may also contribute to the size-dependence of the hygroscopicity of particles in Figure 3.8. Whereas intermediately hygroscopic particles ($1.25 \leq g < 1.4$) in addition to less hygroscopic particles ($g<1.25$) were dominant in the Aitken mode range in Nagoya in summer 2010 [*Kawana et al.,* 2014], the fraction of intermediately hygroscopic particles was on average small in this study (0.85, 0.85, and 0.91 times at 30, 50, and 71 nm). In summer 2010, aged hygroscopic particles and maritime aerosol particles may have been transported substantially to the observation site because air mass trajectories are originated mainly from China and Pacific Ocean. By contrast, the contribution of such particles may have been relatively small because the observed site was influenced

by air masses originated mainly from surrounding areas in Japan.

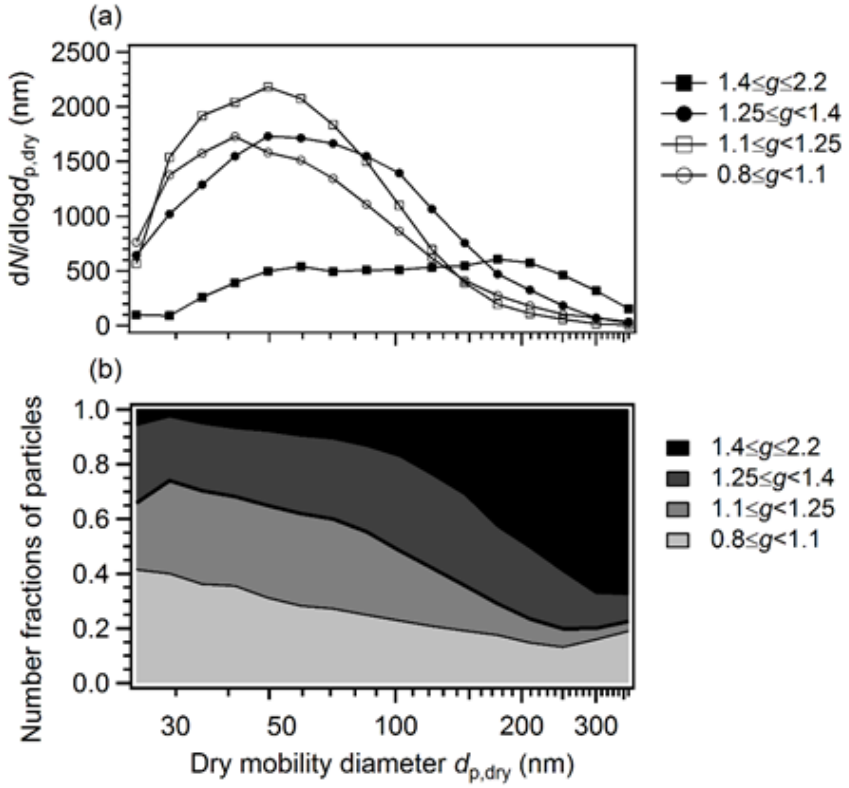

Figure 3.8. The Averages of (a) the number-size distributions and (b) the number fractions of aerosol particles in the ranges of $0.8 \leq g < 1.1$, $1.1 \leq g < 1.25$, $1.25 \leq g < 1.4$, and $1.4 \leq g \leq 2.2$.

3.5. Hygroscopicity parameter of organics

The hygroscopicity parameter of organics (κ_{org}) was calculated by two different methods from the HTDMA-derived hygroscopicity of particles (κ_{HTDMA}) and the chemical composition. One is with the regression of κ_{HTDMA} versus the mass fractions of organics (f_{org}) [*Shinozuka et al.,* 2009; *Gunthe et al.,* 2011; *Rose et al.,* 2011] and the other is with the ZSR method using volume fractions of organics (ε_{org}) [*Mei et al.,* 2013a, 2013b]. In both calculations, particles were assumed to be composed of organics,

inorganic salts (ammonium sulfate and ammonium nitrate) and EC based on the results from the AMS and EC/OC analyzer (Figure 3.4). The κ_{org} from κ_{CCNC} were not used for the analysis here, but are presented in the appendix. From the calculations, size-resolved κ_{org} at $d_{p,dry}$ of 60, 100, 200, and 359 nm were derived. The composition in the ranges of 65−93, 101−172, 209−350, and 363−624 nm in d_{va} were considered to be those at 60, 100, 200, and 359 nm in $d_{p,dry}$, based on the equation in *Decalro et al.* [2004];

$$d_{va} = d_{ve} \bullet \frac{\rho_p}{\rho_0} \bullet \frac{1}{\chi_v} \tag{11}$$

Here, ρ_p is the particle density, ρ_0 is the standard density (1 g cm^{-3}), and χ_v is the dynamic shape factor in the free-molecular regime. Particle was assumed to be spherical (χ_v: 1.0) and the particle density was assumed to range from ~1.0 to ~1.8 g cm^{-3}. Further, κ_{org} values were obtained by using all points at four $d_{p,dry}$ (size-averaged κ_{org}). The regressions of κ_{HTDMA} versus f_{org} are depicted in Figure 3.9a. The calculated κ_{org}, the values of the regression lines at f_{org} of unity, are summarized in Table 3.3. The size-resolved κ_{org} were determined to be 0.08–0.12 (r: 0.41–0.80). The size-averaged κ_{org} from a single regression line for data from all four $d_{p,dry}$ was determined to be 0.108 (r: 0.80). The κ_{org} values show moderately hygroscopic nature of the organics, and are similar to those reported from the regression method for urban aerosols in Asia (0.06 in *Gunthe et al.*[2011] and 0.10 in *Rose et al.*[2011]) and lower than those for aerosols over Mexico City (0.13–0.21) [*Shinozuka et al.,* 2009]. The κ_{org} for every 3h were obtained from the ZSR method using the equation:

$$\kappa_{org} = \frac{\kappa_{HTDMA} - (\kappa_{inorg}\varepsilon_{inorg} + \kappa_{EC}\varepsilon_{EC})}{\varepsilon_{org}} \tag{12}$$

where, κ_{org}, κ_{inorg}, and κ_{EC} are the hygroscopicity parameters of organics, inorganic salts,

and EC, respectively, and ε_{org}, ε_{inorg}, and ε_{EC} are their respective volume fractions. The ε_{EC} was calculated from the mass fraction of EC in total submicrometer aerosol mass as defined by the sum of NR-PM_1 and EC, and κ_{EC} was assumed to be zero. The κ_{inorg} at 85% RH (ammonium sulfate and ammonium nitrate) were calculated to be 0.52–0.56 for 60–359 nm by the κ-Köhler equation with the Pitzer model. The κ_{org} from the ZSR method are presented in Figure 3.9b. The size-resolved κ_{org} for 60– 359 nm were 0.14–0.23. The size-averaged κ_{org}, represented by the mean of κ_{org} at all four $d_{p,dry}$, was 0.191. Although the values are higher than those from the regression method, they also suggest moderately hygroscopic nature of organics. The calculated mean κ_{org} were relatively low in small particles and relatively high in large particles: ~0.15 for 50 and 100 nm particles and ~0.23 for 200 and 359 nm particles.

The relationship of κ_{org} to f_{44} and O/C was investigated as some previous studies [*Aiken et al.,* 2008; *Chang et al., 2010*]. The regressions resulted in the equations: $\kappa_{org} = 1.300 \times f_{44} - 0.101$ and $\kappa_{org} = 0.193 \times \text{O/C} - 0.070$ (Figures 3.9c and 3.9d). The κ_{org} versus f_{44} or O/C show positive, but weak correlations (r: 0.42 and r: 0.27, respectively). Whereas the correlations were weaker than those in some studies [*Dupplissy et al.,* 2011; *Mei et al.,* 2013a], the absence of strong correlations is not unique; weak correlations were also reported from other studies [*Moore et al.,* 2011; *Lathem et al.,* 2013]. A fully quantitative comparison is not possible because the degrees of correlations might be affected by the uncertainty of κ_{org} and f_{44} or O/C in respective studies. In this study, the uncertainty might in part be caused by the assumption of the volume fractions of EC in different sizes and the assumption of the size ranges in d_{va}.

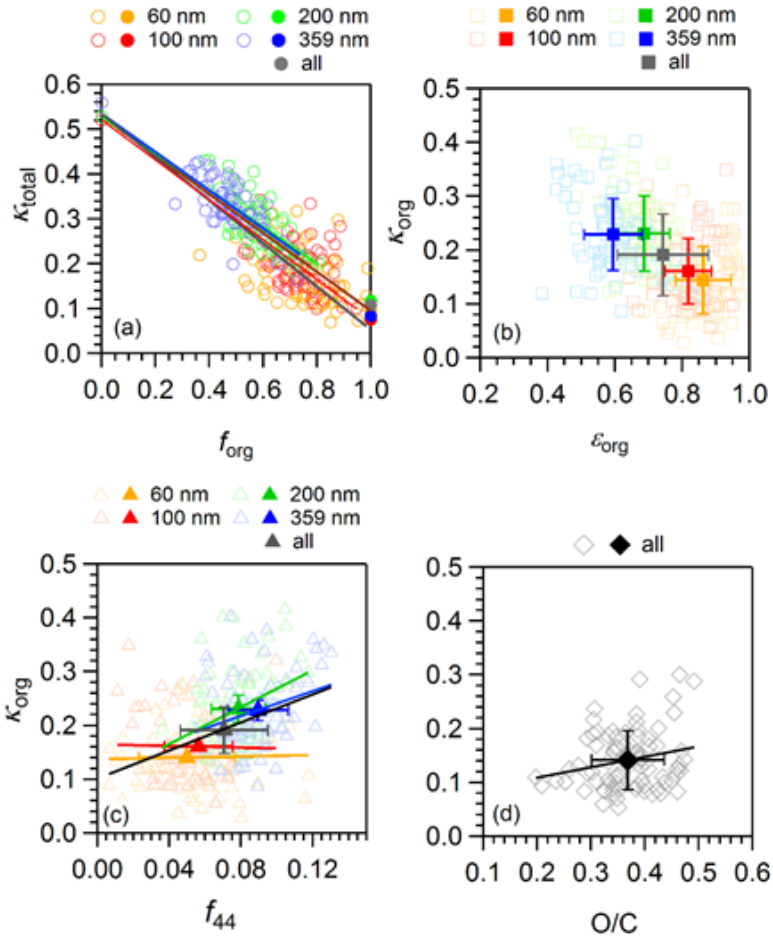

Figure 3.9. (a) The scatterplot of HTDMA-derived hygroscopicity parameter (κ_{HTDMA}) versus organics mass fractions (f_{org}). The solid squares represent size-resolved and size-averaged hygroscopicity parameters of organics (κ_{org}) from the regression lines. (b–d) The scatterplot of (b) κ_{org} from the ZSR method versus organics mass fractions (ε_{org}), (c) ε_{org}-derived κ_{org} versus f_{44}, and (d) ε_{org}-derived κ_{org} versus O/C. The solid lines in 7a, 7c, and 7d represent the regression lines. Open symbols in 8b and 8c represent individual values, and the solid symbols and bars represent the mean values of size-averaged (all) and size-resolved κ_{org} and the standard deviation, respectively.

Table 3.3. κ of organics (κ_{org}) and the correlation coefficients of κ_{org} versus f_{44} and O/C.

d_{va} ($d_{p,dry}$), nm	κ_{org}		correlation coefficients of ε_{org}-derived κ_{org}	
	f_{org}-derived[a]	ε_{org}-derived[b]	f_{44}	O/C
65-93 (60)	0.095 (0.41)	0.144 ± 0.063	0.05	NA
101-172 (100)	0.076 (0.64)	0.161 ± 0.061	0.02	NA
209-350 (200)	0.117 (0.79)	0.231 ± 0.070	0.37	NA
363-624 (359)	0.083 (0.80)	0.229 ± 0.067	0.29	NA
all[c]	0.108 (0.80)	0.191 ± 0.076	0.42	0.27

[a]Values in parentheses are correlation coefficients from the regression analysis.

[b]Mean ± SD.

[c]Values obtained by using all data points in four size ranges.

3.6. CCN activity

The time series of the CCN activated fraction (F_{act}) and d_{act} at 0.12%, 0.24%, and 0.43% SS are presented in Figures 3.10a–3.10c. Parameters of CCN activation derived from fitted CCN efficiency spectra (F_{act}, d_{act}, and σ), CCN fractions at maximum diameter of 359 nm (F_{max}), and σ/d_{act} are summarized in Table 3.4. Both F_{act} and F_{max} have large mean (>0.9) and small SD, indicating the fractions of CCN-inactive particles well above d_{act} were in general small. However, F_{act} and F_{max} were low (<0.7) in the beginning of the observation period (on 14 September), indicating the substantial presence of CCN-inactive particles even well above d_{act}. The mass fraction of EC was large (up to 30%) in this period as compared to the averaged (7%), suggesting that the presence of fresh soot particles resulted in the low F_{act} and F_{max}. This is supported by the report by *Rose et al.* [2011] that suggested CCN-inactive particles at large diameter (~300 nm) might be fresh soot particles based on the analysis of CCN activity and volatility of aerosols near a mega-city in China.

The mean values of the fitting parameters, F_{act}, d_{act}, and σ, and the derivated values of σ/d_{act} and κ_{CCNC} are presented in Figure 3.11. The mean ± SD of d_{act} were 142 ± 11, 95 ± 8, and 69 ± 8 nm at 0.12%, 0.24%, and 0.43% SS, respectively, and those of σ were 19.6 ± 6, 12.8 ± 4, and 9.7 ± 5 nm at 0.12%, 0.24%, and 0.43% SS, respectively. The σ/d_{act} value is a measure of the heterogeneity of aerosol particles: the higher the value, more externally-mixed the aerosol [*Rose et al.*, 2008, 2010]. The σ/d_{act} values averaged for the values of respective SS conditions were ~0.13, and the dependence on SS, and thus $d_{p,dry}$ (69–142 nm) was not evident. The σ/d_{act} values were substantially larger than the values of pure ammonium sulfate particles, i.e., particles composed of a single component (0.05, 0.03, and 0.02 at 112, 71, and 50 nm, respectively), suggesting that ambient particles were inhomogeneous even for a specific size, as expected from g distributions (Figure 3.7). The σ/d_{act} values correlates moderately with the dispersion of hygroscopicity of CCN-activated particles expressed as σ_g in the range of $1.1 \leq g \leq 2.2$ (r: 0.52–0.60 at 0.12–0.43% SS), indicating that the ununiformity of particle hygroscopicity affect to the CCN activation of particles. The mean ± SD of κ_{CCNC} calculated from d_{act} were 0.32 ± 0.07, 0.26 ± 0.06, and 0.23 ± 0.08 at 0.12%, 0.24%, and 0.43% SS, respectively. The result indicates the tendency that the smaller the particles were, the lower the hygroscopicity were, as in the case of κ_{HTDMA}. The time series of N_{CN}, N_{CCN}, and N_{CCN}/N_{CN} under SSs are shown in Figures 3.10d and 3.10e. The mean ± SD of N_{CCN} at 0.12%, 0.24%, and 0.43% were 391 ± 98, 925 ± 429, and 1676 ± 996 cm^{-3}, respectively. The mean ± SD of N_{CCN}/N_{CN} at 0.12%, 0.24%, and 0.43% were 0.11 ± 0.04, 0.24 ± 0.07, and 0.43 ± 0.11, respectively. In Figure 3.11, the fitting parameters and derivated values in other sites in Asia are also presented for comparison. Parameters and values in this study were similar to those in previous studies [*Rose et al.,* 2010;

Gunthe et al., 2011]. In the case of d_{act}, the dependence on SS suggests that the values from this study were higher than those of aged particles in Asian remote sites [*Kuwata et al.,* 2008; *Mochida et al.,* 2010].

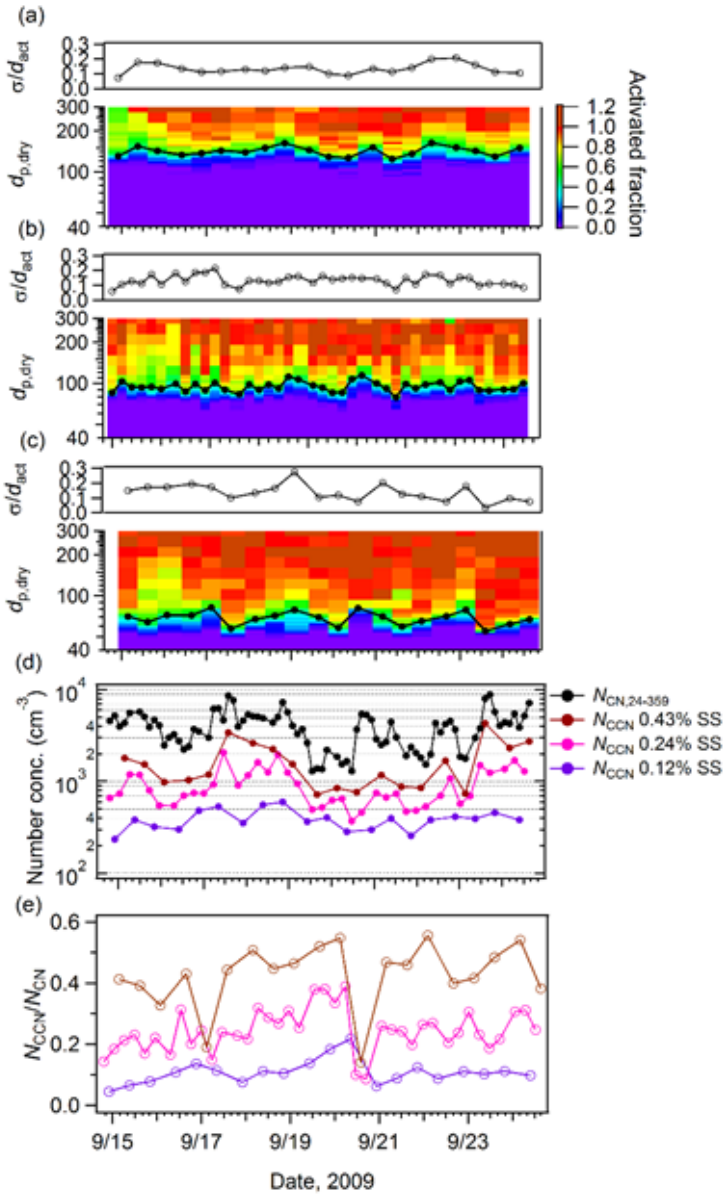

Figure 3.10. (a–c) Time series of size-resolved CCN activated fraction at $d_{p,dry}$ and σ/d_{act} under (a) 0.12%, (b) 0.24%, and (c) 0.43% SS. (d) Time series of the number concentrations of CCN and CN from 24 to 359 nm (N_{CCN} and N_{CN}). (e) Time series of the ratios of N_{CCN} to N_{CN} under 0.12%, 0.24%, and 0.43% SS. Solid black circles in figures a–c represent CCN activation diameters.

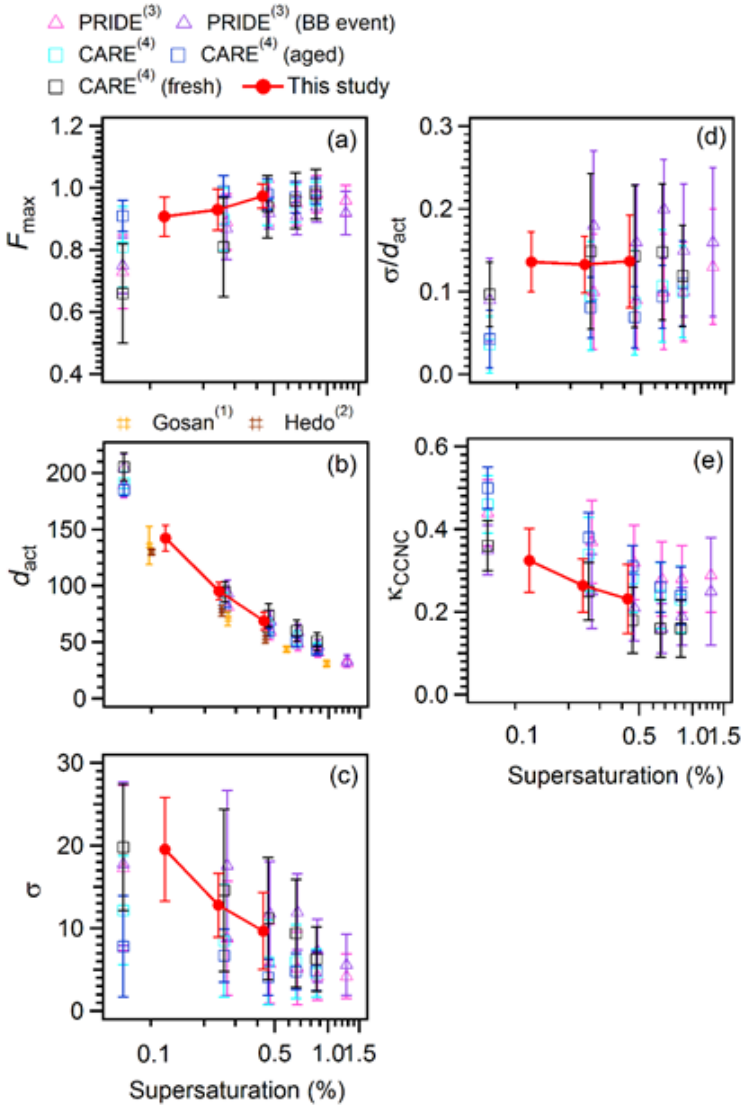

Figure 3.11. Parameters associated with CCN activation: (a) F_{max}, (b) d_{act}, (c) σ, (d) σ/d_{act}, and (e) κ_{CCNC}. Solid red circles and bars represent the mean values and the standard deviation, respectively. The figures also show the values from previous studies reported by (1) *Kuwata et al.* [2008], (2) *Mochida et al.*[2010], (3) *Rose et al.* [2010], and (4) *Gunthe et al.*[2011].

Table 3.4. Values obtained by the fitting of CCN efficiency spectra[a].

SS	F_{act}	F_{max}	d_{act}	σ	σ/d_{act}	κ_{CCNC}[b]	$\kappa_{CCNC}/\kappa_{HTDMA}$	$\kappa_{CCNC}/\kappa_{HTDMA}$*
0.12%	0.91 ± 0.06	1.01 ± 0.11	142.3 ± 11	19.6 ± 6.3	0.136 ± 0.040	0.324 ± 0.070	1.44 ± 0.13	1.27 ± 0.12
0.24%	0.93 ± 0.07	1.00 ± 0.11	95.3 ± 8	12.8 ± 3.9	0.133 ± 0.030	0.264 ± 0.060	1.39 ± 0.21	1.32 ± 0.18
0.43%	0.97 ± 0.04	1.04 ± 0.04	69.0 ± 8	9.7 ± 4.6	0.125 ± 0.070	0.232 ± 0.080	1.25 ± 0.14	1.21 ± 0.13
all[c]							1.37 ± 0.19	1.28 ± 0.16

[a]Mean ± SD.

[b]Hygroscopicity parameter calculated from d_{act}.

[c]Values obtained by using all data points at 0.12%, 0.23%, and 0.43% SS.

The CCNC-derived κ under super-saturated conditions, κ_{CCNC}, are compared to the HTDMA-derived κ under sub-saturated conditions, κ_{HTDMA} (Figure 3.12a and Table 3.4). In this analysis, the similar ranges of $d_{p,dry}$ are selected for comparison because both values are size-dependent (0.12% SS: 131–151 nm and 142 ± 11 nm, 0.24% SS: 88–102 nm and 95 ± 8 nm, 0.43% SS: 64–74 nm and 69 ± 8 nm for κ_{HTDMA} and κ_{CCNC}, respectively). The κ_{CCNC} was higher than κ_{HTDMA} under all SS conditions, and the degree of the differences calculated from all data pairs at three SS (n = 80) was +37% ± 19%. The degree of the difference was similar to that of urban aerosols in Germany (+37%) [*Wu et al.,* 2013]. One possible reason of the difference is the dependence of κ of chemical components on the concentration of the solution, in other words, the saturation ratio of water vapor. For instance, κ_{CCNC} of ammonium sulfate particles is ~18% higher than κ_{HTDMA}, according to the mean values of κ_{HTDMA} (0.51) and κ_{CCNC} (0.60) for three SSs from the κ-Köhler model with the Pitzer equation. To assess this effect by inorganic salts, the sum of κ_{HTDMA} and the estimated increase of κ at supersaturated conditions by inorganic salts were calculated as a hypothetical hygroscopicity κ_{HTDMA}^*;

$$\kappa_{HTDMA}^* = \kappa_{HTDMA} + \varepsilon_{inorg}(\kappa_{inorg\_SS} - \kappa_{inorg\_85}) \quad (13)$$

where κ_{inorg_85} and κ_{inorg_SS} are the κ of inorganic salts (ammonium sulfate and ammonium nitrate) at 85% RH and at 0.12%–0.43% SS, respectively. The mean (ranges) of κ_{inorg_SS} and κ_{inorg_85} from the ZSR method with a κ-Köhler model incorporating the Pitzer equation are 0.54 (0.52–0.56) at 85% RH and 0.63 (0.61–0.66) at 0.12%–0.43% SS, respectively; κ of inorganic salts under super-saturated conditions are ~20% higher than those at 85% RH. The comparison of κ_{HTDMA}^{*} and κ_{CCNC} is presented in Figure 3.12b and Table 3.4. The +28% ± 16% difference remains for κ_{HTDMA}^{*} and κ_{CCNC}, based on the averages of the ratios of κ_{CCNC} to κ_{HTDMA}^{*} at three SS.

It is likely that organics contribute to the remaining difference. Whereas some previous studies reported that κ_{HTDMA} and κ_{CCNC} agreed well (±20%, [*Carrico et al.,* 2008]; [*Dupplissy et al.,* 2008]), they disagreed in other studies (20%–50% [*Massoli et al.,* 2010] and 37% [*Wu et al.,* 2013]). The reasons for the difference were discussed based on both laboratory and field studies; they are a reduction of surface tension, presence of sparingly soluble materials (<90% RH), insufficient expression of the dependence of the activity coefficient of water on the concentration of the solution at high RH (>95%) [*Prenni et al.,* 2007; *Wex et al.,* 2009; *Good et al.,* 2010a, 2010b; *Massoli et al.,* 2010; *Kristensen et al.,* 2012]. The large fraction of organics in this study might be preferable for these effects of organics, and resulted in the difference between κ_{HTDMA}^{*} and κ_{CCNC}. Calculations with the assumptions of internally-mixed, spherical particles, and co-condensation process of semi-volatile compounds might also be the causes of the difference [*Dusek et al.,* 2011; *Jung et al.,* 2011; *Topping and McFiggans,* 2012].

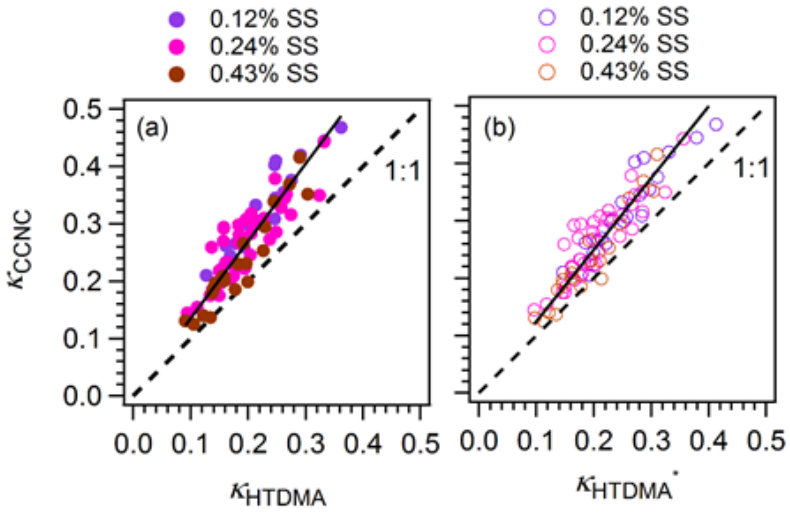

Figure 3.12. (a) The scatterplot of κ_{CCNC} versus κ_{HTDMA} under 0.12%, 0.24%, and 0.43% SS. Solid circles and the solid line represent κ_{CCNC} plotted against κ_{HTDMA} and the regression line constrained through the origin, respectively. (b) The scatterplot of κ_{CCNC} versus κ_{HTDMA}^{*} under 0.12%, 0.24%, and 0.43% SS. Open circles and the solid line represent κ_{CCNC} plotted against κ_{HTDMA}^{*} and the regression line constrained through the origin, respectively.

3.7. Importance of the hygroscopicity of organics and the variations of particle hygroscopicity with time and size

N_{CCN}/N_{CN} is predicted and compared with the measured to investigate the contributions of the hygroscopicity of organics and the variations of g with time and size, and g distributions to N_{CCN}. The results with the consideration of the hygroscopicity of organics are presented in Figures 3.13a–3.13c and Table 3.5. The predicted N_{CCN}/N_{CN} is largely underestimated if κ_{org} is assumed to be zero, i.e., organics is insoluble (Figure 3.13a); the averages of the differences of the ratios of the predicted to the measured N_{CCN}/N_{CN} from unity at 0.12%, 0.24%, and 0.43% SS (mean relative differences) were from −64% to −45% (Table 3.5). The relative standard deviation

(RSD) of the ratios of the predicted to the measured N_{CCN}/N_{CN} for three SS were from 17% to 81% (Table 3.5). If size-averaged κ_{org} derived from the regression analysis (0.11) and the ZSR method (0.19) are applied regardless of the particle size, the mean relative differences for three SS become small (−17% to −8% and −2% to +14%, respectively, Figure 3.13b). Further, the RSD also become small (Table 3.5). In the case that size-resolved κ_{org} derived from the regression method (0.08–0.12) and the ZSR method (0.14–0.23) are applied, the degree of the agreement is not largely different from those using size-averaged κ_{org} (Figure 3.13c and Table 3.5). The better agreement with consideration of κ_{org} estimated in this study supports the finding that organics were hygroscopic to some degree (section 3.4) and contributed to N_{CCN}. Note that the predicted N_{CCN}/N_{CN} agreed to the measured with the mean relative differences from −18% to −9% and those from −2% to +17%, respectively, if κ_{org} are assumed to be 0.1 and 0.2 based on a literature value of κ_{org} (0.1 ± 0.1) [*Rose et al.,* 2010].

Predictions with consideration of the variations of g with time and size, and g distributions are also assessed (Figures 3.14a–3.14e and Table 3.6). Although the predicted N_{CCN}/N_{CN} roughly agreed to the measured if a size- and time-averaged g is used as a representative value (mean relative differences: −30% to +10% for three SS), the RSD were large (15%−17%, Figure 3.14a). In the case that time-resolved but size-averaged g are applied (Figure 3.14b), the mean relative differences of the predicted N_{CCN}/N_{CN} from the measured are not largely different (−27% to +7%), but the RSD are smaller (10%−13%). If size-resolved but time-averaged g are applied (Figure 3.14c), the RSD are not largely different from the case using a size- and time-averaged g (15%−17%), but the mean relative differences at 0.12% and 0.43% SS are much closer to zero (−9% to −1%). Further smaller RSD are obtained if time- and size-resolved g are

considered (7%−10%, Figure 3.14d) or if *g* distributions as well as their time and size dependence are fully considered (6%−9%, Figure 3.14e). Although the predicted N_{CCN}/N_{CN} is slightly underestimated in these cases, the large underestimation in the cases using single *g* and time-resolved *g* at 0.12% SS improves. The above results indicate that the temporal variations and the size dependence of particle hygroscopicity largely controlled the CCN number concentrations.

As discussed for the difference between κ_{HTDMA}^{*} and κ_{CCNC}, the remaining ~15% differences in the cases using time- and size-resolved *g* distributions (Figures 3.14e) are possibly explained by the effects associated with organics, i.e., their Kelvin effect (e.g., surface tension reduction) and Raoult effect (e.g., the dissolution of sparingly soluble materials with the increase in RH, and the non-ideal behavior of the solution), as well as other effects and measurement uncertainties. To assess these possibilities, the reduction of surface tension (0%–20%) and the increase in κ by the change of water-vapor conditions from sub- to super-saturation (0%–20%) are assumed in the calculation of N_{CCN}/N_{CN}. Contour plots showing the differences between N_{CCN}/N_{CN} predicted from size-resolved *g* distributions and measured N_{CCN}/N_{CN} at 0.12%, 0.24%, and 0.43% SS are presented in Figure 3.15. The result indicates that the 15% difference in the CCN closure can be explained by the surface tension reduction or a combination of the surface tension reduction and the enhanced solute effect. For instance, ~11% surface tension reduction, and a combination of <10% surface tension reduction and ~20% enhanced solute effect can explain the differences between measured and predicted N_{CCN}/N_{CN}. The ~11% surface tension reduction is possible in the atmosphere, as reported in previous studies: the reduction of surface tension by organics in ambient aerosols was up to >20% [*Facchini et al.,* 1999, 2000; *Fors et al.,* 2010]. Further,

increase in the hygroscopicity of organics from sub- to super-saturated conditions may also be possible as in the case of inorganic salts, given that non-ideal behavior of organic compounds is reported [*Krendenweis et al.,* 2008].

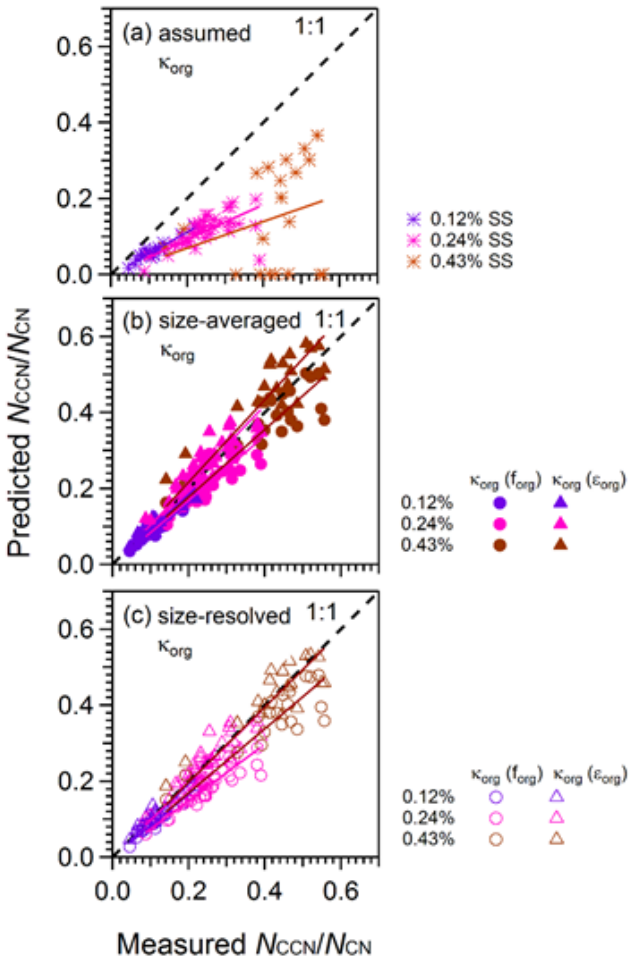

Figure 3.13. (a–c) The N_{CCN}/N_{CN} predicted with (a) κ_{org} of 0, (b) size-averaged κ_{org}, and (c) size-resolved κ_{org} versus the measured N_{CCN}/N_{CN}. Circles and triangles in 11b and 11c represent values predicted from f_{org}-derived and ε_{org}-derived κ_{org}, respectively. Solid lines represent the regression lines constrained through the origin.

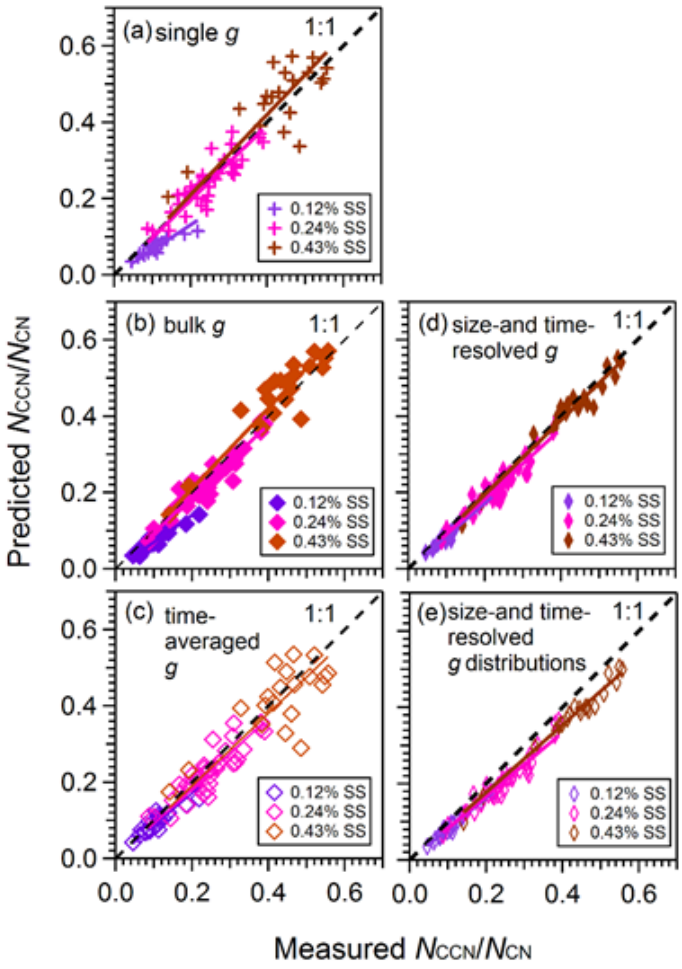

Figure 3.14. (a–e) The N_{CCN}/N_{CN} predicted with considerations of (a) single *g*, (b) size-averaged and time-resolved *g*, (c) time-averaged and size-resolved *g*, (d) size- and time-resolved *g*, and (e) size- and time-resolved *g* distributions versus the measured N_{CCN}/N_{CN}. Solid lines represent the regression lines constrained through the origin.

Table 3.5. The ratios of the predicted N_{CCN}/N_{CN} to measured N_{CCN}/N_{CN}, with different assumptions/considerations of parameters for prediction[a].

SS	κ_{org}: 0	bulk		size-resolved	
		f_{org}	ε_{org}	f_{org}	ε_{org}
0.12%	0.55 (0.17)	0.83 (0.09)	0.98 (0.14)	0.85 (0.11)	1.01 (0.13)
0.24%	0.47 (0.25)	0.86 (0.11)	1.08 (0.13)	0.75 (0.11)	1.01 (0.12)
0.43%	0. 36 (0.81)	0.92 (0.14)	1.14 (0.16)	0.88 (0.14)	1.03 (0.14)

[a] Values with parentheses are the relative standard deviations of the ratios of the predicted N_{CCN}/N_{CN} to the measured.

Table 3.6. The ratios of the predicted N_{CCN}/N_{CN} to measured N_{CCN}/N_{CN}, with different considerations of parameters for prediction.

SS	Single g	Time -resolved g	Size-resolved g	Size-and time-resolved g	Size-and time-resolved g distributions
0.12%	0.70 (0.15)	0.73 (0.13)	0.91 (0.15)	0.86 (0.08)	0.81 (0.07)
0.24%	1.01 (0.15)	0.95 (0.10)	0.94 (0.15)	0.92 (0.10)	0.83 (0.09)
0.43%	1.10 (0.17)	1.07 (0.10)	0.99 (0.17)	0.97 (0.07)	0.88 (0.06)

[a] Values with parentheses are the relative standard deviations of the ratios of the predicted N_{CCN}/N_{CN} to the measured.

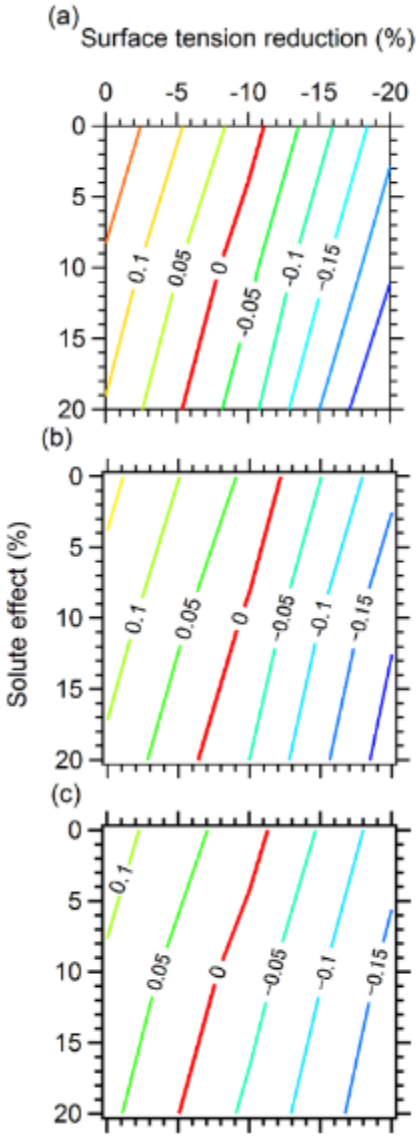

Figure 3.15. Contours representing the differences of N_{CCN}/N_{CN} predicted from size-resolved g distributions to measured N_{CCN}/N_{CN}, with assumed changes in the surface tension reduction and the hygroscopicity (solute effect) at (a) 0.12%, (b) 0.24%, and (c) 0.43% SS.

The results from the CCN closure suggest that the solubility of organics and the externally-mixed condition of the aerosol need to be considered for the accurate prediction of CCN number concentrations. The result is in line with the study by *Ervens et al.* [2010]. They discussed the influence of chemical properties on the prediction of

CCN at six different locations (both urban and remote sites) and suggested that the size-resolved chemical composition or hygroscopicity of particles and organics, and mixing state need to be considered for the prediction near particle sources (e.g., urban sites), while the prediction for remote sites is not influenced by these considerations. Some studies also suggest that consideration of the presence of less hygroscopic particles (i.e., HOA or BC) and their degree of hygroscopicity and mixing state are important for the prediction of CCN at urban sites [*Cubison et al.,* 2008; *Quinn et al.,* 2010]. The results in this study provide an implication for the modeling study on CCN, in particular for urban aerosols, as previous studies do.

3.8. Brief summary of this chapter

The size-resolved *g* distributions, the size-resolved ratios of CCN to CN, the chemical composition, and the number-size distributions of aerosol particles were measured at an urban site in Nagoya, Japan. Bimodal distributions with less and more hygroscopic modes were observed in most cases. The analysis of size-resolved g distributions and chemical composition suggests that less hygroscopic particles with HOA were dominant in the small size range (Aitken mode range) and more hygroscopic particles with OOA, SOA, and inorganic salts were dominant in the large size range (accumulation mode range). The mass fraction of organics in NR-PM_1 particles was large (mean: 56%), in particular in the small size range. The κ of organics was calculated as 0.11–0.19, suggesting that organics was hygroscopic to some degree. The κ values under super-saturated conditions were higher than those under sub-saturated conditions (~37%) and ~28% differences remained after the corrections of the contribution by inorganics. The result suggests that the effects by organics on the

hygroscopicity and CCN activation of particles, i.e., surface tension reduction and the enhancement of the solute at higher RH, are significant. In the CCN closure, the consideration of the hygroscopicity of organics and the variation of g with time and particle size are necessary to explain the CCN number concentrations in Nagoya accurately.

Appendix. Calculation of hygroscopicity of organics from κ_{CCNC}

The size-averaged κ_{org} were determined using the chemical composition of particles in the range of 69–256 nm in d_{va} for particles at d_{act} under 0.12%, 0.24%, and 0.43% SS conditions (69–142 nm). The size-resolved κ_{org} were determined using the chemical composition in the ranges of 75–119, 101–163, and 145–248 nm in d_{va} for particles at d_{act} of 69, 95, and 142 nm, respectively. The κ_{inorg} at three SS conditions were calculated to be 0.61–0.66 for 69–142 nm using the κ-Köhler model with the Pitzer equation. The size-averaged and size-resolved κ_{org} from the regression method were 0.13 and 0.10–0.14, respectively. The size-averaged and size-resolved mean κ_{org} from the ZSR method were 0.23 and 0.21–0.25, respectively. The calculated κ_{org} are weakly correlated (r~0.40) with f_{44}, as with κ_{org} from κ_{HTDMA}. Using the CCNC-derived κ_{org} in the CCN closure, a result similar to that from HTDMA-derived κ_{org} in Figure 3.14 is obtained. The predicted N_{CCN}/N_{CN} was largely underestimated if κ_{org} is assumed to be zero (mean relative differences: −61% to −36%). If size-averaged (or size-resolved) κ_{org} from the regression method is used, the predicted N_{CCN}/N_{CN} agree to the measured with the mean relative differences from −5% to +2% (or −10% to −2%). If size-averaged (or size-resolved) κ_{org} from the ZSR method is used, the predicted N_{CCN}/N_{CN} agree to the measured with the mean relative differences from +7% to +25% (or +10% to +21%).

The result suggests that organics contributed to the CCN activation, as in the case of the results from the HTDMA-derived κ_{org}.

4. Hygroscopicity and CCN activity of forest aerosol particles in Walayama

4.1. Overview of number-size distribution and chemical composition of studied aerosol particles

The number-size distributions and chemical composition of the studied aerosols, and results from backward air mass trajectories were described in *Han et al.* [2013, 2014] and are briefly explained here. On the first six days (0600, August 20–0600, August 26, Japan Standard Time (JST)), air masses were originated from the Asian continent and urban areas in Japan and the observation site was influenced by the inflow of aged aerosols. The total number concentrations of aerosols were smaller and the number-size distributions had larger mode diameters (around 100 nm) as compared to those in the latter periods. The number concentrations and the fitted mode diameters did not exhibit significant changes a day. By contrast, on the latter four days (0600, August 26–0600, August 30 JST), clean maritime air masses originated from the Pacific Ocean arrived at the observation site. The total number concentrations were larger and the number-size distributions had smaller mode diameters. Bursts of small particles ($d_{p,dry}$~30 nm) in the morning and their rapid growth in the afternoon indicate new particle formation (NPF) and their growth. In the daytime, the fraction of semi-volatile oxigenated organic aerosol (SV-OOA) increased in accordance with the increase of air temperature and solar radiation, suggesting locally photochemical formation of BSOA. From the afternoon to nighttime (1300–2300 JST), the O/C ratio of organics and the fraction of the signal at m/z 44 among those from organic aerosol compounds (f_{44}) increased, indicating the oxidation and aging of fleshly formed BSOA. In the former period (non-NPF event days), ammonium sulfate and low-volatile OOA (LV-OOA) were abundant. In the latter period (NPF event days), organics and SV-OOA component

(a surrogate of locally-formed BSOA) were abundant and the mass concentrations and fractions of BSOA in the range of d_{va}<300 nm (~$d_{p,dry}$: 60–150 nm) increased whereas ammonium sulfate did not. The results suggests that aged particles composed of LV-OOA and ammonium sulfate were dominant during non-event days and that locally emitted particles composed of SV-OOA and BSOA were dominant during NPF event days, in association with new particle formation and the subsequent growth.

4.2. Size-resloved hygroscopic growth factors distributions

The averages of *g* distributions and those normalized for four different time sections are presented in Figure 4.1. Here, results in the sections when particle hygroscopicity tended to be low (0900–2100 JST) and high (2100–0900 JST) on both NPF-event and non-event days are presented. The mean ± standard deviation (SD) of *g* is summarized in Table 4.1. The size-resolved *g* distributions of particles ($d_{p,dry}$: 24.1–359 nm, $0.8 \leq g \leq 2.2$) at 85% RH showed differences depending on non-event/NPF-event days and the time sections defined above.

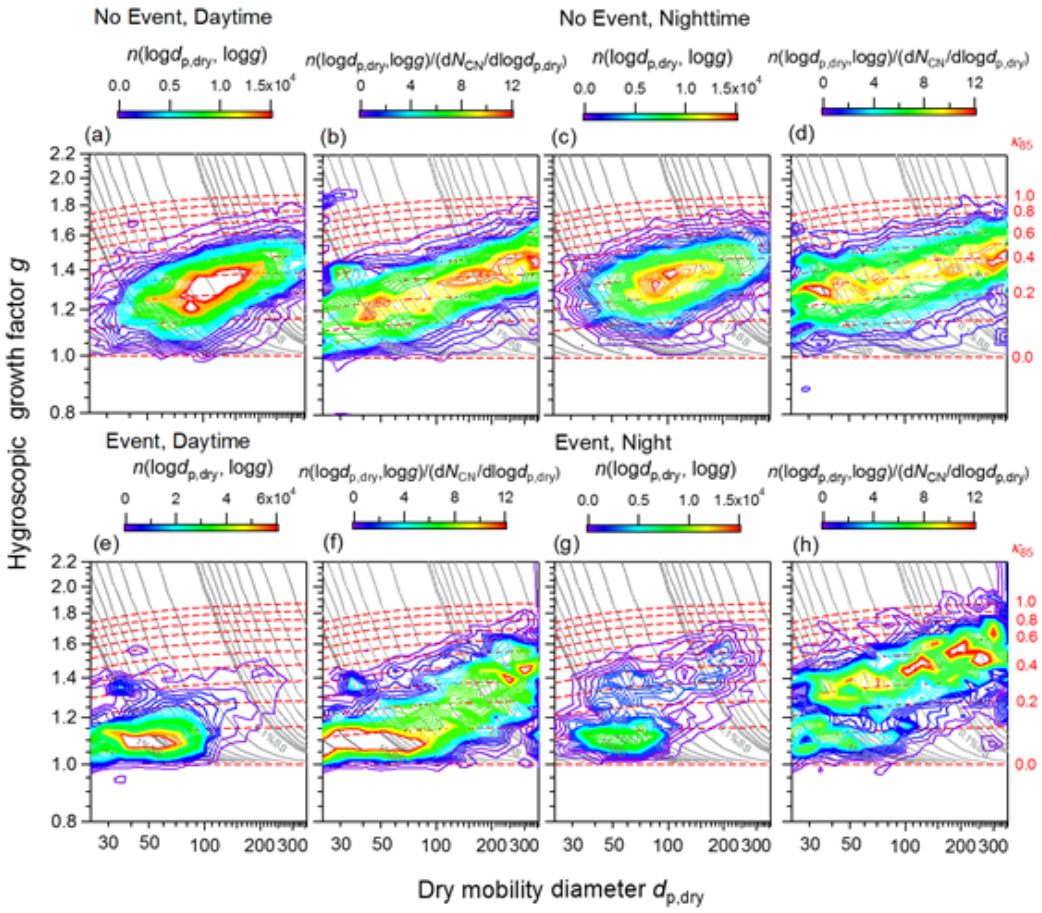

Figure 4.1. (a–b) The average of (a) two-dimensional distributions of the number concentrations of aerosol particles as a function of hygroscopic growth factor (g) and dry mobility diameter ($d_{p,dry}$) at 85% RH and (b) that normalized by N_{CN} during 0900-2100 JST on non-event days. (c–d) Same as (a–b), but during 2100-0900 on non-event days. (e–f) Same as (a–b), but during 0900-2100 JST on NPF event days. (g–h) Same as (a–b), but during 2100-0900 on NPF event days. The dashed red lines represent contours of κ at 85% RH (κ_{85}). The gray contours show critical SS estimated from the κ-Köhler theory [*Mochida et al.*, 2011].

On non-event days (Figures 4.1a–d), broad unimodal g distributions ranging of 1.2–1.4 were observed and the differences of the g distributions in the time sections were not clear. The averages of the normalized g distributions for every 3h were also similar throughout the day (Figure 4.2). During 0900-2100 JST, the mean g of particles

in the Aitken ($d_{p,dry}$<100 nm) (g_{Ait}) and accumulation mode ranges (g_{Acc}) were 1.23 and 1.39, respectively. During 2100-0900 JST, the mean *g* of particles in the Aitken ($d_{p,dry}$<100 nm) (g_{Ait}) and accumulation mode ranges (g_{Acc}) were 1.30 and 1.43, respectively. The mean *g* observed during 0900-2100 JST was slightly lower, indicating that the locally-formed BSOA with less hygroscopicity decrease the hygroscopicity of particles, although more hygroscopic particles were dominant.

On NPF event days (Figures 4.1e–h), the two-demensional *g* distributions in the two time sections were largely different. During 0900-2100 JST, large number concentrations of less hygroscopicity particles with *g* of 1.1–1.2 appeared in the Aitken mode range. This low *g* values were similar to the those of laboratory-generated BSOA (*g*~1.1) [*Varutbangkul et al.,* 2006; *Lang-Yona et al.,* 2010]. The result suggests that the particles were composed of newly-formed BSOA. This suggestion is supported by the results from chemical composition analysis using the AMS that the fraction of SV-OOA estimated from positive matrix factorization analysis as well as that of organics was large and that SV-OOA were regarded to be generated locally. Further, the *g* values in the accuulation mode range as well as those in the Aitken mode range (g_{Ait}: 1.15 and g_{Acc}: 1.23) were also low, as compared to those on non-event days (g_{Ait}: 1.23 and g_{Acc}: 1.39). This is presumably because the condensation of less hygroscopic BSOA components lead to the decrease of *g* of pre-existing large particles in the accumulation mode range. By contrast, during 2100-0900 JST (Figures 4.3e–4.3h), the distributions shifted and constituted a more hygroscopic mode and the mean *g* were high both in the Aitken and accumulation mode ranges (g_{Ait}: 1.29 and g_{Acc}: 1.50).

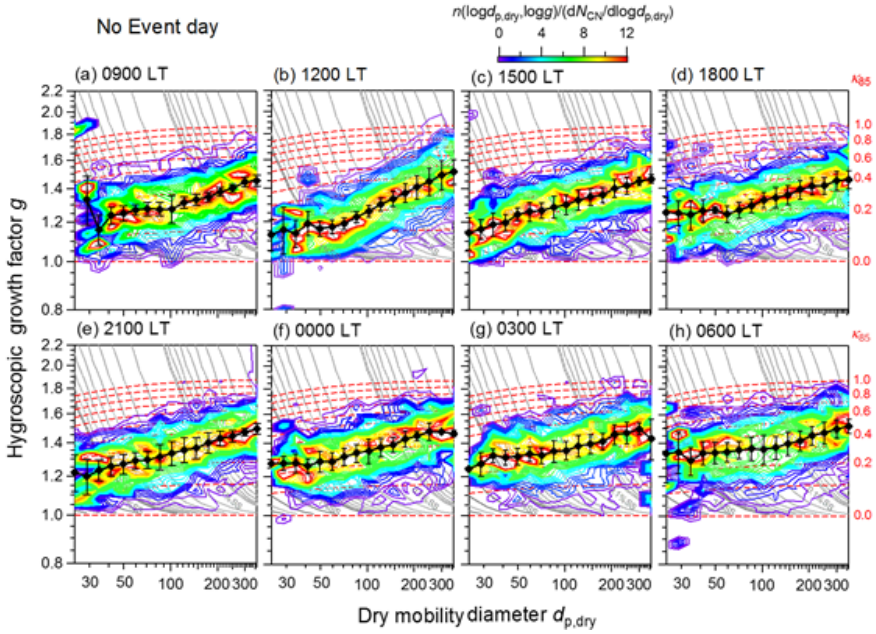

Figure 4.2. The averages of the normalized *g* distributions at 85% RH during (a) 0900–1200 (b) 1200–1500 (c) 1500–1800 (d) 1800–2100 (e) 2100–2400 (f) 0000–0300 (g) 0300–0600 (h) 0600–0900 JST, on non-event day.

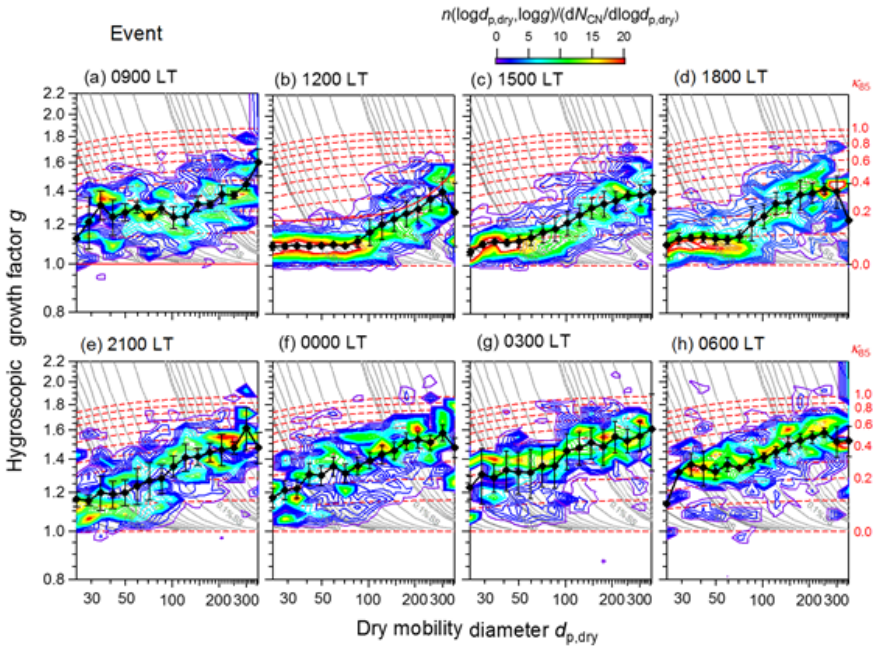

Figure 4.3. Same as Fig.4.1.2, but on NPF event days.

Table 4.1. Hygroscopic growth factors of aerosol particles and hygroscopicity parameters of aerosol particles and organics[a].

period	$d_{p,dry}$	g_m[b]	κ_{HTDMA}[c]	κ_{org}	period	$d_{p,dry}$	g_m[b]	κ_{HTDMA}[c]	κ_{org}
NE_day	28.9	1.23 ± 0.12	0.22 ± 0.15		NPF_day	28.9	1.12 ± 0.06	0.11 ± 0.07	
	49.6	1.23 ± 0.05	0.20±0.05			49.6	1.14 ± 0.07	0.12 ± 0.07	
	102	1.29 ± 0.06	0.23±0.06			102	1.21 ± 0.07	0.16 ± 0.06	
	209	1.40 ± 0.05	0.33±0.06			209	1.35 ± 0.07	0.28 ± 0.07	
	359	1.47 ± 0.06	0.40±0.07			359	1.36 ± 0.19	0.30 ± 0.19	
	aver	1.30 ± 0.10	0.26±0.07			aver	1.23 ± 0.10	0.19 ± 0.08	
	Ait	1.23 ± 0.04	0.20±0.02	0.20 ± 0.05		Ait	1.15 ± 0.04	0.12 ± 0.02	0.17 ± 0.06
	Acc	1.39 ± 0.06	0.33±0.06	0.30 ± 0.08		Acc	1.34 ± 0.05	0.27 ± 0.05	0.25 ± 0.06
NE_night	28.9	1.27 ± 0.10	0.28±0.13		NPF_night	28.9	1.22 ± 0.11	0.23 ± 0.02	
	49.6	1.30 ± 0.06	0.27±0.07			49.6	1.28 ± 0.10	0.26 ± 0.05	
	102	1.34 ± 0.07	0.29±0.08			102	1.40 ± 0.09	0.35 ± 0.06	
	209	1.44 ± 0.05	0.38±0.06			209	1.52 ± 0.08	0.47 ± 0.06	
	359	1.47 ± 0.08	0.40±0.08			359	1.52 ± 0.18	0.49 ± 0.07	
	aver	1.36 ± 0.07	0.32±0.05			aver	1.38 ± 0.12	0.35 ± 0.11	
	Ait	1.30 ± 0.03	0.28±0.01	0.26 ± 0.07		Ait	1.29 ± 0.06	0.27 ± 0.05	0.30 ± 0.10
	Acc	1.43 ± 0.04	0.37±0.04	0.30 ± 0.07		Acc	1.50 ± 0.04	0.46 ± 0.05	0.37 ± 0.16
all	28.9	1.22 ± 0.11	0.22±0.03						
	49.6	1.24 ± 0.09	0.22±0.01						
	102	1.31 ± 0.09	0.26±0.02						
	209	1.42 ± 0.08	0.36±0.06						
	359	1.46 ± 0.12	0.40±0.02						
	aver	1.32 ± 0.10	0.29±0.07						
	Ait	1.25 ± 0.04	0.23±0.01	0.23 ± 0.09					
	Acc	1.42 ± 0.05	0.35±0.05	0.31 ± 0.08					

[a] Mean ± SD.

[b] Mean hygroscopic growth factors in the range of $0.8 \leq g \leq 2.2$.

[c] Volume-weighted hygroscopicity parameter from g_m.

Time series of g distributions of aerosol particles at 50, 100, 200, and 300 nm of $d_{p,dry}$ and the mean g in each diameter (g_m) are presented in Figure 4.4. The temporal variation pattern of g distributions were similar regardless of the particle diameter (50, 100, 200, and 359 nm), while g_m tended to be larger as the particle sizes were larger. The diurnal variations on non-event days were small, as seen as Figures 4.1 and 4.2. On the other hand, strong diurnal variations were observed on NPF event days. The g_m was

low in the morning and the afternoon and changed to high in the evening and the nighttime regardless of the particle size. Growth of newly-formed particles with less hygroscopicity and the condensation of BSOA components to pre-existing particles at large diameters may be causes of the variations of g of small and large particles, respectively.

In the evening and the nighttime, the g_m increased and more hygroscopic particles appeared over a wide diameter range. Possible reasons include the oxidation and aging of newly-formed BSOA, the production of water-soluble organic matter (WSOM) in the aqueous phase, and the influence of the inflow of sulfate originating from the maritime air mass. The aging process in the atmosphere probably lead to the increase of hygroscopicity of particles both in newly-formed and pre-existing particles. In fact, the mass concentrations of organics at ~300 nm of d_{va} (corresponding to ~150 nm of $d_{p,dry}$) increased without the increase of sulfate on NPF event days, and the oxidation and aging of newly formed BSOA from afternoon to midnight was suggested in *Han et al.* [2014]. The production of WSOC by the oxidation of BVOC may also contribute to the increase of particle hygroscopicity. *Miyazaki et al*. [2012a, 2012b] reported that the concentrations of WSOC in a deciduous forest in Japan increased on NPF event days and they suggest that the oxidation of BVOC (pinene and isoprene) contributed largely (~90%) to the enhancement of WSOC, in the daytime with the increase of air temperature and solar radiation, and in the nighttime with the production of WSOC in the aqueous phase at higher RH. *Engelhart et al.* [2008, 2012] reported that BSOA after photochemical aging may partly work as WSOC from laboratory study. Furthermore, high g (up to 1.8) at >300 nm was observed in the nighttime on NPF event days (Figure 4.4). In this period, the mass fraction of sulfate increased at a larger diameter (d_{va} >300

nm), which probably lead to the increase in *g*. The sulfate may have been originated from the Pacific Ocean facing the studied site, because observed *g* was higher than that of pure ammonium sulfate particles (*g*~1.6 at 85% RH) and was close to the values in maritime environments.

The hygroscopic growth of particles were characterized by broad and unimodal *g* distributions. The broad and unimodal *g* distributions were also reported at some forest sites [*Hong et al., 2014*], whereas multi-modal distributions were also reported at other forest sites [*Hämeri et al.,* 2001; *Irwin et al.,* 2011]. The absence of less hygroscopic modes in this study suggests that the contribution of locally-emitted anthropogenic primary particles, such as particles composed of hydrocarbon-like organic aerosol (HOA) and black carbon (BC), was small. The unimodal *g* distributions during the studied periods can be explained as follows. On non-NPF event days, the observation site was influenced by air masses with long-range transport and aged particles (ammonium sulfate and LV-OOA) were dominant. The aged, well-mixed, and highly oxidized particles that were relatively more hygroscopic (g~1.2–1.4) were abundant over the day and they formed broad and unimodal *g* distributions. This is consistent with the fact that size-resolved *g* were mainly characterized by unimodal distributions with a large mass fraction of ammoniated sulfate (72%) and with high hygroscopicity (median g: 1.39–1.47 at 49–125 nm) at a remote receptor site of the Asian outflow (Okinawa) [*Mochida et al*., 2010]. In this study, lower hygroscopicity (mean g: 1.2–1.4) than those in Okinawa were observed, which is probably explained by the larger fraction of organics with less hygroscopicity rather than inorganic salts.

On NPF event days, the study site was under the influence of maritime air masses in which aerosol number and mass concentrations was presumably low. This

might lead to enhanced contributions of the newly-formed BSOA to the particle hygroscopicity. In the daytime, the bursts of nanoparticles and the formation of BSOA probably lead to the predominance of fresh, less oxidized, and less hygroscopic particles (g~1.1) and they influenced on the particle hygroscopicity in both the Aitken and accumulation mode ranges. Then, g distributions with less hygroscopic particles appeared over a wide diameter range.

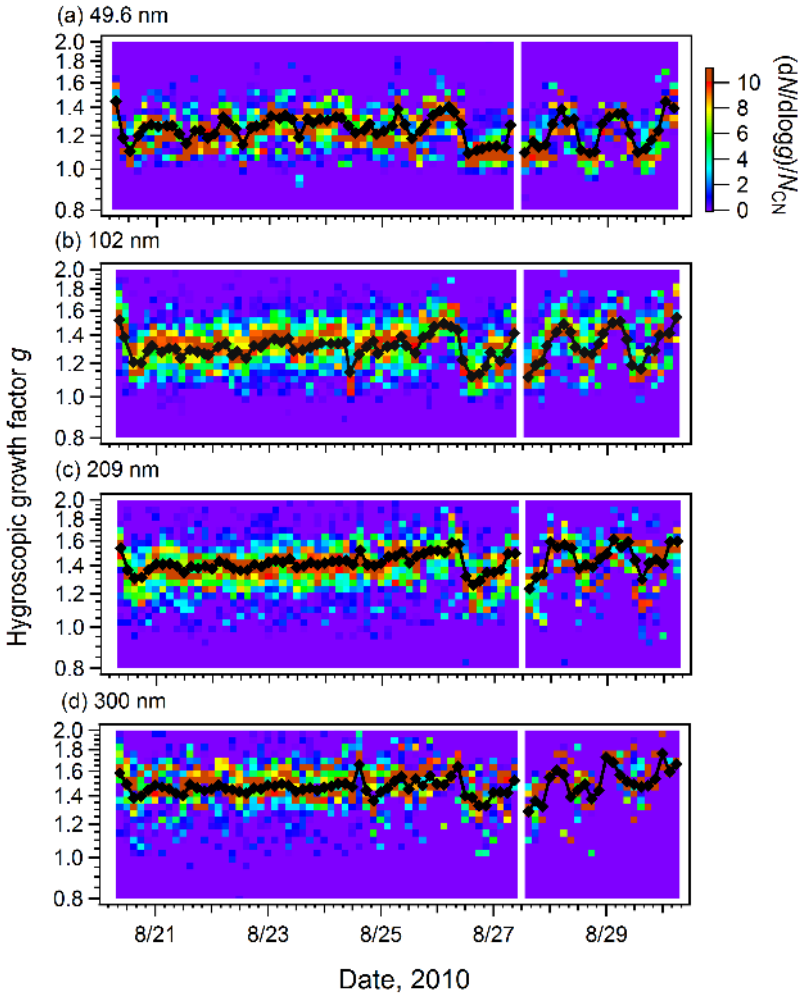

Figure 4.4. Time series of g distributions at 85% RH for particles with $d_{p,dry}$ of (a) 49.6 nm, (b) 102 nm, (c) 209 nm, and (d) 300 nm. The symbols represent mean g in the range of $0.8 \leq g \leq 2.2$.

The number-size distributions and the number fractions of particles in different ranges of g were calculated to investigate the size dependence of particle hygroscopicity (Figure 4.5). The averages of the number-size distributions and the number fractions were characterized by the large fraction of more hygroscopic particles (g>1.25) except for 0900-2100 JST on NPF event days, being in contrast to those at an urban site [*Kawana et al.,* 2014], which were characterized by the large N_{CN} and the large fraction of less hygroscopic particles (g<1.25). During 0900-2100 JST on non-event days (Figures 4.5a and 4.5b), intermediate hygroscopic particles ($1.1 \leq g < 1.4$) were dominant and the number concentrations of highest more hygroscopic particles ($g \geq 1.4$) in the large diameter were large. During 2100-0900 JST on non-event days (Figures 4.5c and 4.5d), whereas the shape of averaged number-size distributions was not different from that during 0900-2100 largely, the number concentration of less hygroscopic particles was on average to a half of the value during 0900-2100 JST, and the fraction of more hygroscopic particles was relatively large.

During 0900-2100 JST on NPF event days (Figures 4.5e and 4.5f), the large N_{CN} and the large fraction of less hygroscopic particles were observed, in particular in the Aitken mode range. The fraction of more hygroscopic particles in this time section was lower than those in the other time sections. The less hygroscopic particles were dominant (>50%) up to 180 nm, suggesting that newly-formed less hygroscopic particles were present in the Aitken mode range (Figures 4.1 and 4.3) and the less hygroscopic components also affected the decrease of the particle hygroscopicity of pre-existing larger particles by the condensation in the accumulation mode range. During 2100-0900 JST on NPF event days (Figures 4.5g and 4.5h), lowest N_{CN} and largest

fraction of more hygroscopic particles among four different time sections were observed. The large fraction of more hygroscopic particles might be caused by the chemical aging of newly-formed BSOA and the production of WSOC. At >300 nm, the inflow of maritime airs may have also contributed to the increase of particle hygroscopicity as mentioned above.

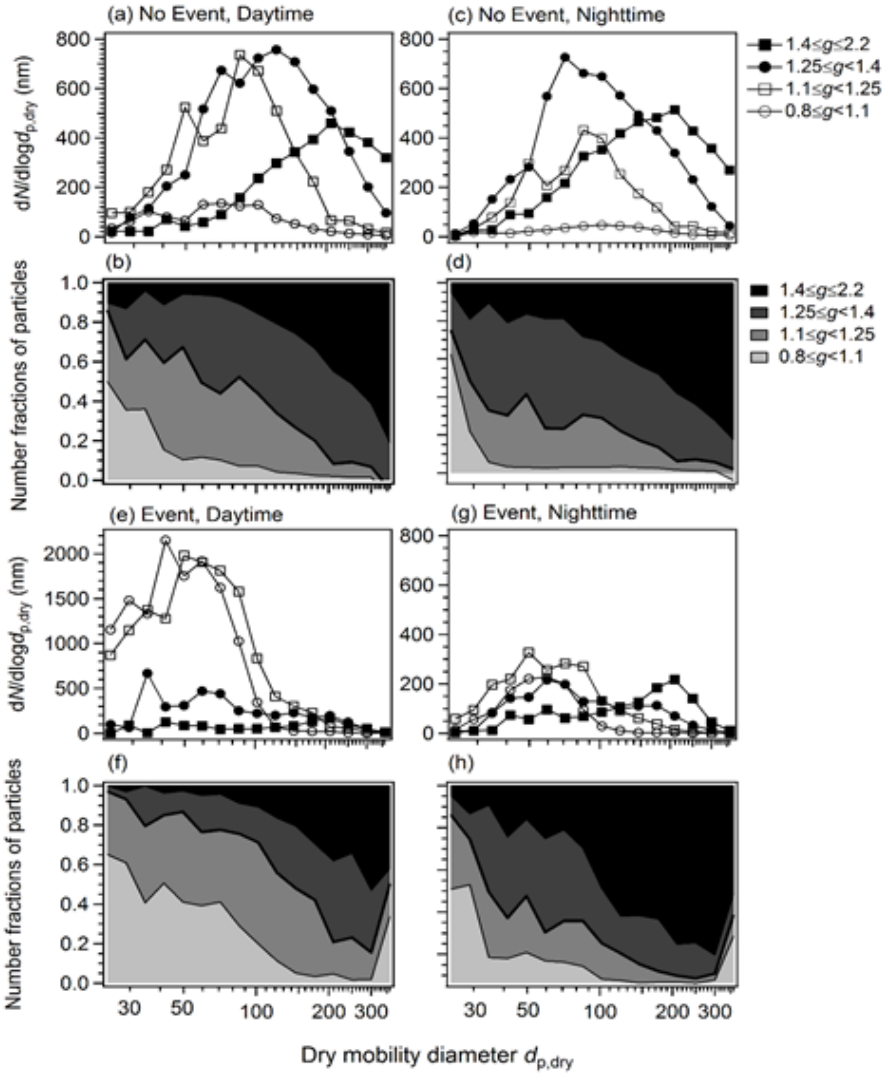

Figure 4.5. (a–b) The averages of (a) the number-size distributions and (b) the number fractions of aerosol particles in the ranges of $0.8 \leq g < 1.1$, $1.1 \leq g < 1.25$, $1.25 \leq g < 1.4$, and $1.4 \leq g \leq 2.2$ during 0900-2100 JST on non-event days. (c–d) Same as (a–b), but during 2100-0900 JST on non-event days. (e–f) Same as (a–b), but during 0900-2100 JST on NPF event days. (g–h) Same as (a–b), but during 2100-0900 JST on NPF event days.

4.3. CCN activity

The time series of the CCN activated fraction (F_{act}) and the CCN activation diameter (d_{act}) at 0.12%, 0.23%, and 0.41% SS, both of which were derived from the curve fitting to the CCN efficiency spectra, are presented in Figures 4.6a–4.6c. The F_{act} and d_{act}, and the CCN activated fraction at a maximum diameter of 359 nm (F_{max}) were summarized in Table 4.2. The mean ± SD of F_{act} and F_{max} were on average more than 0.9 except during 0900-2100 JST on NPF event days, indicating that that fractions of CCN-inactive particles well above d_{act} were generally small. During 0900-2100 JST on NPF event days, the mean ± SD of F_{act} and F_{max} were smaller and the fraction of CCN-inactive particles were larger than those in other time sections regardless of SS conditions.

While the diurnal variations of d_{act} were small on non-event days, those on NPF event days were large under all SSs (0.12%–0.41% SS); the d_{act} during 0900-2100 JST were large and those during 2100-0900 JST were small (Figures 4.6a–4.6c). The mean ± SD of d_{act} during 0900-2100 JST were 171 ± 12, 118 ± 19, and 84 ± 8 nm at 0.12%, 0.23%, and 0.41% SS, respectively, and those during 2100-0900 JST were 138 ± 11, 89 ± 10, and 65 ± 14 nm, respectively. The difference of d_{act} in the time sections was greater than that on non-event days; the d_{act} were 152±11, 98±9, and 69±7 nm at 0.12%, 0.24%, and 0.43% SS, respectively. The averages of the CCN efficiency spectra and the fitted curves also suggest the differences between NPF-event and non-event days and between 0900-2100 and 2100-0900 JST (Figures 4.7a–4.7c). The result is explained by the differences of hygroscopicity distributions in the four time sections. During 0900-2100 JST on NPF event days, less hygroscopic small particles, which should have large

S_{crit} for activation, were dominant, which is in line with the increase of d_{act} and small F_{act}. During 2100-0900 JST, more hygroscopic large particles were dominant, being in line with the decrease of d_{act} and large F_{act}.

The time series of N_{CN}, N_{CCN}, and the ratio of N_{CCN} to N_{CN} (N_{CCN}/N_{CN}) under three SS conditions are shown in Figures 4.6d and 4.6e. On NPF event days, the N_{CCN} and N_{CCN}/N_{CN} increased from the afternoon in the response to the burst of N_{CN} and the increase of particle hygroscopicity (Figure 4.4), indicating that newly-formed particles after aging contributed to N_{CCN}. The mean ± SD of N_{CCN} and N_{CCN}/N_{CN} were summarized in Table 4.2. The mean ± SD of N_{CCN} during 0900-2100 JST were 63 ± 27, 117 ± 49, and 155 ± 108 cm^{-3} at 0.12%, 0.23%, and 0.41% SS, respectively, and those during 2100-0900 JST were 95 ± 64, 202 ± 153, and 360 ± 313 cm^{-3}, respectively. The mean ± SD of N_{CCN}/N_{CN} during 0900-2100 JST were 0.05% ± 0.03%, 0.21% ± 0.19%, and 0.21% ± 0.05% at 0.12%, 0.23%, and 0.41% SS, respectively, and those during 2100-0900 JST were 0.21% ± 0.12%, 0.28% ± 0.14%, and 0.51% ± 0.14%, respectively. On non-event days, the mean ± SD of N_{CCN} at 0.12%, 0.23%, and 0.41% were 297 ± 124, 543 ± 166, and 674 ± 275 cm^{-3}, respectively. The mean ± SD of N_{CCN}/N_{CN} at 0.12%, 0.23%, and 0.41% were 0.29 ± 0.06, 0.49 ± 0.08, and 0.60 ± 0.11, respectively. The mean N_{CCN} in this study was similar to those over forests from previous studies (61–274 cm^{-3} at 0.11%–0.37% SS, [*Irwin et al.,* 2011]; <500 cm^{-3} at 0.14%–0.36% SS, [*Levin et al.,* 2012]) and higher than the mean N_{CCN} value in pristine rainforest in Amazonia (35–160 cm^{-3} at 0.1%–0.8% SS, [*Gunthe et al.,* 2009]).

The mean values of N_{CCN} and N_{CCN}/N_{CN} on NPF event days were lower than those on non-event days, in spite that the particle bursts resulted in large N_{CN} in the daytime and more hygroscopic and large particles were dominant during NPF event

days. One possible reason of smaller values is the wet removal of N_{CCN} and N_{CN} by precipitation in the afternoon [*Han et al.,* 2013]. As seen in Figures 4.5g and 4.5h, lowest N_{CN} was observed during 2100-0900 JST. The N_{CCN} should have been limited in this period because of the small number concentrations of particles, although more hygroscopic particles were dominant and most of particles activated as CCN.

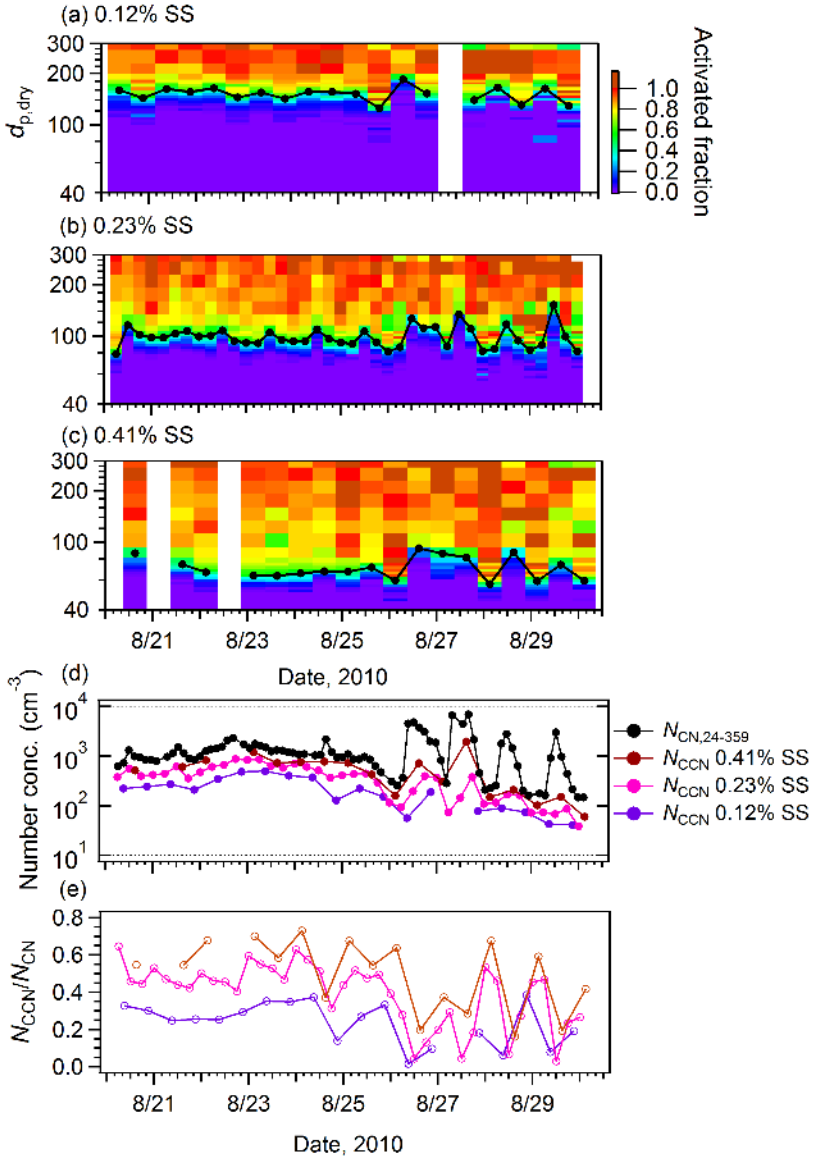

Figure 4.6. (a–c) Time series of size-resolved CCN activated fractions at $d_{p,dry}$ under 0.12%, 0.23%, and 0.41% SS. (d) Time series of the number concentrations of CCN and CN in the size range of 24–359 nm (N_{CCN} and N_{CN}). (e) Time series of the ratios of N_{CCN} to N_{CN} under 0.12%, 0.23%, and 0.41% SS. The filled circles with solid lines in figures a–c represent CCN activation diameters.

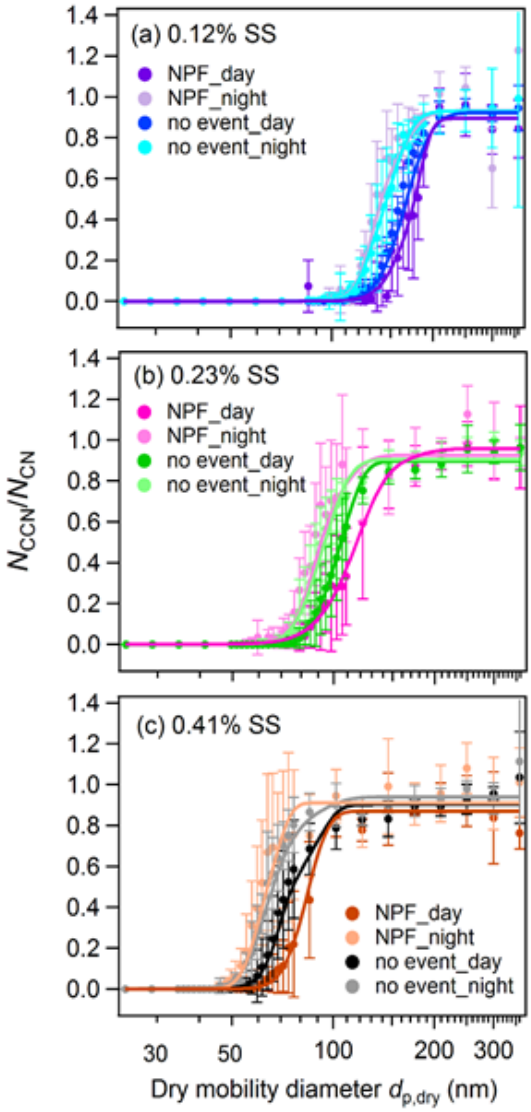

Figure 4.7. The averages of the measured CCN efficiency spectra and the curves fitted to them under (a) 0.12%, (b) 0.23%, and (c) 0.41% SS. The bars represent the standard deviation.

Table 4.2. Values from CCN activation measurement in different periods[a].

period	SS	F_{act}	F_{max}	d_{act}	κ_{CCNC}[b]	κ_{org}[c]
NE_day						
	0.41	0.89 ± 0.06	1.04 ± 0.22	73 ± 9	0.22 ± 0.02	
	0.23	0.90 ± 0.04	0.96 ± 0.11	103 ± 7	0.24 ± 0.05	
	0.12	0.92 ± 0.03	0.94 ± 0.11	159 ± 4	0.22 ± 0.02	
						0.22 ± 0.07
NE_night						
	0.41	0.93 ± 0.06	1.11 ± 0.30	65 ± 9	0.29 ± 0.08	
	0.23	0.91 ± 0.04	0.94 ± 0.06	92 ± 7	0.33 ± 0.08	
	0.12	0.93 ± 0.05	0.99 ± 0.10	145 ± 12	0.34 ± 0.12	
						0.34 ± 0.08
NPF_day						
	0.41	0.88 ± 0.05	0.86 ± 0.17	84 ± 8	0.17 ± 0.03	
	0.23	0.96 ± 0.07	0.97 ± 0.20	118 ± 19	0.17 ± 0.08	
	0.12	0.89 ± 0.07	0.85 ± 0.14	171 ± 12	0.14 ± 0.04	
						0.13 ± 0.06
NPF_night						
	0.41	0.93 ± 0.07	1.01 ± 0.17	65 ± 14	0.33 ± 0.07	
	0.23	0.95 ± 0.07	0.94 ± 0.08	89 ± 10	0.39 ± 0.10	
	0.12	0.92 ± 0.07	1.20 ± 0.50	138 ± 11	0.33 ± 0.14	
						0.41 ± 0.04
all						
	0.41	0.91 ± 0.06	1.02 ± 0.24	71 ± 11	0.26 ± 0.08	
	0.23	0.91 ± 0.06	0.95 ± 0.12	100 ± 15	0.28 ± 0.10	
	0.12	0.92 ± 0.03	1.00 ± 0.25	152 ± 5	0.25 ± 0.10	

[a]Mean ± SD.

[b]Hygroscopicity parameter calculated from d_{act}.

[c]Calculated for particles in the Aitken mode range.

4.4. The hygroscopicity parameter κ of forest aerosols and the organic aerosol component

The hygroscopicity parameter κ calculated from the g distribution (κ_{HTDMA}) and from the CCN activation diameter (κ_{CCNC}) are summarized in Table 4.1 and 4.2, and are compared with κ values from previous studies in Table 4.3. In the comparison of κ_{HTDMA} and κ_{CCNC}, similar ranges of $d_{p,dry}$ were applied (0.12% SS: 136–169 nm and 152 ± 5 nm, 0.23% SS: 88–109 nm and 100 ± 15 nm, 0.41% SS: 64–85 nm and 71 ± 11 nm, for κ_{HTDMA} and κ_{CCNC}). The mean ± SD of both κ_{HTDMA} and κ_{CCNC} is characterized by the differences between NPF event and non-event days and between 0900–2100 and 2100–0900 JST, and the difference in particle size. On NPF event days, the mean values of κ_{HTDMA} and κ_{CCNC} were ~30% lower during 0900-2100 JST and ~15% higher during 2100-0900 JST, than those in the same time sections on non-event days. During 0900-2100 JST on NPF event days, the mean ± SD of κ_{HTDMA} in the Aitken and accumulation mode ranges were 0.12 ± 0.02 and 0.27 ± 0.05, respectively. During 2100-0900 JST on NPF event days, those were 0.27 ± 0.05 and 0.46 ± 0.05, respectively. In the case of κ_{CCNC}, the mean ± SD in 69–152 nm were 0.16± 0.02 and 0.35 ± 0.05 during 0900-2100 and 2100-0900 JST, respectively. The mean ± SD of κ_{HTDMA} and κ_{CCNC} in this study were similar to those from previous studies (Table 4.3). However, κ_{HTDMA} in the accumulation mode range during 2100-0900 JST on NPF event days (0.46 ± 0.05) was higher than previously reported κ values from HTDMA and CCNC data analysis.

The κ of organics (κ_{org}) was calculated from the volume fractions of chemical components and total particle hygroscopicity on the assumption of the ZSR mixing rule [*Petters and Kreidenweis,* 2007]. The particles were assumed to be composed of organics and ammonium sulfate, based on the observed chemical composition. The

differences of κ_{org} in the Aitken mode particles ($d_{p,dry:}$ 60–102 nm, N: 80) and the accumulation mode particles ($d_{p,dry:}$ 150–359 nm, N: 80), and the differences of κ_{org} in four different time sections (0900–2100 and 2100–0900 JST on non-event and NPF-event days) were investigated. In the calculation of size-resolved κ_{org}, d_{va} in the AMS data were converted to $d_{p,dry}$ used for the HTDMA and CCNC data, based on the equation for the conversion described in *Decalro et al.* [2004], under the assumption that particles were spheres and the densities of the particle's components ranged of 1.0–1.5 g cm^{-3}. The composition of particles in the ranges of 60−150 nm and 150−540 nm in d_{va} were used for particles with $d_{p,dry}$ of 60−102 nm (Aitken mode particles) and 150−359 nm. The κ_{org} was calculated by subtracting the contribution of ammonium sulfate to κ_{HTDMA} or κ_{CCNC} (see chapter 3) . The κ_{AS} values were calculated to be 0.493 and 0.59–0.64 for sub- and super-saturated conditions, respectively, by applying the Pitzer equation to the κ-Köhler model.

The κ_{org} values in the Aitken and accumulation mode ranges in four different time sections are presented in Figure 4.8, and the mean ± SD of κ_{org} are summarized in Tables 4.1 and 4.2. During 0900-2100 JST on NPF event days, the mean κ_{org} derived from κ_{HTDMA} was lower than those in other time sections in both Aitken and accumulation mode ranges (Figures 4.8a and 4.8b). The mean ± SD of κ_{org} in the Aitken and accumulation mode ranges were 0.13 ± 0.06 and 0.24 ± 0.06, respectively. By contrast, during 2100-0900 JST on NPF event days, κ_{org} was higher than those in other time sections. The mean ± SD of κ_{org} in the Aitken and accumulation mode ranges were 0.30 ± 0.10 and 0.33 ± 0.13, respectively. Higher SD during 2100-0900 JST of NPF event days may be due to the large uncertainty by small N_{CN}, g values, and chemical composition (the ratio of organics to sulfate: 1.81 ± 1.78) [*Han et al.,* 2014]. The result

suggests that the degrees of aging or influences of inflow of more hygroscopic particles may have varied during this periods and affected the result. The κ_{org} derived from κ_{CCNC} also showed a variation pattern similar to that derived from κ_{HTDMA} (Figure 4.8c and Table 4.2). The mean ± SD of κ_{HTDMA}, κ_{CCNC}, and κ_{org} in the Aitken mode range during 0900-2100 JST on NPF event days were 0.17 ± 0.02, 0.17 ± 0.04, and 0.13 ± 0.06, respectively. The κ obtained in this study were similar to those of forest aerosols reported in previous studies and laboratory-generated pure BSOA. The reported κ values of atmospheric forest aerosols characterized by the predominance of BSOA from HTDMA and CCNC were slightly hygroscopic, ranging of 0.1–0.2: ~0.15 in the tropical rainforest in Amazonia [*Gunthe et al.,* 2009], ~0.13 and ~0.18 in boreal forest [*Cerully et al.,* 2011; *Sihto et al.,* 2011], and ~0.1 and ~0.13 in other forested sites [*Dusek et al.,* 2010; *Levin et al.,* 2014]. Laboratory-generated BSOA have κ values of ~0.1 (0.15 from monoterpene and 0.12 from isoprene at 85% RH [*Engelhart et al.,* 2008, 2011]; 0.04–0.10 from monoterpene at 90% RH [*Lang-Yona et al.,* 2010]) and g of ~1.1 (1.06–1.10 from monoterpene and 1.01–1.04 from sesquiterpene at 85% RH [*Varutbangkul et al.,* 2006]; 1.13 from monoterpene at 90% RH [*Lang-Yona et al.,* 2010]).

Table 4.3. Summary of κ values from this study and previous studies.

κ_{HTDMA}	κ_{CCNC}	κ_{org}	References
–	0.12-0.20, 0.10-0.82% SS (50-200 nm)	0.09-0.11 (from κ_{CCNC})	Gunthe et al., 2009
–	0.2–0.45 (Figure), 0.33-0.74% SS (<100 nm)	0.1 (from κ_{CCNC})	Dusek et al., 2010, NPF
0.14–0.15, 90% RH (30-50 nm)	0.19–0.22, 0.1-1.8% SS (40-80 nm)	0.12-0.14 (from κ_{HTDMA} and κ_{CCNC})	Cerully et al., 2011
0.17–0.37, 90% RH (32-258 nm)	0.05–0.37, 0.11-0.73% SS (50-210 nm)	–	Irwin et al., 2011
0.18, 90% RH (35-110 nm)	0.05–0.37, 0.1-1.0% SS	–	Sihto et al., 2011
–	0.15–0.22, 0.14-0.97% SS	0.13 (from κ_{CCNC})	Levin et al., 2014
0.17±0.02, 85% RH (< 100 nm)	0.17±0.04, 0.41% SS (< 100 nm)	0.13±0.06 (from κ_{HTDMA} and κ_{CCNC})	This study, NPF event days
0.22–0.40, 85% RH (24-359 nm)	0.25–0.28, 0.12-0.41% SS (71-152 nm)		This study, all the period

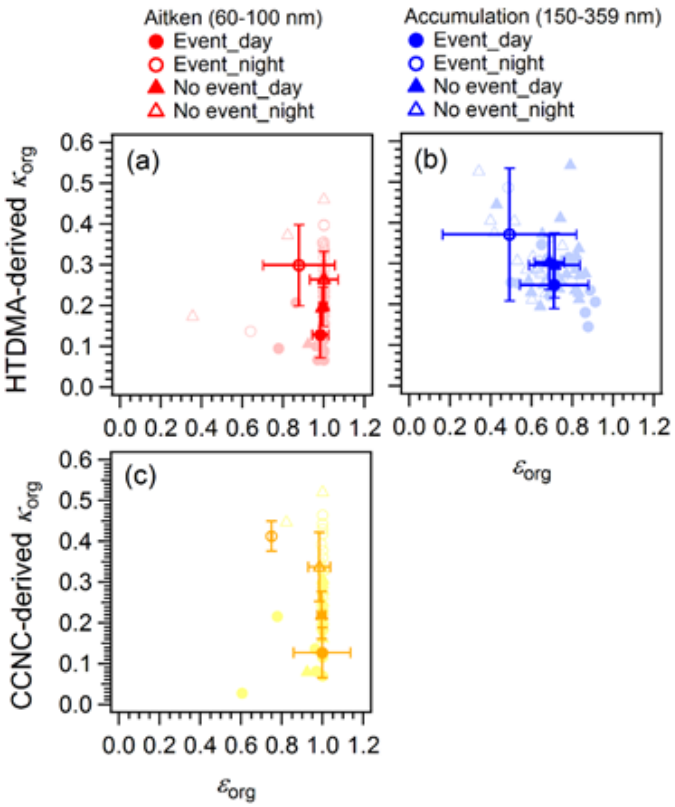

Figure 4.8. (a–b) The scatterplot of HTDMA-derived hygroscopicity parameter (κ_{HTDMA}) versus the volume fraction of organics (ε_{org}), for (a) Aitken and (b) accumulation mode ranges. (c) The scatterplot of CCNC-derived hygroscopicity parameter (κ_{CCNC}) versus ε_{org}. Symbols and bars in figures represent the mean and standard deviation of κ_{org}, respectively.

Regarding the difference of κ values under sub- and super-saturated conditions, κ_{HTDMA} and κ_{CCNC} values agreed well (~10% from the regression line, r>0.97) at presented in Figure 4.9 and Table 4.3. The difference of κ_{HTDMA} and κ_{CCNC} in this study was not so large as compared to those reported from some previous studies for forest aerosols [*Sihto et al.,* 2011; *Cerully et al.,* 2011]. The large difference between κ_{HTDMA} and κ_{CCNC} may possibly be caused by the failure to predict N_{CCN}. *Irwin et al.* [2013] reported that the differences of κ_{HTDMA} and κ_{CCNC} (κ_{HTDMA}: 0.17–0.37, κ_{CCNC}: 0.05–0.37)

in the tropical forest aerosols in Asia may lead to the overestimation of N_{CCN} in the CCN closure. Possible reasons for the large differences (>30%) of κ_{HTDMA} and κ_{CCNC} from laboratory and ambient aerosol studies were the presence of sparingly soluble materials, insufficient expression of dependence of the activity coefficient of water on the concentration of solution, and co-condensation process of semi-volatile compounds [*Prenni et al.,* 2007; *Wex et al.,* 2009; *Good et al.,* 2010; *Massoli et al.,* 2010; *Irwin et al.,* 2011; *Dusek et al.,* 2011; *Kristensen et al.,* 2012; *Wu et al.,* 2013].

The agreement of κ_{HTDMA} and κ_{CCNC} in this study suggests that the contribution of the above-mentioned effects was small. This may relates to the small contribution of organics with less hygroscopicity. The less hygroscopic organic compounds might lead to the larger difference of particle hygroscopicity under sub- and super-saturated conditions than that of inorganics. Some studies reported that organic compounds such as humic like substance (HULIS) in the atmosphere lead to the surface tension reduction significantly [*Facchini et al.,* 1999, 2000; *Kiss et al.,* 2005; *Diner et al.,* 2005]. Further, less hygroscopic organic compounds may lead to the increase of solute via the dissolution of sparingly soluble materials and dilution under higher RH and super-saturated conditions. In the case of urban aerosols with less hygroscopic particles, κ_{HTDMA} and κ_{CCNC} were different (~37%) and the large contribution of organics as mentioned above were possible (~28%) (see chapter 3). In this study, the fraction of more hygroscopic particles, such as inorganic salts and aged organic particles, were relatively high, as compared to that of the urban aerosols. Further, some studies showed that the contribution of surface tension reduction of BSOA was not large: the decrease was within 10% or the surface tension was same as that of pure water. Hence, the differences of κ_{HTDMA} and κ_{CCNC} may not be so large.

Table 4.4. Ratios of κ_{CCNC} to κ_{HTDMA} under 0.12, 0.23, and 0.41% SS[a].

SS	$\kappa_{CCNC}/\kappa_{HTDMA}$
0.12%	0.88 (0.97)
0.23%	1.05 (0.97)
0.41%	1.00 (0.97)

[a]Values without and with parentheses are the slopes of regression lines constrained through the origin, and the correlation coefficients between κ_{CCNC} and κ_{HTDMA}, respectively.

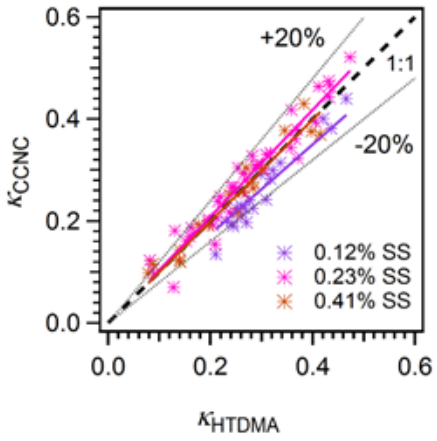

Figure 4.9. The scatterplot of κ_{HTDMA} versus κ_{CCNC} under 0.12%, 0.23%, and 0.41% SS. The solid lines represent the regression lines constrained through the origin.

4.5. CCN closure study

The N_{CCN}/N_{CN} values were predicted from the HTDMA data and were compared with the measured, to investigate the influence of particle hygroscopicity to CCN number concentrations. As presented in Figure 4.10a, the predicted N_{CCN}/N_{CN} agreed well to the measured if a single averaged g during observation was applied (12% ± 6%, r~0.91), although some deviations from 1:1 line were seen and the overestimation of

N_{CCN} was found at 0.41% SS (18%, r~0.85). Using four g values with the consideration of different characteristics in four time sections (Figures 4.10b and 4.10c), the degree of agreement is similar to that from a single g ((13% ± 4% (r~0.95) and 11% ± 3% (r~0.96), respectively). If size- and time-resolved g and size- and time-resolved g distribution were applied (Figures 4.10e and 4.10f), the correlation coefficients are higher and the degrees of overestimation improve slightly ((11% ± 4% (r~0.98) and 9% ± 3% (r~0.98), respectively), as compared to those using a single g.

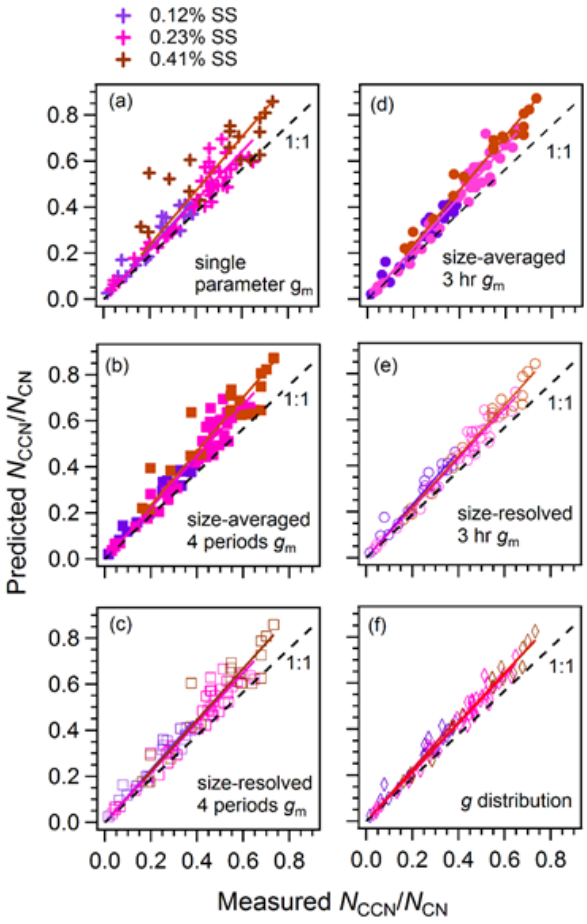

Figure 4.10. Predicted N_{CCN}/N_{CN} versus those measured, with the consideration of (a) single representative parameter g, (b) size-averaged g in four time sections, (c) size-resolved g in four time sections, (d) size-averaged g for every 3 h, (e) size-resolved g for every 3 h, and (f) size- and time-resolved g distributions. The solid lines represent the regression lines constrained through the origin.

Table 4.5. The ratios of predicted N_{CCN}/N_{CN} to those measured, with different considerations of particle hygroscopicity for the prediction[a].

SS	Single parameter g[b]	Size-average g[c]	Size-resolved g[d]	Size-average g[e]	Size-resolved g[f]	Size-resolved g distributions[g]
0.12%	1.10 (0.94)	1.11 (0.97)	1.14 (0.96)	1.10 (0.95)	1.16 (0.97)	1.12 (0.97)
0.23%	1.07 (0.95)	1.12 (0.96)	1.09 (0.97)	1.11 (0.98)	1.08 (0.98)	1.07 (0.99)
0.41%	1.18 (0.85)	1.17 (0.92)	1.11 (0.94)	1.18 (0.98)	1.10 (0.98)	1.08 (0.99)

[a] Values without and with parentheses are the slopes of regression lines constrained through the origin, and the correlation coefficients between predicted and measured, respectively.

[b]Using the single representative parameter g of 1.33.

[c]Using size-averaged g in four time sections: 1.30 (during 0900-2100 JST on non-event days), 1.36 (during 2100-0900 JST on non-event days), 1.23 (during 0900-2100 JST on NPF event days), and 1.38 (during 2100-0900 JST on NPF event days).

[d]Using size-resolved g in four time sections.

[e]Using size-averaged g for every 3 h.

[f]Using size-resolved g for every 3 h.

[g]Using size- and time resolved g distributions.

The result suggests that N_{CCN}/N_{CN} can be explained well using a representative g, without considering the variation of the detailed size- and time-resolved particle hygroscopicity. However, the larger overestimation was seen using a simplified g for smaller particles in the Aitken mode range, indicating that the difference of composition and hygroscopicity of particles in the Aitken and accumulation mode ranges needs to be considered, especially when less hygroscopic particles were dominant on NPF event days. The contribution of newly-formed particles to N_{CCN} were large (Figures 4.6d and 4.6e), and κ_{org} increased up to ~0.3 in the nighttime, suggesting that locally-generated BSOA after aging may have worked as WSOC and contributed to N_{CCN}. Additionally, long-range transported background aerosol particles composed of inorganic salts and

aged particles may have also contributed to N_{CCN} during the studied period.

The result is in contrast to that from an urban aerosol study in Nagoya [*Kawana et al.,* 2015, submitted to JGR], in which predicted N_{CCN}/N_{CN} agreed to the measured with the differences of −17% to +14% if an averaged g was used to represent the hygroscopicity of aerosols with less and more hygroscopicity modes. This result suggests that time- and size-resolved g was needed to the accurate prediction of N_{CCN}. Furthermore, κ_{HTDMA} and κ_{CCNC} were largely different on average (≥28%), suggesting that the effects of organics such as surface tension reduction and enhanced solute effects at higher RH contributed largely to the differences in the predicted and measured N_{CCN}/N_{CN}. In the case of the studied forest aerosols, the successful closure using an averaged g was expected from the characteristics of g distributions that they were unimodal.

The result in this study provides evidence of BSOA formation in the Aitken mode range. Further, clear diurnal patterns the hygroscopic growth of newly-formed particle was observed, based on the g distributions from 24 to 359 nm, which shows the contribution of newly-formed particles to CCN number concentrations for the first time in the Asian region. The results were useful to understand the hygroscopicity and CCN activity of forest aerosols and newly-formed BSOA, and to obtain HTDMA- and CCNC-derived κ_{org} of forest aerosols in temperate zones.

4.6. Brief summary of this chapter

The size-resolved *g* distributions and the size-resolved ratios of CCN to CN of atmospheric aerosols were measured at a forest site in Wakayama during summer. The hygroscopicity and CCN activity of the forest aerosols were investigated in view of their diurnal variations and the dependence on particle size and time. The size-resolved *g* during the observation period exhibited a broad unimodal distribution on average. during 0900-2100 JST on NPF event days, when newly-formed particles were present and the fraction of BSOA was large, less hygroscopic particles (g~1.1) appeared in the Aitken mode range and *g* of particles decreased significantly (~15%) both in Aitken and accumulation mode ranges, compared to those on non-event days. The result suggests that newly-formed BSOA was less hygroscopic and decrease the hygroscopicity of pre-existed particles by the condensation. The *g* of particles and κ of organics increased continuously from late afternoon to nighttime regardless of the particle size. Possible reasons are the aging of particles by oxidation, the production of WSOM in the aqueous phase, and the inflow of maritime airs with more hygroscopic particles. The d_{act} and N_{CCN} also changed with the appearance of small less hygroscopic particles during 0900-2100 JST and larger more hygroscopic particles during 2100-0900 JST. The κ of organics and particles were calculated to be 0.13 and 0.17 during 0900-2100 JST, respectively, and the values were up to ~0.30 during 2100-0900 JST. The N_{CCN} increased from the afternoon to the evening, suggesting that aged BSOA contribute to the increase of particle hygroscopicity and N_{CCN}. Particles with highly hygroscopic components, i.e., sulfate, in background airs may have also contributed to the CCN number concentrations.

5. CCN activity with different hygroscopicity of urban aerosol particles and the application to cloud parcel model

5.1. Number-size distributions of aerosol particles

The time series of the number-size distributions and the total number concentrations of aerosol particles are presented in Figures 5.1a and 5.1b. As seen in Figure 5.1a, a large portion of particles were present in the Aitken mode range ($d_{p,dry}$ <100 nm). The mode diameters derived from fittings with a single log-normal curve was 60 ± 19 nm (mean ± SD). Fittings with two log-normal curves gave mean mode diameters of 34 ± 10 nm and 83 ± 18 nm. The total number concentration of aerosols (N_{CN}) from 14.1 to 711 nm was 6932 ± 8379 cm^{-3}. A plausible reason for the dominance of Aitken mode particles could be a large emission of POA in the studied urban area. According to other studies that characterized urban aerosols, hydrocarbon-like organic aerosol (HOA) is likely POA emitted by local combustion and these mainly exist in the Aitken mode. By contrast, oxygenated organic aerosol (OOA) is likely SOA and they mainly exist in the accumulation mode [*Zhang et al.*, 2005a; 2005b]. Another possible reason for the dominance of Aitken mode particles could be the occurrence of new particle formation. The increase of the number concentrations of small particles ($d_{p,dry}$ <40 nm) and the total number concentrations to >10000 cm^{-3} during the observation implied an influence from new particle formation.

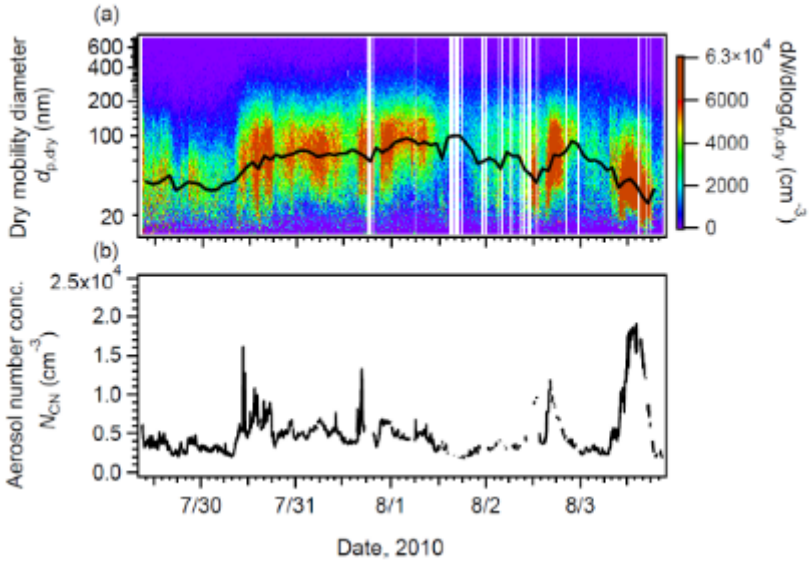

Figure 5.1. Time series of (a) the number-size distributions and (b) the total number concentrations (14.1–711 nm) of aerosol particles. The black line in Figure 3a is the mode diameters derived from single log-normal fittings.

5.2. Distributions of hygroscopic growth factors

The average distributions of *g* as a function of the particle diameter and the average of the normalized distributions are presented in Figures 5.2a and 5.2b, respectively. As seen in the figures, the average *g* distribution is characterized by the presence of less and more hygroscopic modes. Most of the individual distributions of *g* over the 11 time periods were bimodal as well, as shown in Figure 5.3.

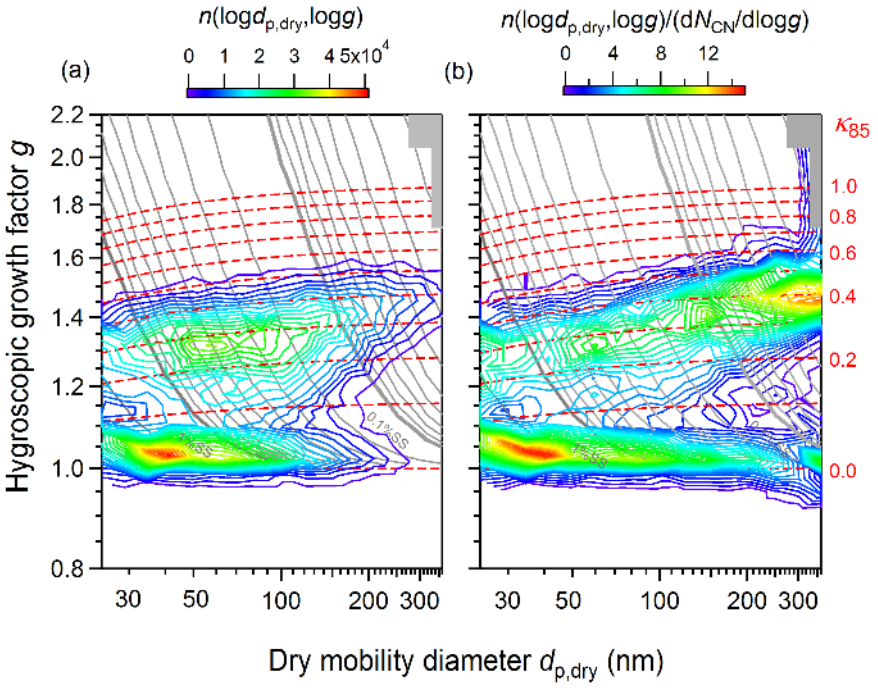

Figure 5.2. (a) Average two-dimensional distribution of the number concentrations of aerosol particles as a function of g and $d_{p,dry}$ at 85% RH and (b) the average of 11 normalized distributions. The dashed red lines represent contours of κ at 85% RH (κ_{85}). The gray contours show critical SS estimated from the κ-Köhler theory [*Mochida et al.*, 2011].

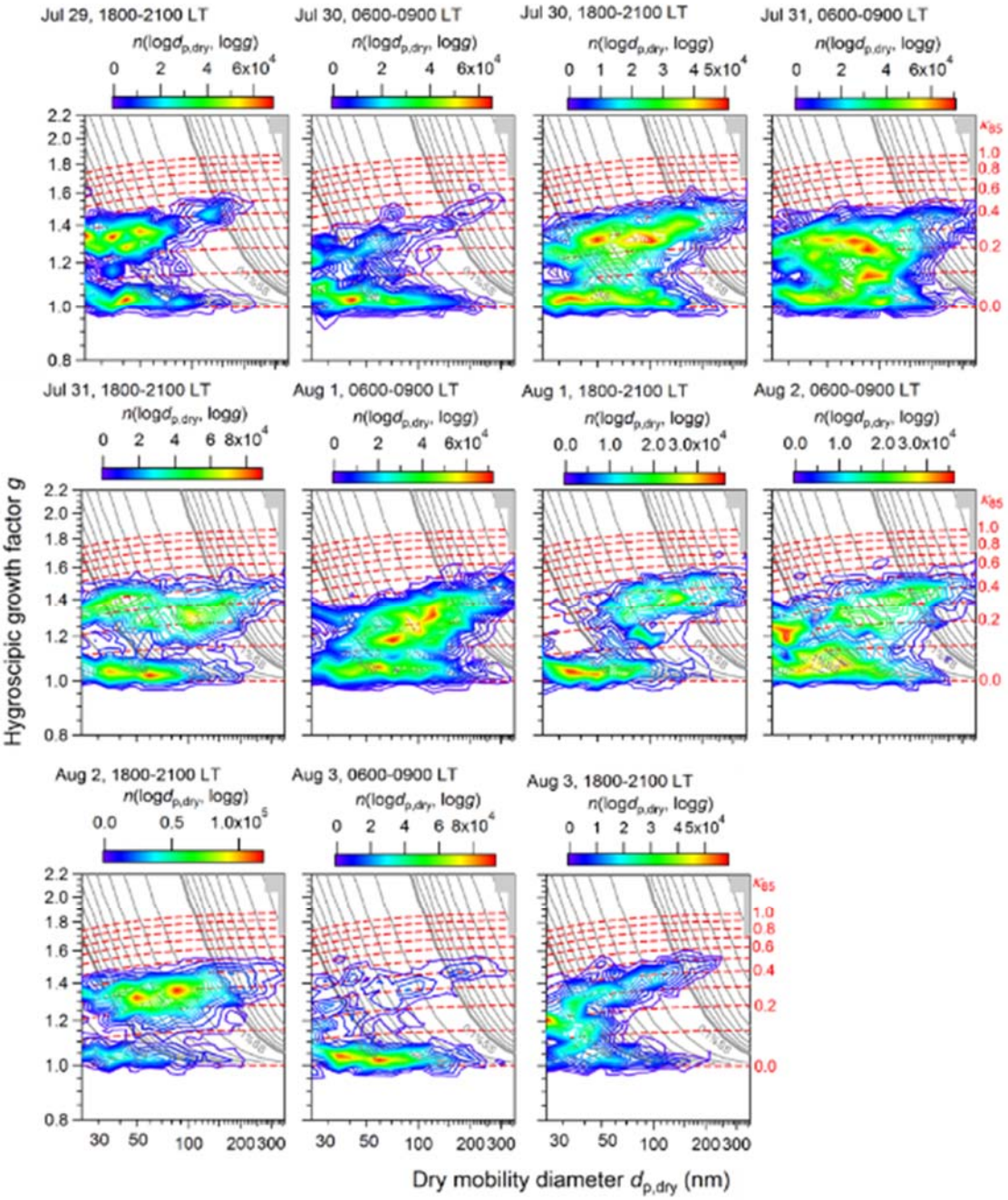

Figure 5.3. HTDMA-derived distributions of the aerosol particle number concentrations as a function of hygroscopic growth factor (g) and dry mobility diameter ($d_{p,dry}$) at 85% RH. The dashed red lines represent the contours of κ at 85% RH (κ_{85}). The gray contours show the critical supersaturation estimated from the κ-Köhler theory.

The average of the number-size distributions and the average of the number fractions of aerosol particles in four different ranges of g are shown in Figures 5.4a and 5.4b. As seen in Figure 5.4a, the concentrations of particles in the lowest hygroscopicity range ($0.8 \leq g < 1.1$) had a maximum in the Aitken mode range ($d_{p,dry} < 100$ nm) and it decreased toward the accumulation mode range ($d_{p,dry} > 100$ nm). By contrast, the concentrations and the number fraction of particles in the highest hygroscopicity range ($1.4 \leq g \leq 2.2$) in the accumulation mode range were substantially higher compared to those in the Aitken mode range. In the case of the particles in the range of $1.1 \leq g < 1.25$, while the shape of the number-size distributions was similar to that of the particles in the lowest hygroscopic range, the size dependence of the number fraction was small.

The less hygroscopic particles may have consisted of BC or primary-emitted HOA, as can be inferred from their compositional characteristics. Furthermore, the high abundance of less hygroscopic particles in the Aitken mode range also supported the contribution of BC and HOA, as discussed in section 5.1. More hygroscopic particles may have consisted of secondary-generated OOA and inorganics as has been suggested for urban aerosols (Tokyo) by *Mochida et al.* [2008]. Aerosols from the East Asian continent [*Aikawa et al.*, 2010; *Yoshitomi et al.*, 2011] as well as those from other parts of Japan might have contributed to the observed more hygroscopic particles, as suggested from the five-day backward air mass trajectories (Figure 5.5) passing near the coast of China. This interpretation is also supported by observation that aerosols from China by the long-range transport had high hygroscopic growth factors in Okinawa, Japan [*Mochida et al.*, 2010]. The finding in this study that the size distribution of more hygroscopic particles is characterized by the larger size than that of less hygroscopic particles was reasonable because more hygroscopic particles may have grown by

condensation, coagulation, and in-cloud processes during the long-range transport. Further, the growth from less hygroscopic to more hygroscopic particles in the local urban air is also possible. *Wang et al.* [2010] reported that the hygroscopicity of non-hygroscopic particles (fresh POA or BC) increased within a few hours during the daytime by the condensation of photochemically formed SOA in Mexico. This process could also explain the size dependence of the number fractions of particles with different g (Figure 5.4b).

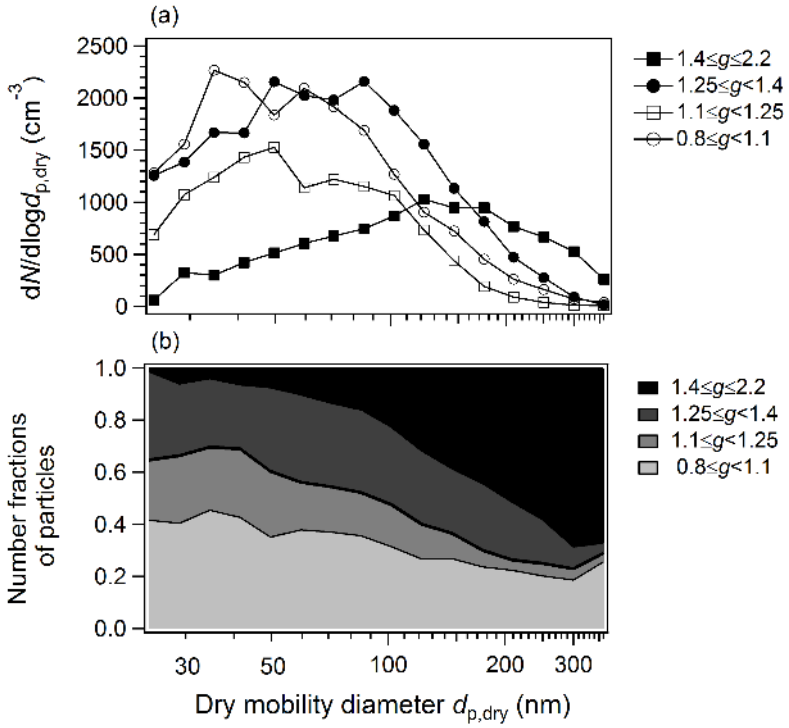

Figure 5.4. (a) Average of the number-size distributions and (b) the average of the number fractions of aerosol particles in the ranges of $0.8 \leq g < 1.1$, $1.1 \leq g < 1.25$, $1.25 \leq g < 1.4$, and $1.4 \leq g \leq 2.2$.

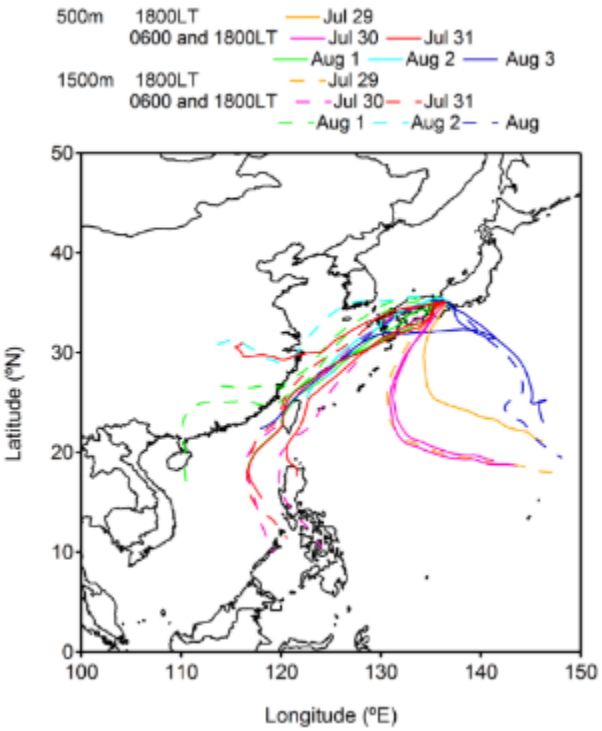

Figure 5.5. Five-day backward air mass trajectories from the observation site (500 and 1500 m above ground level) at 0600 and 1800 LT during the atmospheric observation period. The trajectory analysis was performed using the HYSPLIT model from NOAA Air Resources Laboratory [*Draxler and Rolph*, 2003]. The meteorological data is from GDAS of NCEP. The solid and dashed lines represent the trajectories of air masses at 500 and 1500 m above ground level, respectively.

The individual distributions of *g* over the 11 time periods (Figure 5.3) were mainly bimodal as was also the case of the average distribution. However, in some cases the separation in the mode was not clear, while in others, only the less hygroscopic mode was clearly observed. The substantial variation in the distributions of *g* in Nagoya was in contrast to the unimodal distributions observed at remote locations to the east (the western North Pacific) and to the west (Okinawa) of Nagoya [*Mochida et al.*, 2010; 2011]. The variation may have been influenced by different degrees of mixing of air masses with different origins or local formation of SOA and subsequent aging.

5.3. CCN efficiency spectra of aerosol particles with different hygroscopic growth factors

Figures 5.6a–5.6l show the averages of the measured CCN efficiency spectra and the curves fitted to the averages for aerosol particles with four different g_{set} (1.0, 1.1, 1.25, and 1.4). The parameters obtained by the fitting of CCN efficiency spectra (i.e., F_{max}, $d_{act,CCN}$, σ_{CCN}, and $\sigma_{CCN}/d_{act,CCN}$) are summarized in Table 5.1. The $\sigma_{CCN}/d_{act,CCN}$ values are the measures of the heterogeneity of aerosol particles; the higher the value, the less uniform are the particles [*Rose et al.*, 2008; 2010]. Although the σ values are broadened by the widths of the transfer functions of two DMAs in HTDMA, this effect is not considered in this study.

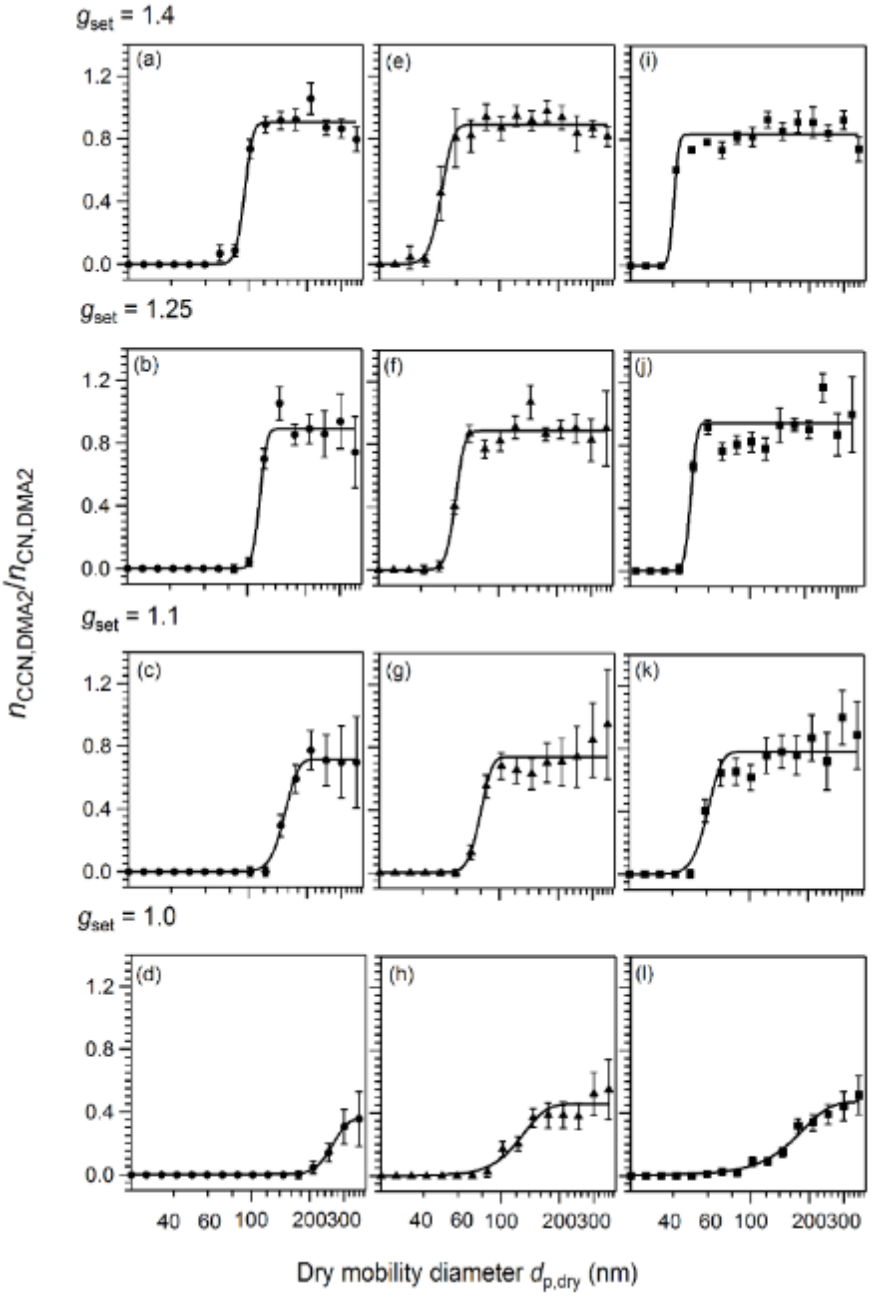

Figure 5.6. The averages of the measured CCN efficiency spectra (symbols) and the curves fitted to the averages (solid lines) for aerosol particles with g_{set} of (a, e, and i) 1.4, (b, f, and j) 1.25, (c, g, and k) 1.1, and (d, h, and l) 1.0 at (a–d) 0.18%, (e–h) 0.49%, and (i–l) 0.95% SS. The bars represent the standard deviation.

Table 5.1. Parameters of the function fitted to the averages of the measured CCN efficiency spectra for atmospheric particles selected with specific g_{set} values and ammonium sulfate particles.

Particle type	g_{set} [a]	SS [b] (%)	F_{max} [c]	$d_{act,CCN}$ [d] (nm)	σ_{CCN} [e]	$\sigma_{CCN}/d_{act,CCN}$
atmospheric aerosols	1.0	0.18	0.36	239.0	40	0.16
		0.49	0.46	123.1	33	0.27
		0.95	0.47	139.4	51	0.36
	(mean)		0.43		42	0.26
	1.1	0.18	0.72	152.7	20	0.13
		0.49	0.74	79.3	9.1	0.11
		0.95	0.78	50.7	7.2	0.14
	(mean)		0.75		12	0.13
	1.25	0.18	0.89	115.6	8.0	0.07
		0.49	0.88	60.0	5.4	0.09
		0.95	0.95	40.1	2.5	0.06
	(mean)		0.91		5.3	0.07
	1.4	0.18	0.90	95.0	7.8	0.08
		0.49	0.89	49.9	5.8	0.11
		0.95	0.83	33.7	1.6	0.01
	(mean)		0.88		5.1	0.08
ammonium sulfate		0.18	0.99	86.3	3.9	0.05
		0.49	0.98	45.3	1.3	0.03
		0.95	0.98	29.7	0.7	0.02
	(mean)		0.98		2.0	0.03

[a]Setting hygroscopic growth factors.

[b]Supersaturations in the CCNC.

[c]The value that $fn_{CCN,DMA2}/n_{CN,DMA2}$ approaches as $d_{p,dry}$ increases.

[d]CCN activation diameters.

[e]The standard deviation of the fitting function.

In the case of more hygroscopic particles with g_{set} of 1.25 and 1.4, $n_{CCN,DMA2}/n_{CN,DMA2}$ increased sharply with increasing dry diameter (Figures 5.6a, b, e, f, i, and j) as represented by small $\sigma_{CCN}/d_{act,CCN}$ values (Table 5.1). The mean values of $\sigma_{CCN}/d_{act,CCN}$ for particles with g_{set} of 1.25 and 1.4 were 0.07 and 0.08, respectively, which were similar to the values of ammonium sulfate particles. The $d_{act,CCN}$ of more hygroscopic particles were smaller than those of less hygroscopic particles with g_{set} of 1.0 and 1.1 at respective SS conditions (Figures 5.6c, d, g, h, k, and l), indicating high CCN activity as expected from higher g_{set}. F_{max} values were close to 1.0, indicating that particles well above $d_{act,CCN}$ were mostly activated. Both $\sigma_{CCN}/d_{act,CCN}$ values similar to that of ammonium sulfate and high F_{max} values suggested that the hygroscopicity at 85% RH was tightly linked to the CCN activity of particles under supersaturated conditions.

In the case of particles with g_{set} of 1.0, the increase of $n_{DMA2,CCN}/n_{DMA2,CN}$ with increasing dry diameter was not as sharp (Figures 5.6d, h, and l). The mean $\sigma_{CCN}/d_{act,CCN}$ was 0.26, which was substantially larger than that for more hygroscopic particles. This large $\sigma_{CCN}/d_{act,CCN}$ is hypothesized to be caused in part by the fact that the hygroscopicity κ of particles with g_{set} of 1.0 can vary by many orders of magnitude (the order of κ can be infinitely low). It is consistent with the result that the CCN effective spectrum predicted by HTDMA data also have the same tendency (large $\sigma_{CCN}/d_{act,CCN}$ of less hygroscopic particles) as shown in Figure 5.7 (see the next section). $d_{act,CCN}$ were also larger than those for more hygroscopic particles, indicating low CCN activity as expected from low g_{set}. F_{max} values were much less than 1.0: 0.36, 0.46, and 0.47 at 0.18%, 0.49%, and 0.95% SS, respectively. This finding showed that the fractions of

inactive particles were high even in the case of high SS and large particles within the measured size range. The low F_{max} values indicated either that the hygroscopicity of less hygroscopic particles was not uniform (in time as well as size, because the result was from the averages of multiple measurements) or that the asphericity of particles showed large variation. The nonuniformity or asphericity of particles may also affect the large $\sigma_{CCN}/d_{act,CCN}$ values in part. However, we did not obtain the contribution quantitatively.

In the case of particles with g_{set} of 1.1, the above-mentioned characteristics of particles with g_{set} of 1.0 (i.e., moderate increase of $n_{DMA2,CCN}/n_{DMA2,CN}$ versus $d_{p,dry}$ and F_{max} values substantially less than unity) were observed, although their patterns were not as clear as particles with g_{set} of 1.0 (Figures 5.6c, g, and k). The CCN-inactive particles with g_{set} of 1.0 and 1.1, as evidenced by F_{max} values less than unity, may have been fresh and uncoated BC. Previous studies in urban sites had suggested that these particles have the lowest CCN activity among particles with the same mobility diameters [*Kuwata et al.*, 2008; *Rose et al.*, 2010].

5.4. Prediction of CCN activation diameters from hygroscopic growth factor distributions and comparison to measured activation diameters

To examine the prediction of the CCN activation of aerosol particles from measured hygroscopicity, the CCN efficiency spectra were estimated from the measured distributions of g. The averages of the predicted CCN efficiency spectra at each SS condition and the curves fitted to the averages, for aerosol particles with four different g_{set} (1.0, 1.1, 1.25, and 1.4) are present in Figure 5.8, together with the averages of measured CCN efficiency spectra and the curves fitted to them (see Figure 5.7 for the standard deviation). Here, particles in the range of $0.8 \leq g < 1.0$ were assumed to be CCN-

inactive. The figure shows that the differences of the shapes of CCN efficiency spectra caused by the difference of g_{set} were predicted to some extent.

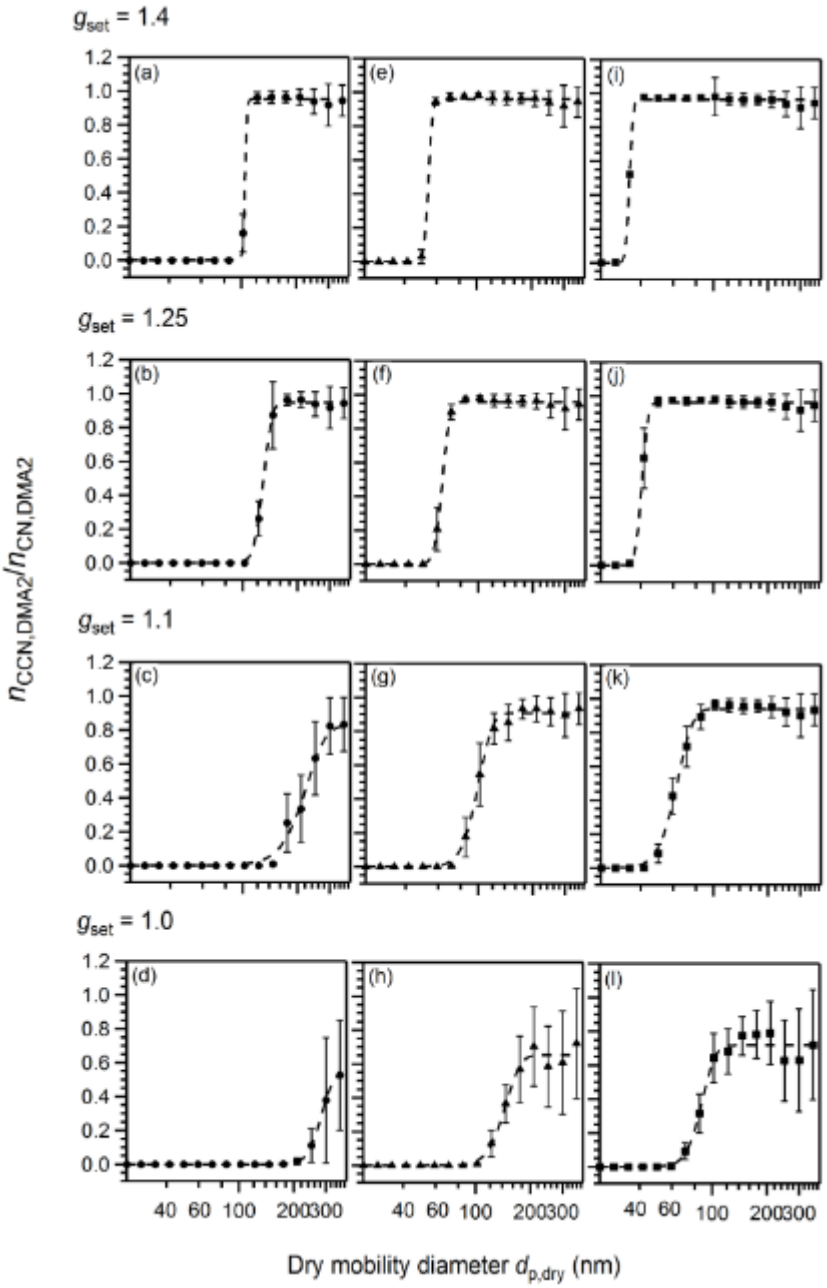

Figure 5.7. The averages of the predicted CCN efficiency spectra (symbols) and the curves fitted to the averages (dashed lines) for aerosol particles with g_{set} of (a, e, and i) 1.4, (b, f, and j) 1.25, (c, g, and k) 1.1, and (d, h, and l) 1.0 at (a–d) 0.18%, (e–h) 0.49%, and (i–l) 0.95% SS. The bars represent the standard deviation.

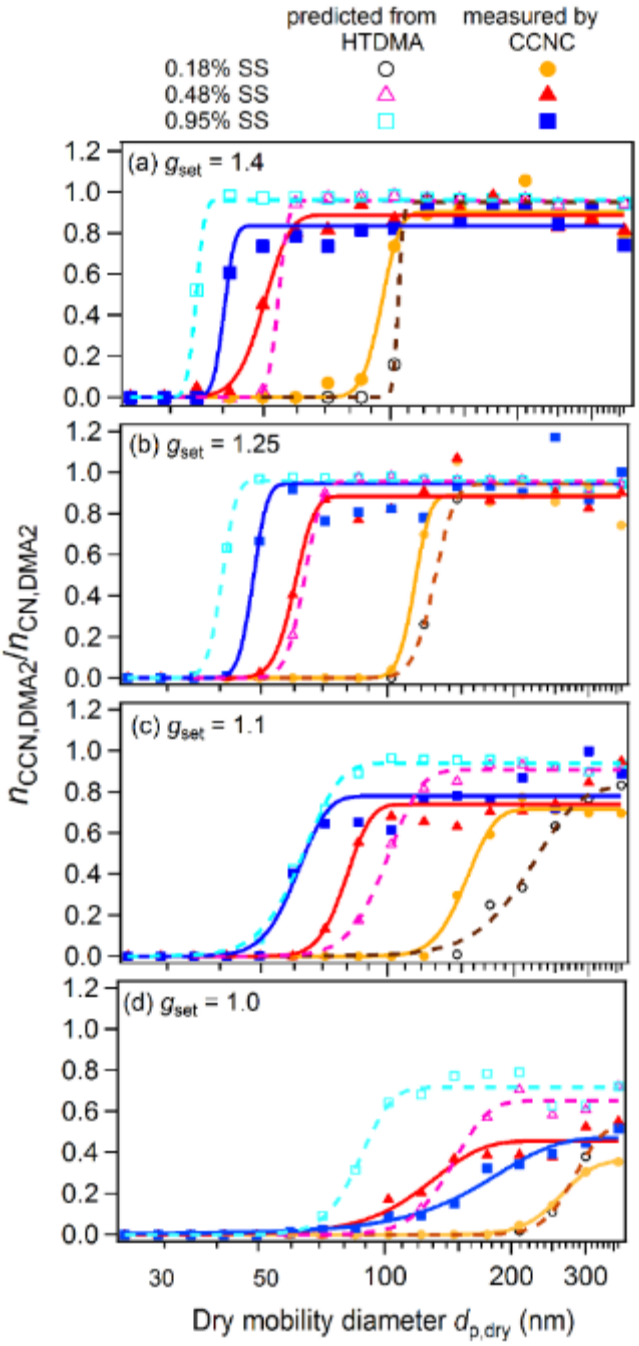

Figure 5.8. The averages of the CCN efficiency spectra predicted from the distribution of g at 85% RH (open symbols) and those measured using the CCNC (solid symbols) for aerosol particles with g_{set} of (a) 1.4, (b) 1.25, (c) 1.1, and (d) 1.0. The dashed and solid lines represent the curves fitted to the averages of the predicted and measured spectra, respectively.

The $\sigma_{g85}/d_{act,g85}$, where σ_{g85} and $d_{act,g85}$ are, respectively, σ and d_{act} obtained by the fitting of the predicted CCN efficiency spectra presented in Figure 5.8, for more hygroscopic particles with g_{set} of 1.25 and 1.4 were on average very small (0.08 and 0.04, respectively) as in the case of $\sigma_{CCN}/d_{act,CCN}$ (0.07 and 0.08, respectively). In contrast, less hygroscopic particles with g_{set} of 1.0 and 1.1 had on average a large $\sigma_{g85}/d_{act,g85}$ (0.16 and 0.19, respectively) as in the case of $\sigma_{CCN}/d_{act,CCN}$ (0.26 and 0.13, respectively). The prediction of the CCN efficiency spectra was, however, rather poor for particles with g_{set} of 1.0 (Figure 5.8d), which was possibly caused by the asphericity of the particles (aggregate or fractal structures). Quantitative evaluation of the F_{max} values prediction was not performed because the validity of the estimation of CCN-inactive particles from g<1.0 was not clear.

The relation between $d_{act,CCN}$ derived from the averages of measured CCN efficiency spectra and the activation diameters predicted from the distributions of g ($d_{act,g85}$) is presented in Figure 5.9. $d_{act,CCN}$ were smaller than $d_{act,g85}$ with one exception, indicating that the measured CCN activity was higher than that predicted from the hygroscopicity data. In particular, plots for less hygroscopic particles showed large deviations from the 1:1 line. The mean values of $d_{act,g85}$, $d_{act,CCN}$, and the activation diameters predicted from g_{set} of 1.0, 1.1, 1.25 and 1.4 ($d_{act,gset}$) are summarized in Table 5.2. Whereas $d_{act,g85}$ from $d_{act,CCN}$ agreed within 12% for more hygroscopic particles, the disagreement was larger (16%–41%) for less hygroscopic particles. Figure 5.9 and Table 5.2 also shows the relationship between $d_{act,CCN}$ and $d_{act,gset}$, the value without the correction for the width of g. While $d_{act,gset}$ and $d_{act,g85}$ agreed within 4% for more hygroscopic particles, the disagreement was very large (7%–412%) for less hygroscopic particles. The results in Figure 5.9 show that taking the width of g into consideration

shifts the plots toward the 1:1 line. Hence, this consideration is probably important for the precise prediction of CCN activation diameters. CCN activation diameters calculated from independent measured and predicted CCN efficiency spectra (not from the averages) were also obtained and the mean values are similar to the result obtained by use of average CCN efficiency spectra in Figure 5.9 (within 15% except for one point for particles with g_{set} of 1.0 at 0.49% SS). These data were not used for the analysis in this section because some of the fittings to the predicted CCN efficiency spectra failed or resulted in exceptional curves.

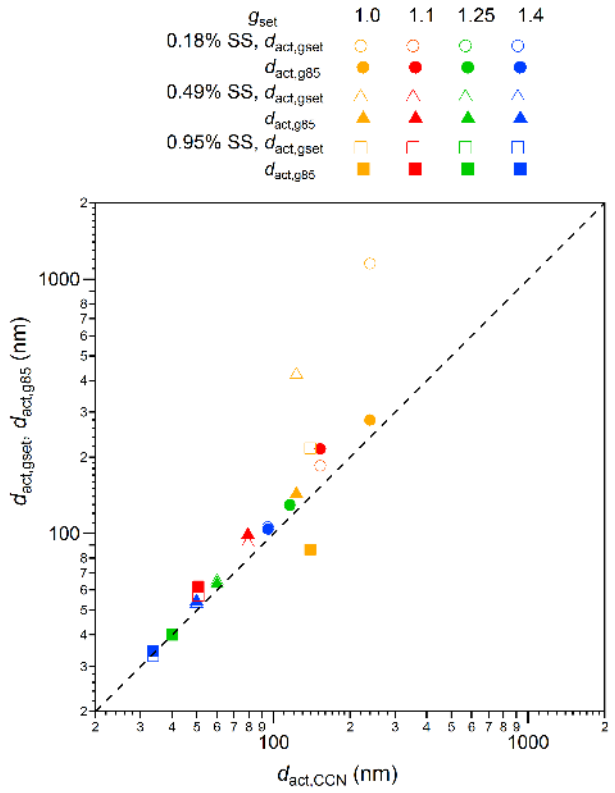

Figure 5.9. The CCN activation diameters predicted from g_{set} with and without consideration of the width of the transfer function of DMA1 (i.e., $d_{act,g85}$ and $d_{act,gset}$, respectively) plotted against the measured CCN activation diameters ($d_{act,CCN}$). These values were obtained from the fittings to the averages of the predicted and measured CCN efficiency spectra.

Table 5.2. Summary of predicted and measured CCN activation diameters and other values derived from the activation diameters.

g_{set} [a]	SS [b] (%)	$d_{act,gset}$ [c] (nm)	$d_{act,g85}$ [d] (nm)	$d_{act,CCN}$ [e] (nm)	κ_{gset} [f]	κ_{85} [g]	κ_{CCN} [h]	$d_{act,g85}/d_{act,CCN}$	$d_{act,gset}/d_{act,g85}$	$d_{act,gset}/d_{act,CCN}$
1.0	0.18	1153	279.9	239.0	0	0.018	0.029	1.17	4.12	4.82
	0.49	422	143.1	123.1	0	0.016	0.026	1.16	2.95	3.43
	0.95	217	86.7	139.4	0	0.018	0.002	0.62	2.50	1.56
(mean)					0	0.017	0.019	0.99	3.19	3.27
1.1	0.18	185	215.4	152.7	0.062	0.040	0.112	1.41	0.86	1.21
	0.49	92	98.8	79.3	0.066	0.054	0.105	1.25	0.93	1.16
	0.95	57	62.1	50.7	0.071	0.055	0.106	1.22	0.92	1.12
(mean)					0.066	0.050	0.108	1.29	0.90	1.17
1.25	0.18	130	129.1	115.6	0.183	0.187	0.260	1.12	1.01	1.12
	0.49	65	63.3	60.0	0.197	0.210	0.246	1.06	1.03	1.08
	0.95	40	40.3	40.1	0.215	0.214	0.218	1.00	0.99	1.00
(mean)					0.198	0.204	0.241	1.06	1.01	1.07
1.4	0.18	106	104.3	95.0	0.336	0.355	0.468	1.10	1.02	1.12
	0.49	53	54.1	49.9	0.366	0.340	0.430	1.08	0.98	1.06
	0.95	33	34.5	33.7	0.401	0.346	0.370	1.02	0.96	0.98
(mean)					0.368	0.347	0.423	1.07	0.98	1.05

[a]Setting hygroscopic growth factors.

[b]Supersaturations in the CCNC.

[c]CCN activation diameters predicted from g_{set} without consideration of the width of the transfer function of DMA1.

[d]Same as c but with consideration of the width of the transfer function of DMA1.

[e]CCN activation diameters measured using the CCNC.

[f]κ values calculated from $d_{act,gset}$.

[g]Same as f but calculated from $d_{act,g85}$.

[h]Same as f but calculated from $d_{act,CCN}$.

However, the width of g does not fully explain the discrepancy from the 1:1 line. A possible cause of the differences between $d_{act,g85}$ and $d_{act,CCN}$ was the surface tension reduction caused by organics. Based on analysis of filter extracts, the surface tension reduction was reported to be approximately 25% in the Po Valley [*Facchini et al.*, 2000] and 5%–22% in Mexico [*Pádro et al.*, 2010]. Given that the percentage decrease of CCN activation diameters by the surface tension with respect to that of water was comparable to the percentage decrease of the surface tension itself [*Wex et al.*, 2008], the expected range of the decrease of CCN activation diameters by surface tension was estimated to be approximately 5%–25% in the atmosphere.

Other possible causes of the differences between $d_{act,g85}$ and $d_{act,CCN}$ originate from the effects of solutes. The κ values vary up to ~20%, depending on the concentrations of aqueous solutions (corresponding to ~7% in CCN activation diameters). For example, in ammonium sulfate particles, κ calculated from g at ~90% RH (0.53) was 13% smaller than that calculated from CCN measurements (0.61) [*Petters and Kreidenweis*, 2007]. *Kreidenweis et al.* [2008] reported that the water contents computed from κ parameterization $(V_w/V_s)_\kappa$ and those from the Aerosol Inorganic Model [*Clegg et al.*, 1998] $(V_w/V_s)_{AIM}$ for some inorganics and organics agreed within ~20% at RH>85% (based on an assessment of up to 99% RH). Hence, the deviation of κ was estimated to be within ~20% at RH>85%. The influence of sparingly soluble components with degree of dissolution that depends on the water content in particles is potentially great. *Wex et al.* [2009] reported a large increase in g of laboratory-generated pure SOA particles at RH>98%, suggesting possible overestimation of CCN activation diameters based on the measured g at 85% RH. Moreover, the sensitivity of mobility diameter to water uptake depends on the particle

shape. *Tritscher et al.* [2011] reported that the measurement based on the mobility diameter using the DMA led to underestimation of the hygroscopicity for soot particles because of morphology changes.

While small differences of $d_{act,g85}$ from $d_{act,CCN}$ for more hygroscopic particles can be explained by either or both the surface tension reduction and the underestimation of the amount of solutes, it is difficult to explain the differences for less hygroscopic particles by surface tension reduction alone. Although it was not clear which mechanism was the main contribution to the differences, the results indicated that the amounts of soluble materials in less hygroscopic particles were larger than those estimated from the measured hygroscopic growth at 85% RH. Assuming the surface tension of pure water and a spherical particle shape, the mean values of κ_{CCN} calculated from $d_{act,CCN}$ on particles with g_{set} of 1.0, 1.1, 1.25, and 1.4 were 0.02, 0.11, 0.24, and 0.42, respectively (Table 2). In contrast, the mean values of κ_{85} calculated from $d_{act,g85}$ for particles with g_{set} of 1.0, 1.1, 1.25, and 1.4 were 0.02, 0.05, 0.20, and 0.35, respectively. While the mean values of κ_{CCN} were 1.0–1.4 times κ_{85} for more hygroscopic particles with g_{set} of 1.25 and 1.4, the mean values of κ_{CCN} were 0.1–2.8 times κ_{85} for less hygroscopic particles with g_{set} of 1.0 and 1.1. The differences of κ_{CCN} from κ_{85} for less hygroscopic particles were in general larger than those of more hygroscopic particles as was expected from the comparison in Figure 5.4.3.

The finding that κ_{CCN} of less hygroscopic particles were larger than κ_{85} strongly suggested the presence of a hydrophilic component that could not be detected accurately using the HTDMA. If particles are assumed to be ammonium sulfate with κ of 0.58 (derived from the calibration of the CCNC) with an insoluble component with κ of 0, the mean values and ranges of the soluble component volume fractions (ε_{sol}) in particles

with g_{set} of 1.0 and 1.1 are calculated to be 3.0% (2.8%–3.3%) and 8.6% (6.3%–10%), respectively. If the soluble component in the particles are OOA or SOA (κ~0.1), the mean values and ranges of ε_{sol} are calculated to be 17% (16%–18%) and 50% (40%–55%) for particles with g_{set} of 1.0 and 1.1, respectively. This suggests that the fraction of soluble components in less hygroscopic particles could be substantial, depending on the hygroscopicity of the chemical components.

5.5. Prediction of cloud droplet formation and growth from hygroscopic growth factor distributions

In the base case of the cloud parcel model, the cloud droplet number concentrations (N_{cd}) and the effective radius (R_{eff}) were estimated from the distributions of g, which were measured using the HTDMA. Further, the number concentrations of CCN (N_{CCN}) at the maximum SS in the model (S_{max}) were estimated. The average SS profiles for four updraft velocities (v) had a maximum at ~530 m AGL and showed rapid decreases above that height. S_{max} depended on the updraft velocity and the total number concentrations of aerosol particles (N_{CN}); the mean values of S_{max} at v of 0.1, 0.5, 1.0, and 5.0 m s^{-1} were 0.15%, 0.34%, 0.48%, and 1.1%, respectively. Figure 5.10a shows N_{CN} versus N_{cd} in the base case for 11 time periods (Figure 5.2) under different conditions of v. Whereas N_{cd} depended on v and N_a if v was high, N_{cd} remained small if v was low. This indicated that the former was in aerosol- and updraft-sensitive regimes, and that the latter was in an updraft-limited regime [*Reutter et al.*, 2009]. Figure 10b shows N_{CCN} (in hypothetical equilibrium conditions at S_{max}) versus N_{cd}. The hypothetical CCN at S_{max} were not all activated as cloud droplets, particularly in the cases of low v and large N_{CCN}. This result may be associated with the kinetic mechanism

not all particles grow to become cloud droplets even if S_{crit} of particles is smaller than S_{max}, because of the insufficient time to activate [*Nenes et al.*, 2001].

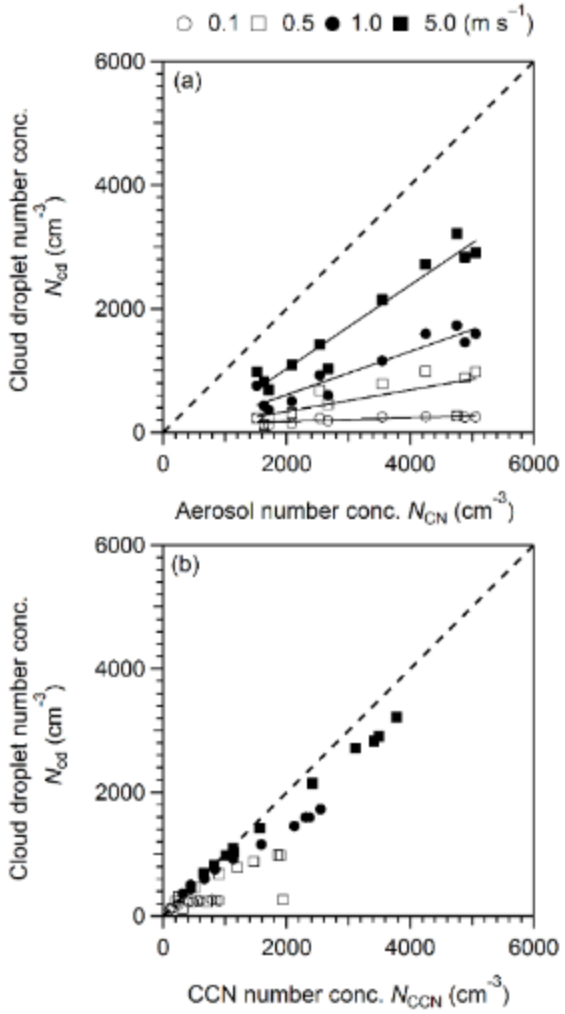

Figure 5.10. The plots of (a) N_{CN} and (b) N_{CCN} against the cloud droplet number concentrations N_{cd}. The results are from the base case of the cloud parcel model with v of 0.1 (open circles), 0.5 (open squares), 1.0 (solid circles), and 5.0 m s^{-1} (solid squares).

Model calculations in the base case showed that corrections for the difference of $d_{act,g85}$ from $d_{act,CCN}$ (section 5.4) and the presence of CCN-inactive particles (section 5.3) based on the results from the HTDMA and the CCNC, had a small influence on the

cloud droplet formation. The difference of $d_{act,g85}$ from $d_{act,CCN}$ was considered so that particles in the ranges of $0.8 \leq g < 1.1$, $1.1 \leq g < 1.25$, $1.25 \leq g < 1.4$, and $1.4 \leq g \leq 2.2$ had κ_{CCN} (Table 5.2) if their original κ_{85} were lower than κ_{CCN}. Further, the presence of CCN-inactive particles (F_{max} values less than unity) with g_{set} of 1.0 and 1.1 (Table 5.1) was also considered by multiplying the number concentrations of particles in the ranges of $0.8 \leq g < 1.05$ and $1.05 \leq g \leq 1.15$ by 0.43 and 0.75, respectively. If model calculations were performed without the corrections for the difference of $d_{act,g85}$ from $d_{act,CCN}$ and the presence of CCN-inactive particles, N_{CCN}, N_{cd} and R_{eff} at v of 1.0 m s^{-1} (or 5.0 m s^{-1}) changed within 2% (5%), 2% (5%), and 1% (2%), respectively. The very small changes indicated that N_{CCN}, N_{cd} and R_{eff} were reasonably estimated from the distributions of g and the number-size distributions from the HTDMA and SMPS, even without the CCNC data. However, the corrections explained above were included in the model to seek higher reliability in the estimates for this study.

5.6. Contribution of aerosol particles with different hygroscopicity to cloud droplet formation and growth

In this section, the contributions of particles grouped by hygroscopicity to the number concentrations and properties of cloud droplets are assessed. The primary objective of this sensitivity analysis was to investigate the importance of less hygroscopic particles, which were abundant in the urban aerosol, for cloud droplet formation in the urban atmosphere. This was performed by investigating the changes in N_{CCN}, N_{cd} and R_{eff} by considering the presence of less hygroscopic particles in addition to more hygroscopic particles ($0.8 \leq g \leq 2.2$), as compared to the hypothetical cases that only more hygroscopic particles ($g \geq 1.25$) were present. If urban aerosols are taken as an

analogy, the latter case corresponds to aerosols entering the urban area after long-range transport, and the former corresponds to aerosols after less hygroscopic particles are added to these aerosols over the urban area [*Zaveri et al.*, 2010].

Figures 5.11a–5.11c show the mean values of $N_{CCN,}$ N_{cd} and R_{eff} in the cases of particles in the ranges of $0.8 \leq g \leq 2.2$ (i.e., all particles are present), and $1.25 \leq g \leq 2.2$ (only more hygroscopic particles are present). The results in the other cases that particles in the ranges of $1.1 \leq g \leq 2.2$ and $1.4 \leq g \leq 2.2$ were considered are also shown in figures. Figures 5.11d–5.11f show the ratios of $N_{CCN,}$ N_{cd} and R_{eff} in each case to those variables over the entire range of $0.8 \leq g \leq 2.2$ ($N_{CCN,all}$, $N_{cd,all}$ and $R_{eff,all}$). The mean values in the four cases are summarized in Table 5.3.

As seen in Figure 5.11 and Table 5.3, N_{CCN}, N_{cd} and R_{eff} depended largely on v. If v was high (1.0 and 5.0 m s^{-1}), N_{cd} increased and R_{eff} decreased markedly considering the particle had a wider range of g in the model. In the base case that all particles with $0.8 \leq g \leq 2.2$ were included at v of 1.0 m s^{-1} (or 5.0 m s^{-1}), N_{cd} was 18% (36%) larger and R_{eff} was 5% (10%) smaller on average, as compared to the case that only more hygroscopic particles were present. N_{CCN} was also larger on average by 27% (43%). In contrast, if v was very low (0.1 m s^{-1}), N_{CCN}, N_{cd} and R_{eff} did not show differences regardless of the model cases. The ratio of $N_{cd}/N_{cd,all}$ was about one except for the case when only particles with g larger than 1.4 were considered (Figure 5.11e). This suggested that most of the particles that could be activated as cloud droplets were highly hygroscopic ($g \geq 1.4$) at low v and low SS. From this, it was apparent that the presence/absence of less hygroscopic particles was not important for the formation of cloud droplets under extremely low v.

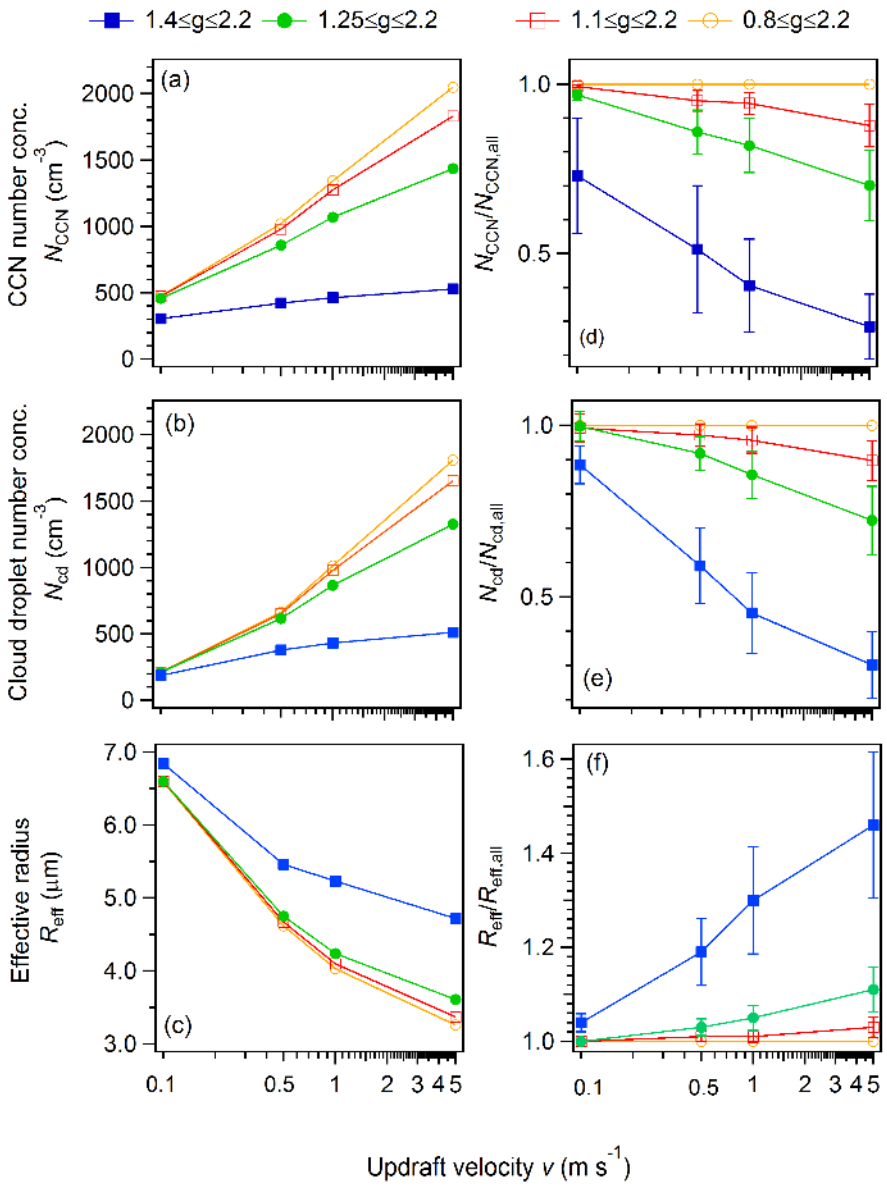

Figure 5.11. Mean values of (a) N_{CCN}, (b) N_{cd}, and (c) R_{eff} with consideration of particles in different ranges of g (blue: $1.4 \leq g \leq 2.2$, green: $1.25 \leq g \leq 2.2$, red: $1.1 \leq g \leq 2.2$, yellow: $0.8 \leq g \leq 2.2$), and the means and standard deviations of (d) $N_{CCN}/N_{CCN,all}$, (e) $N_{cd}/N_{cd,all}$ and (f) $R_{eff}/R_{eff,all}$. $N_{CCN,all}$, $N_{cd,all}$, and $R_{eff,all}$ denote N_{CCN}, N_{cd}, and R_{eff} in the case of $0.8 \leq g \leq 2.2$.

Table 5.3. Mean and standard deviation of N_{CCN}, N_{cd} and R_{eff}, and the ratios of N_{CCN}, N_{cd} and R_{eff} to those in the case of $0.8 \leq g \leq 2.2$ ($N_{CCN,all}$, $N_{cd,all}$ and $R_{eff,all}$).

v	0.1 m s	0.5 m s	1.0 m s	5.0 m s
N_{CCN}[b] base case($0.8 \leq g \leq 2.2$)	476±298 (+4%)	1024±684 (+19%)	1358±867 (+27%)	2061±1211 (+43%)
$1.1 \leq g \leq 2.2$	473±296 (+3%)	979±666 (+14%)	1277 ±836 (+19%)	1832 ±1139 (+27%)
$1.25 \leq g \leq 2.2$	458±283	859±567	1071±677	1437±897
$1.4 \leq g \leq 2.2$	306±151 (−33%)	423±202 (−51%)	462±228 (−57%)	529±279 (−63%)
N_{cd}[c] base case($0.8 \leq g \leq 2.2$)	212±57 (+1%)	665±302 (+8%)	1014±516 (+18%)	1809±969 (+36%)
$1.1 \leq g \leq 2.2$	211±56 (+0%)	652±307 (+6%)	981±517 (+13%)	1655±945 (+25%)
$1.25 \leq g \leq 2.2$	211±56	617±292	866±447	1326±772
$1.4 \leq g \leq 2.2$	187±49 (−11%)	379±157 (−38%)	431±187 (−50%)	511±258 (−62%)
R_{eff}[d] base case($0.8 \leq g \leq 2.2$)	6.59±0.6 (−0%)	4.62±0.8 (−3%)	4.03±0.7 (−5%)	3.26±0.6 (−10%)
$1.1 \leq g \leq 2.2$	6.60±0.6 (−0%)	4.67±0.8 (−2%)	4.10±0.8 (−3%)	3.37±0.6 (−7%)
$1.25 \leq g \leq 2.2$	6.60±0.6	4.75±0.9	4.24±0.8	3.61±0.7
$1.4 \leq g \leq 2.2$	6.84±0.7 (+4%)	5.46±0.9 (+15%)	5.23±0.9 (+23%)	4.72±0.8 (+31%)
$N_{CCN}/N_{CCN,all}$ base case($0.8 \leq g \leq 2.2$)	1.00	1.00	1.00	1.00
$1.1 \leq g \leq 2.2$	0.99±0.01 (−1%)	0.95±0.03 (−5%)	0.93±0.04 (−7%)	0.87±0.07 (−13%)
$1.25 \leq g \leq 2.2$	0.97±0.01 (−3%)	0.86±0.06 (−14%)	0.81±0.08 (−19%)	0.70±0.11 (−30%)
$1.4 \leq g \leq 2.2$	0.73±0.17 (−27%)	0.51±0.19 (−49%)	0.40±0.13 (−60%)	0.28±0.10 (−72%)
$N_{Cd}/N_{Cd,all}$ basecase($0.8 \leq g \leq 2.2$)	1.00	1.00	1.00	1.00
$1.1 \leq g \leq 2.2$	0.99±0.04 (−1%)	0.97±0.03 (−3%)	0.96±0.04 (−4%)	0.90±0.06 (−10%)
$1.25 \leq g \leq 2.2$	0.99±0.04 (−1%)	0.92±0.05 (−8%)	0.86±0.07 (−14%)	0.72±0.10 (−28%)
$1.4 \leq g \leq 2.2$	0.89±0.06 (−11%)	0.59±0.11 (−41%)	0.45±0.12 (−55%)	0.30±0.10 (−70%)
$R_{eff}/R_{eff,all}$ base case($0.8 \leq g \leq 2.2$)	1.00	1.00	1.00	1.00
$1.1 \leq g \leq 2.2$	1.00±0.01 (+0%)	1.01±0.01 (+1%)	1.01±0.02 (+1%)	1.03±0.02 (+3%)
$1.25 \leq g \leq 2.2$	1.00±0.01 (+0%)	1.03±0.02 (+3%)	1.05±0.03 (+5%)	1.11±0.05 (+11%)
$1.4 \leq g \leq 2.2$	1.04±0.02 (+4%)	1.19±0.07 (+19%)	1.30±0.12 (+30%)	1.46±0.16 (+46%)

[a]Updraft velocity.

[b]Number concentrations of CCN.

[c]Number concentrations of cloud droplets.

[d]Effective radius of cloud droplets.

The results in Figure 5.11 and Table 5.3 show that the presence of less hygroscopic particles contributed substantially to N_{CCN} and N_{cd} and led to smaller cloud droplets except in the case of small v. *Facchini et al.* [1999] reported that a 20% increase of N_{CCN} led to 1% enhancement of local TOA albedo and a decrease of −1 W m^{-2} radiative forcing in the case of the formation of stratus clouds (SS of ~0.5%). In this study, the presence of less hygroscopic particles contributed to a 27% increase of N_{CCN} with v of 1.0 m s^{-1} at S_{max} of ~0.47% (Figure 10d), which may corresponded to a decrease in the local radiative forcing on the order of 1 W m^{-2}.

Results from the cloud parcel model showed that the hygroscopicity of aerosol particles has a large influence on the CCN and cloud droplet activation, as suggested from recent studies [*Anttila et al.*, 2009; *Liu and Wang*, 2010]. The varying importance of less hygroscopic particles to cloud droplet formation depending on v illustrated the importance of information about the hygroscopicity as well as size distribution. This result demonstrated that HTDMA-derived two-dimensional particle number distributions versus g and $d_{p,dry}$ are useful to analyze the cloud droplet activation based on it. For this purpose, the CCNC data may not be necessary because there was little bias from the differences of $d_{act,g85}$ from $d_{act,CCN}$ (i.e., surface tension and solute effect) and F_{max} values less than unity (i.e., presence of inactive particles). However, these variables have important implications for the properties and processing of less hygroscopic particles, for example, the degree of change in hygroscopicity of less hygroscopic particles by aging in the atmosphere.

5.7. Brief summary of this chapter

The size-resolved ratios of CCN to CN of atmospheric aerosol particles with specific *g* of 1.0, 1.1, 1.25 and 1.4 and the size-resolved *g* distributions were measured at an urban site during summer in Nagoya in 2010, to investigate the CCN activity of less and more hygroscopic particles individually. The CCN efficiency spectra of less hygroscopic particles was characterized by the dominance of CCN-inactive particles, while that of more hygroscopic particles was characterized by the dominance of CCN-active particles. The d_{act} predicted from size-resolved *g* distributions using HTDMA for less hygroscopic particles showed large difference with the measured d_{act}, while they showed small difference for more hygroscopic particles. Surface tension reduction, solute effects, and asphericity of particles are among the factors that may contribute to the large discrepancy, in particular in the case of less hygroscopic particles. The model simulation for the cloud droplet formation based on the size-resolved *g* distributions showed that the influence of less hygroscopic particles on the number concentrations and the effective radii of cloud droplets is large.

Appendix.

Influences of multiply charged particles on data of hygroscopic growth and CCN activation

The particles selected in DMA1 of the HTDMA include multiply charged particles in addition to singly charged particles. The presence of multiply charged particles engenders some biases of the measured data [*Duplissy et al.*, 2009; *Gysel et al.*, 2009] because the changes in the electrical mobility of particles by the hygroscopic growth depend on the dry diameters, which differ for particles with same electrical

mobility but with different numbers of charges. Moreover, the differences of g distributions of singly and multiply charged particles bias the g distributions obtained on the assumption that all particles with charges are singly charged. In this study, these biases are considered as explained below. The former of the biases was assessed by calculating the differences of g of multiply charged particles from that of singly charged particles having the same mobility diameter. The biases of g of doubly and triply charged particles are presented respectively in Figures A1a and A1b. As the figures show, the biases of g for doubly and triply charged particles in the range of $0.8 \leq g \leq 2.2$ are within 9% and 13%, respectively. The biases of particles with g of 1.0, 1.1, 1.25, and 1.4 for doubly and triply charged particles are within 6% and 7%, respectively. Figures A2a–A2d present the number fractions of singly, doubly, and triply charged particles in the four ranges of g. In the range of $0.8 \leq g < 1.4$, the fraction of singly charged particles is more than 80% in most of the cases of the averages at each $d_{p,dry}$. In the range of $1.4 \leq g \leq 2.2$, the fraction of singly charged particles is more than 60% in all but one of the cases of the averages at each $d_{p,dry}$. If the biases of $d_{act,gset}$ and $d_{act,g85}$ are assumed to be given by the products of the number fraction of multiply charged (i.e., either doubly or triply) particles and their biases of g, then the biases of $d_{act,gset}$ and $d_{act,g85}$ with 20% multiply charged (i.e., doubly or triply) particles are within 1% for particles with g_{set} of 1.0, 1.1, and 1.25. The biases of $d_{act,gset}$ and $d_{act,g85}$ with 40% multiply charged (i.e., doubly or triply) particles are within 3% for particles with g_{set} of 1.4. Comparison of this result to that in Figure A4 shows that the biases attributable to the differences of g of multiply charged particles are not remarkable.

The latter of the two biases, which results from the differences of g distributions of singly charged particles and those of multiply charged particles are evaluated using the following equation.

$$\left[\left. \frac{dN}{d\log d_{\mathrm{p,dry}}} \right|_{d_{\mathrm{p,dry}}=d_1} \bullet l(d_j) f(d_1,1) + \left. \frac{dN}{d\log d_{\mathrm{p,dry}}} \right|_{d_{\mathrm{p,dry}}=d_2} \bullet l(d_j) f(d_2,2) + \left. \frac{dN}{d\log d_{\mathrm{p,dry}}} \right|_{d_{\mathrm{p,dry}}=d_3} \bullet l(d_j) f(d_3,3) \right] p_{apparent}(d_1,i)$$

$$\cong \left. \frac{dN}{d\log d_{\mathrm{p,dry}}} \right|_{d_{\mathrm{p,dry}}=d_1} \bullet l(d_j) f(d_1,1) p_{\mathrm{true}}(d_1,i) + \left. \frac{dN}{d\log d_{\mathrm{p,dry}}} \right|_{d_{\mathrm{p,dry}}=d_2} \bullet l(d_j) f(d_2,2) p_{\mathrm{true}}(d_2,i)$$

$$+ \left. \frac{dN}{d\log d_{\mathrm{p,dry}}} \right|_{d_{\mathrm{p,dry}}=d_3} \bullet l(d_j) f(d_3,3) p_{\mathrm{true}}(d_3,i)$$

Here, d_j denotes the dry mobility diameters of $+j$ charged particles (j = 1, 2, 3) selected in DMA1. $dN/d\log d_{\mathrm{p,dry}}$ represents the number-size distribution of aerosol particles in the atmosphere and l (d_j) is the factor to correct for diffusion losses in the sampling line [*Mochida et al.*, 2010]. $f(d_j,j)$ are the number fractions of $+j$ charged particles (j = 1, 2, 3) [*Wiedensohler*, 1988; *TSI Incorporated*, 2006]. $p_{\mathrm{apparent}}(d_j, i)$ and $p_{\mathrm{true}}(d_j, i)$ respectively stand for the apparent (i.e., biased by the presence of multiply charged particles) and true probabilities of the presence of particles in the four ranges of g (numbered using i). In this calculation, the biases of g in Figure A1 were not considered. The presence of doubly and triply particles above 359 nm was not considered because of the absence of g distribution data. The d_j in $f(d_j,j)$ was replaced by the values in the nearest setting diameters used for size selection in DMA1. In addition, and $p_{\mathrm{true}}(d_2, i)$ and $p_{\mathrm{true}}(d_3, i)$ are approximated by $p_{\mathrm{apparent}}(d_2, i)$ and $p_{\mathrm{apparent}}(d_3, i)$ in equation, respectively, with replacement of d_j by the nearest setting diameters of DMA1. The calculated biases of g distributions by the presence of doubly and triply charged particles, $\{[p_{\mathrm{apparent}}(d_1, i)/p_{\mathrm{true}}(d_1, i)] - 1\}$ (Figure A1.3) at each dry diameter

from 24.1 to 359 nm are on average within the range from −3% to 24%. Finally, the biases of *g* distributions by the presence of multiply charged particles are regarded to small and the biases are acceptable for the analysis of model simulation of cloud droplet formation and growth.

The presence of multiply charged particles also biases CCN effective spectra from CCNC and CPC data because CCN activity of multiply charged particles tends to be higher than that of singly charged particles with the same electrical mobility. For the analysis of this study, CCN efficiency spectra for singly charged particles were calculated as follows. The fractions of multiply charged particles with specific $d_{p,dry}$ downstream of DMA2 are estimated from the SMPS-derived number-size distributions on the assumption that the fraction of multiply charged particles selected in DMA1 did not change by the further selection in DMA2. This assumption is consistent with the result that the differences of *g* of multiply charged particles from singly charged particles having the same mobility diameter (Figures A1a and A1b) are not large. $n_{CCN,DMA2}/n_{CN,DMA2}$ at each $d_{p,dry}$ was obtained by calculating the number fractions of doubly and triply charged particles based on the theoretical formulas [*Wiedensohler*, 1988; *TSI Incorporated*, 2006], and by subtracting the contribution of doubly and triply charged particles as CCN preferentially from raw $n_{CCN,DMA2}$ on the assumption that CCN activity of multiply charged particles is higher than that of singly charged particles. The contributions of doubly and triply charged particles were calculated based on 3h-average number-size distributions of aerosol particles in the atmosphere with considerations of the diffusion losses in the sampling line and the areas of the transfer functions of DMA1 [*Mochida et al.*, 2010].

This assumption is not entirely correct because all multiply charged particles are not necessarily CCN active as suggested from F_{max} less than unity. To evaluate the validity of the method explained above, $n_{CCN,DMA2}/n_{CN,DMA2}$ were corrected by considering $n_{CCN,DMA2}/n_{CN,DMA2}$ of doubly and triply charged particles (Figure A3). Here, the presence of doubly and triply particles above 359 nm in $n_{CCN,DMA2}$ were not considered because of the absence of data. In this method, the differences of the CCN activation diameters predicted based on g ($d_{act,g85}$) from those measured ($d_{act,CCN}$) were within 17% and 18–46%, respectively, for more and less hygroscopic particles. These values are similar to the corresponding values in section 5.3 (12% and 16–41%, respectively). Furthermore, the feature that $d_{act,CCN}$ tends to be smaller than $d_{act,g85}$ holds, although the number of the exceptional cases that $d_{act,CCN}$ is larger than $d_{act,g85}$ increases to three from one. The results obtained this method were not used for this study because some CCN efficiency spectra seem to be unrealistically scattered. This scattering might be associated in part with the uncertainties of $n_{CCN,DMA2}/n_{CN,DMA2}$ of multiply charged particles as a result of the temporal variation of CCN number concentrations during the dry diameter scans conducted using DMA1.

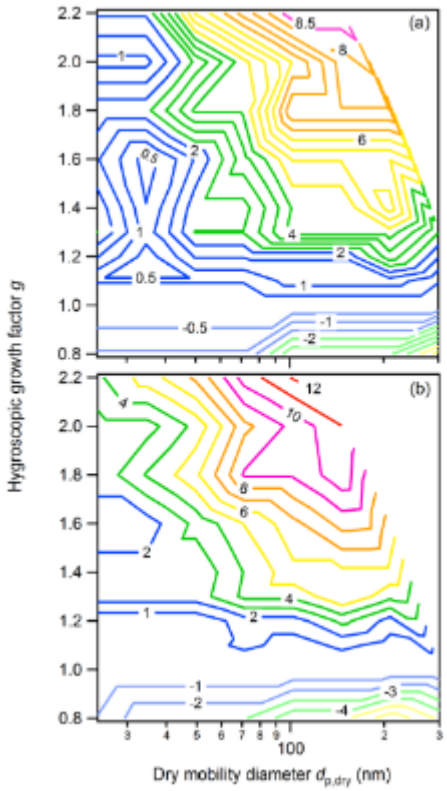

Figure A1. The differences of *g* of (a) doubly and (b) triply charged particles from those of singly charged particles with the same electrical mobility (in %). For multiply charged particles, the horizontal axis represents the dry mobility diameter ($d_{p,dry}$) of singly charged particles with the same mobility. The concept of the contour plots follows from *Duplissy et al.* [2009].

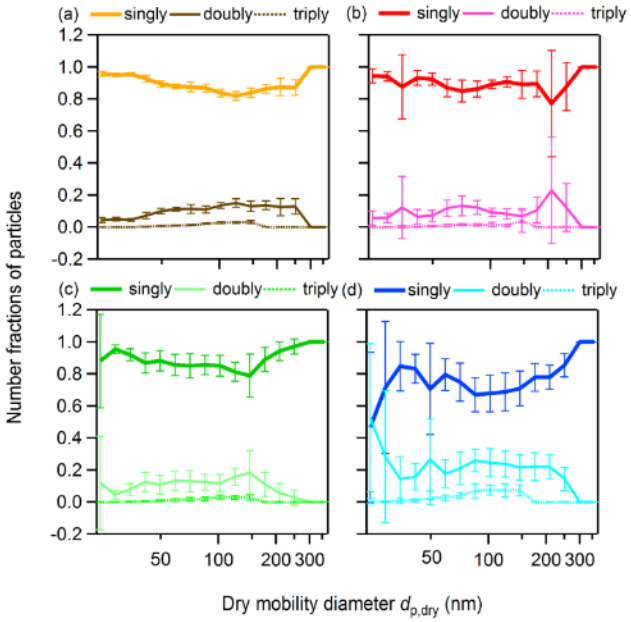

Figure A2. The estimated number fractions of singly, doubly, and triply charged particles among these particles in the ranges of (a) $0.8 \leq g < 1.1$, (b) $1.1 \leq g < 1.25$, (c) $1.25 \leq g < 1.4$, and (d) $1.4 \leq g \leq 2.2$. For doubly and triply charged particles, the horizontal axis represents the dry mobility diameter ($d_{p,dry}$) of singly charged particles with the same mobility.

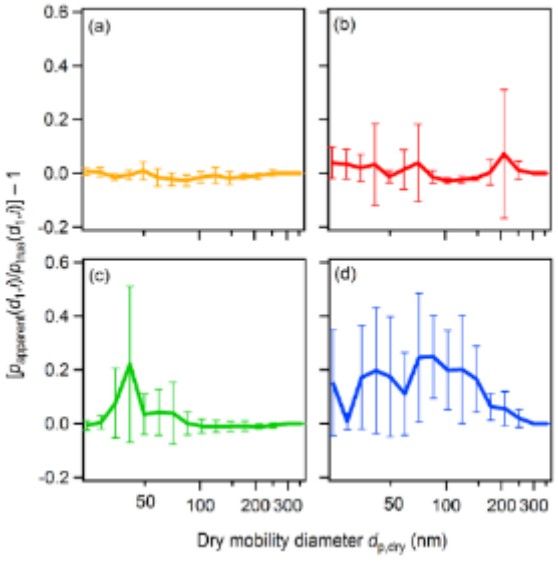

Figure A3. The estimated biases of the apparent probabilities of the presence of doubly and triply charged particles for particles in the ranges of (a) $0.8 \leq g < 1.1$, (b) $1.1 \leq g < 1.25$, (c) $1.25 \leq g < 1.4$, and (d) $1.4 \leq g \leq 2.2$.

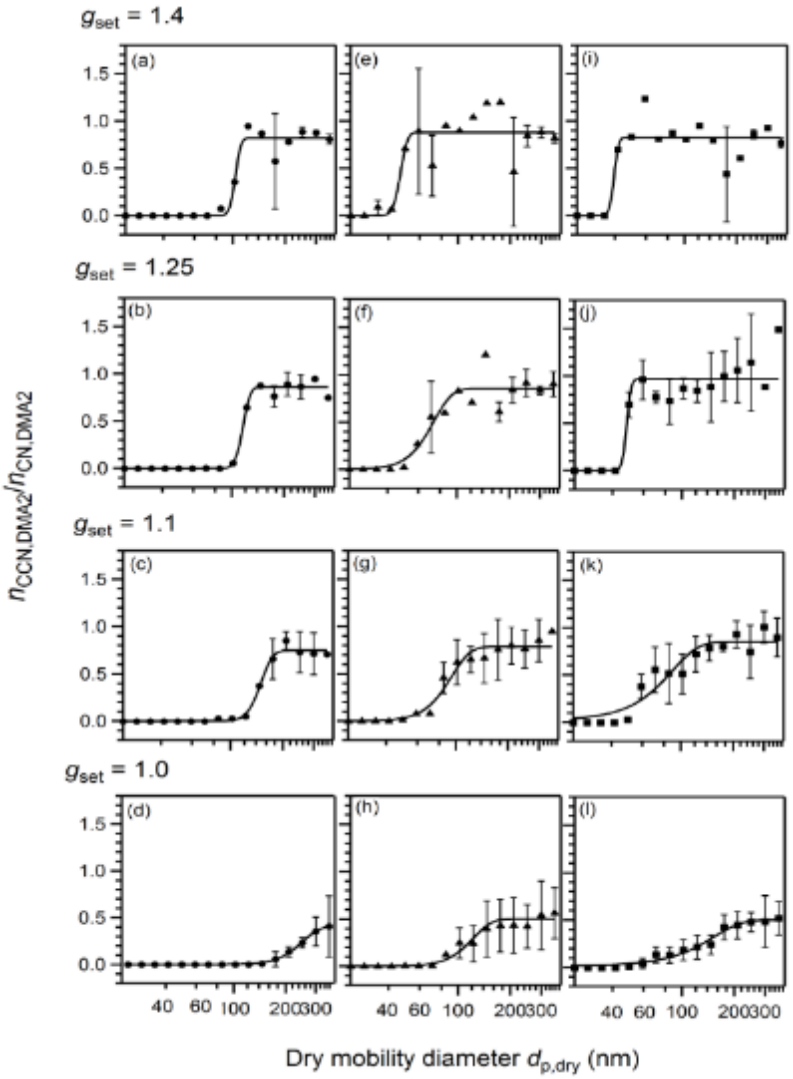

Figure A4. The averages of the measured CCN efficiency spectra (symbols) and the curves fitted to the averages (solid lines) for aerosol particles with g_{set} of (a, e, and i) 1.4, (b, f, and j) 1.25, (c, g, and k) 1.1, and (d, h, and l) 1.0 at (a–d) 0.18%, (e–h) 0.49%, and (i–l) 0.95% SS. The calculation is performed with consideration of $n_{CCN,DMA2}/n_{CN,DMA2}$ of doubly and triply charged particles sequentially from large to small diameters (see Appendix A1 for detail). The data points with negative values of $n_{CCN,DMA2}$ after correction of doubly and triply charged particles are omitted. Some data points are obtained from single samples as a result of the omissions. The standard deviation for data points from three or more samples are shown by bars.

6. Summary and Conclusions

To better understand the critical factors for CCN activation and the number concentrations of CCN and cloud droplets, and the reasons that lead to the differences of the prediction and the measurement of N_{CCN}, studies on the hygroscopicity and CCN activity of atmospheric aerosol particles were performed based on atmospheric observations at urban and forest sites. According to the results of the observation in Nagoya, 2009, the size-resolved g at 85% RH was on average characterized by bimodal distributions with less and more hygroscopic modes. The mean of g_m and κ_{HTDMA} for 24–359 nm particles were 1.27 and 0.22, respectively. The g_m and κ_{HTDMA} were relatively low in small particles and they were larger at larger diameters. The Aitken mode range was dominated by particles that had relatively low hygroscopicity ($0.8 \leq g < 1.25$) and were composed of freshly emitted organic compounds. Conversely, the accumulation mode range was dominated by particles that had relatively high hygroscopicity ($1.25 \leq g \leq 2.2$) and were composed of oxidized organic compounds and inorganic salts. The size-averaged κ_{org} and the range of size-resolved κ_{org} for 60–359 nm from the regression method were calculated to be 0.11 and 0.08–0.12, respectively. The mean of κ_{org} from all four size ranges and the mean from respective size ranges from the ZSR method were calculated to be 0.19 and 0.14–0.23, respectively. The κ_{org} correlated positively with f_{44} and O/C, yet their correlations were not high. The F_{act} at 0.12%, 0.24%, and 0.43% SS were >0.9 in most cases during the observation period, indicating low fractions of CCN-inactive particles at large diameters. The mean κ_{CCNC} calculated from d_{act} at 0.12%, 0.24%, and 0.43% SS were 0.32, 0.26, and 0.23, respectively, showing the size dependence that smaller particles had lower hygroscopicity, as κ_{HTDMA}. The κ_{CCNC} was ~37% higher than κ_{HTDMA} and the ~28% differences among ~37%

difference may be due to the effects of organics, in addition to the simplifications made for the calculations of κ_{HTDMA} and κ_{CCNC}, and possible co-condensation of semi volatile organics. In the CCN closure, predicted N_{CCN}/N_{CN} is largely underestimated (mean relative differences at three SS: −64% to −45%) if κ_{org} is assumed to be zero. Using size-averaged κ_{org} (0.11 and 0.19) obtained from *g*, predicted N_{CCN}/N_{CN} agreed better to the measured with the mean relative differences from −17% to −8% and those from −2% to +14%, respectively. This result suggests that water-soluble organics contributed to N_{CCN} substantially. The predicted N_{CCN}/N_{CN} agreed to the measured with the mean relative differences from −30% to +10% (RSD: 15%–17%) if a representative single *g* is considered. The better agreement was obtained if size- and time-resolved *g* or size- and time-resolved *g* distributions is considered (mean relative differences: −19% to −3%, RSD: 6%−10%). The result indicates the importance of the dependence of *g* on time and size to N_{CCN}. The remaining 15% difference of N_{CCN}/N_{CN} in the CCN closure can be explained solely by a surface tension reduction (10%–12%) or by a combination of a surface tension reduction and an enhanced solute effect. The results demonstrate that the hygroscopicity of organics and the variations of the hygroscopicity of particles with time and size affect CCN number concentrations in an urban area.

The atmospheric observation of aerosol particles at a forested site in Wakayama was conducted in 2010. In the case of forest aerosol particles, the *g* of particles was characterized by broad unimodal distributions. The size-resolved *g* distributions and CCN activation curves were influenced by the formation and growth of new particles, and exhibited a clear diurnal pattern on NPF event days. During 0900-2100 JST on NPF event days, an large number concentrations of less hygroscopicity particles with *g* of 1.1–1.2 appeared in the Aitken mode range. This *g* values were similar to those for pure

BSOA generated in laboratory studies (g~1.1). The result suggests that these particles with low g were associated with newly-formed BSOA. Furthermore, the number fraction of less hygroscopic particles was large (>50%) in the range of <180 nm and the mean g of particles in accumulation mode range decreased significantly. The differences of the values of κ_{HTDMA} or κ_{CCNC} in different time sections on NPF event days were clear: the mean values of κ_{HTDMA} and κ_{CCNC} were 30% lower during 0900-2100 JST and 15% higher during 2100-0900 JST, than those during same time sections on non-event days. The result indicates that the bursts of nanoparticles with fresh, less oxidized, and less hygroscopic newly-formed BSOA components contributed to the decrease of hygroscopicity of pre-existing large particles by the condensation. The low g_m observed in the daytime rapidly shifted to high g_m in the nighttime in both small and large particles. During 2100-0900 JST, lowest N_{CN} and largest fraction of more hygroscopic particles among four different time sections were observed. The large fraction of more hygroscopic particles and the increase of g_m both in small and large particles were possibly caused by the aging of particles by oxidation, the production of WSOM in the aqueous phase, and the inflow of maritime air in the large diameter. The CCN activity of particles on NPF event days also showed a clear diurnal pattern corresponding to the changes of the particle hygroscopicity. By contrast, on non-event days, g distributions and the values associated with CCN activity of particles, d_{act}, N_{CCN}, and N_{CCN}/N_{CN} did not show large differences throughout the day. The monotonous g distributions with more hygroscopic particles suggest the particles to be well-mixed, highly oxidized, and aged. The κ values under sub- and super-saturated conditions were compared during observation; κ_{HTDMA} and κ_{CCNC} agreed within 10% on average. The differences of κ_{HTDMA} and κ_{CCNC} were not so large, suggesting that the effects by organics or less

hygroscopic particles, i.e., surface tension reduction and the enhancement of solute effect, were small. The mean ± SD of κ_{HTDMA}, $\kappa_{CCNC,}$ and κ_{org} in the Aitken mode during 0900-2100 JST on NPF event days were 0.17±0.02, 0.17±0.04, and 0.13±0.06 (from κ_{HTDMA} and κ_{CCNC}), respectively. The κ_{org} values were similar to those reported in previous studies for aerosols in the boreal forest and rainforest sites and for laboratory-generated pure BSOA. In the CCN closure, predicted N_{CCN}/N_{CN} values agreed well to the measured if a single averaged g was applied (12% ± 6%, r~0.91). The result provides an evidence of BSOA formation in the Aitken mode range and hygroscopic growth of newly-formed particles, and suggests their contribution to CCN number concentrations.

Another observation of atmospheric aerosol particles in Nagoya was conducted in 2010. The CCN activity with g_{set} of 1.0, 1.1, 1.25, and 1.4 were investigated individually, to consider the relationship between the hygroscopic growth and the CCN activation. The CCN efficiency spectra of more hygroscopic particles with g_{set} of 1.25 and 1.4 were characterized by a steep curve around d_{act}, small $\sigma_{CCN}/d_{act,CCN}$ and large F_{max} values. Obtained results showed that the hygroscopicity of more hygroscopic particles at 85% RH linked well to the CCN activity. In contrast, CCN efficiency spectra of less hygroscopic particles with g_{set} of 1.0 and 1.1 were characterized by a curve with moderate steepness, large $\sigma_{CCN}/d_{act,CCN}$, and small F_{max} values. Results showed that some of the less hygroscopic particles remained CCN-inactive even in the case of high SS and large diameters. To investigate the relation between the hygroscopic growth and the CCN activation, CCN activation diameters predicted from the g distributions ($d_{act,g85}$) were compared with measured ($d_{act,CCN}$) for aerosol particles with different g_{set}. The $d_{act,CCN}$ were smaller than $d_{act,g85}$ with one exception, that is, the measured CCN

activity was higher than predicted. Although the differences of $d_{act,g85}$ from $d_{act,CCN}$ were on average within 12% for more hygroscopic particles, the differences were on average larger (16%–41%) for less hygroscopic particles. The possible causes of this difference include the surface tension reduction, the dependence of κ on the concentration of the aqueous solution, the existence of sparingly soluble particles, and asphericity of particles. Furthermore, the contribution of aerosol particles with different hygroscopicity to cloud droplet formation was investigated using the cloud parcel model. The presence of less hygroscopic particles in addition to more hygroscopic particles ($0.8 \leq g \leq 2.2$) led to 27% increase of N_{CCN}, 18% increase of N_{cd}, and the 5% decrease of R_{eff} at v of 1.0 m s^{-1}, as compared to the case that only more hygroscopic particles ($g \geq 1.25$) were present. These results suggested that the presence of less hygroscopic particles can contribute substantially to N_{CCN} and N_{cd} and can lead to smaller cloud droplets.

References

Abbatt, J. P. D., K. Broekhuizen, P. P. Kumar (2005), Cloud condensation nucleus activity of internally mixed ammonium sulfate/organic acid aerosol particles, *Atmos. Environ.,*39, 4767−4778, doi: 10.1016/j.atmosenv.2005.04.029.

Ahlm, L., S. Liu, D. A. Day, L. M. Russell, R. Weber, D. R. Gentner, A. H. Goldstein, J. P. DiGangi, S. B. Henry, F. N. keutsch, T. C. Vandenboer, M. Z. Markovic, J. G. Murphy, X. Ren, and S. Scheller (2012), Formation and growth of ultrafine particles from secondary sources in Bakersfield, California, *J. Geophys. Res*., 117, D00V08, doi:10.1029/2011JD017144.

Aikawa. M, T. Ohara, T. Hiraki, O. Oishi, A. Tsuji, M. Yamagami, K. Murano, and H. Mukai (2010), Significant geographic gradients in particulate sulfate over Japan determined from multiple-site measurements and a chemical transport model: Impacts of transboundary pollution from the Asian continent, *Atmos. Environ.,*44, 381−391, doi: 10.1016/j.atmosenv.2009.10.025.

Aiken, A. C., P. F. DeCarlo, and J. L. Jimenez (2007), Elemental analysis of organic species with electron ionization high-resolution mass spectrometry, *Anal. Chem.,* 79, 8350−8358, doi: 10.1021/ac071150w.

Aiken, A. C., P. F. DeCarlo, J. H. Kroll, D. R. Worsnop, J. A. Huffman, K. S. Docherty, I. M. Ulbrich, C. Mohr, J. R. Kimmel, D. Sueper, Y. Sun, Q. Zhang, A. Trimborn, M. Northway, P. J. Ziemann, M. R. Canagaratna, T. B. Onasch, M. R. Alfarra, A. S. H. Prévôt, J. Dommen, J. Duplissy, A. Metzger, U. Baltensperger, and J. L. Jimenez (2008), O/C and OM/OC ratios of primary, secondary, and ambient organic aerosols with high-resolution time-of-flight aerosol mass spectrometry, *Environ. Sci. Technol.,* 42, 4478-4485, doi:10.1021/es703009q.

Albrecht, B. A (1989), Aerosols, Cloud Microphysics, and Fractional Cloudiness, *Science*, 245, 1227−1230, doi: 10.1126/science.245.4923.1227.

Alfarra, M. R., N. Good, K. P. Wyche, J. F. Hamilton, P. S. Monks, A. C. Lewis, and G. McFiggans (2013), Water uptake is independent of the inferred composition of secondary aerosols derived from multiple biogenic VOCs, *Atmos. Chem. Phys*., 13, 11769−11789, doi:10.5194/acp-13-11769-2013.

Andreae, M. O. and D. Rosenfeld (2008), Aerosol-cloud-precipitation interations, Part 1. The nature and sources of cloud-active aerosols, *Earth Sci. Review,* 13-41.

Anttila, T., P. Vaattovaara, M. Komppula, A.-P. Hyvarinen, H. Lihavainen, V.-M. Kerminen, and A. Laaksonen (2009), Size-dependent activation of aerosols into cloud droplets at a subarctic background site during the second Pallas Cloud Experiment (2nd PaCE): method development and data evaluation, *Atmos. Chem. Phys*., 9, 4841−4854, doi:10.5194/acp-9-4841-2009.

Asa-Awuku, A., R. H. Moore, A. Nenes, R. Bahreini, J. S. Holloway, C. A. Brock, A. M. Middlebrook, T. B. Ryerson, J. L. Jimenez, P. F. DeCarlo, A. Hecobian, R. J. Weber, R. Stickel, D. J. Tanner, and L. G. Huey (2011), Airborne cloud condensation nuclei measurements during the 2006 Texas Air Quality Study, *J. Geophys. Res*., 116, D11201, doi:10.1029/2010JD014874.

Asmi, E., E. Freney, M. Hervo, D. Picard, C. Rose, A. Colomb, and K. Sellegri (2012), Aerosol cloud activation in summer and winter at puy-de-Dôme high altitude site in France, *Atmos. Chem. Phys*., 12, 11589−11607, doi:10.5194/acp-12-11589-2012.

Bilde, M.,B. Svennigson (2004), CCN activation of slightly soluble organics: the importance of small amounts of inorganic salt and particle phase, *Tellus*, 56B, 128−134.

Bougiatioti, A., C. Fountoukis, N. Kalivitis, S. N. Pandis, A. Nenes, and N. Mihalopoulos (2009), Cloud condensation nuclei measurements in the marine boundary layer of the eastern Mediterranean: CCN closure and droplet growth kinetics, *Atmos. Chem. Phys*., 9, 7053−7066, doi:10.5194/acp-9-7053-2009.

Bougiatioti, A., A. Nenes, C. Fountoukis, N. Kalivitis, S. N. Pandis, and N. Mihalopoulos (2011), Size-resolved CCN distributions and activation kinetics of aged continental and marine aerosol, *Atmos. Chem. Phys*., 11, 8791−8808, doi:10.5194/acp-11-8791-2011.

Boy, M., T. Petäjä, M. Dal Maso, Ü. Rannik, J. Rinne, P. Aalto, A. Laaksonen, P. Vaattovaara, J. Joutsensaari, T. Hoffmann, J. Warnke, M. Apostolaki, E. G. Stephanou, M. Tsapakis, A. Kouvarakis, C. Pio, A. Carvalho, A. Römpp, G. Moortgat, C. Spirig, A. Guenther, J. Greenberg, P. Ciccioli, and M. Kulmala (2004), Overview of the field measurement campaign in Hyytiälä, August 2001 in the framework of the EU project OSOA, *Atmos. Chem. Phys*., 4, 657−678, doi:10.5194/acp-4-657-2004.

Broekhuizen, K., P. P. Kumar, and J. P. D. Abbatt (2004), partially soluble organics as cloud condensation nuclei: Role of trace soluble and surface active species, *Geophys. Res. Lett.,* 31, D01107, doi:10.1029/2003GL018203.

Broekhuizen, K., R. Y. -W. Chang, W. R. Leaitch, S.-M. Li, and J. P. D. Abbatt (2006), Closure between measured and modeled cloud condensation nuclei (CCN) using size-resolved aerosol compositions in downtown Toronto, *Atmos. Chem. Phys*., 6, 2513−2524, doi:10.5194/acp-6-2513-2006.

Carrico, C. M., M. D. Petters, S. M. Kreidenweis, J. L. Collett Jr., G. Engling, and W. C. Malm (2008), Aerosol hygroscopicity and cloud droplet activation of extracts of filters from biomass burning experiments, *J. Geophys. Res*., 113, D08206, doi:10.1029/2007JD009274.

Cerully, K. M., T. Raatikainen, S. Lance, D. Tkacik, P. Tiitta, T. Petäjä, M. Ehn, M. Kulmala, D. R. Worsnop, A. Laaksonen, J. N. Smith, and A. Nenes (2011), Aerosol hygroscopicity and CCN activation kinetics in a boreal forest environment during the 2007 EUCAARI campaign, *Atmos. Chem. Phys*., 11, 12369−12386, doi:10.5194/acp-11-12369-2011.

Chang, R. Y. -W., P. S. K. Liu, W. R. Leaitch, and J. P. D. Abbatt (2007), Comparison between measured and predicted CCN concentrations at Egbert, Ontario: focus on the organic aerosol fraction at a semi-rural site, *Atmos. Environ.,*41, 8172−8182.

Chang, R. Y. -W., J. G. Slowik, N. C. Shantz, A. Vlasenko, J. Liggio, S. J. Sjostedt, W. R. Leaitch, and J. P. D. Abbatt (2010), The hygroscopicity parameter (κ) of ambient organic aerosol at a field site subject to biogenic and anthropogenic influences: relationship to degree of aerosol oxidation, *Atmos. Chem. Phys*., 10, 5047−5064, doi:10.5194/acp-10-5047-2010.

Chuang, P. Y (2003), Measurement of the timescale of hygroscopic growth for atmospheric aerosols, *J. Geophys. Res*., 108, D9, 4282, doi:10.1029/2002JD002757.

Clegg, S. L., P. Brimblecombe, and A. S. Wexler (1998), A thermodynamic model of the system $H^+ - NH_4^+ - SO_4^{2-} - NO_3^- - H_2O$ at tropospheric temperatures. *J. Phys. Chem. A*, 102, 2137−2154.

Cubison, M. J., B. Ervens, G. Feingold, K. S. Docherty, I. M. Ulbrich, L. Shields, K. Prather, S. Hering, and J. L. Jimenez (2008), The influence of chemical composition and mixing state of Los Angeles urban aerosol on CCN number and cloud properties,

Atmos. Chem. Phys., 8, 5649−5667, doi:10.5194/acp-8-5649-2008.

Decarlo, P. F., J. G. Slowik, D. R. Worsnop, P. Davidovits, and J. L. Jimenez (2004), Particle morphology and density characterization by combined mobility and aerodynamic diameter measurements, Part 1: Theory, *Aerosol. Sci. Technol.,* 38, 1185−1205, doi:10.1080/027868290903907.

Decarlo, P. F., J. R. Kimmel, A. Trimborn, M. J. Northway, J. T. Jayne, A. C. Aiken, M. Gonln, K. Fuhrer, T. Horvath, K. S. Docherty, D. R. Worsnop, and J. L. Jimenez (2006), Field-deployable, high-resolution, time-of-flight aerosol mass spectrometer, *Anal. Chem.,* 78, 24, 8281−8289.

Drexler, R. R., and G. D. Rolph (2003), HYSPLIT (HYbrid Single-Particle Lagrangian Integrated Trajectory) Model access via NOAA ARL READY Website (http://www.arl.noaa.gov/ready/hysplit4.html), NOAA Air Resources Laboratory, Silver Spring, MD, USA

Duplissy, J., M. Gysel, M. R. Alfarra, J. Dommen, A. Metzger, A. S. H. Prevot, E. Weingartner, A. Laaksonen, T. Raatikainen, N. Good, S. F. Turner, G. McFiggans, and U. Baltensperger (2008), Cloud forming potential of secondary organic aerosol under near atmospheric conditions, *Geophys. Res. Lett.,* 35, D03818, doi:10.1029/2007GL031075.

Duplissy, J., M. Gysel, S. Sjogren, N. Meyer, N. Good, L. Kammermann, V. Michaud, R. Weigel, S. Martins dos Santos, C. Gruening, P. Villani, P. Laj, K. Sellegri, A. Metzger, G. McFiggans, G. Wehrle, R. Richter, J. Dommen, Z. ristovski, U. Baltensperger, and E. Weingartner (2009), Intercomparison study of six HTDMAs: results and recommendations, *Atmos. Meas. Tech.,* 2, 363−378.

Duplissy, J., P. F. Decarlo, J. Dommen, M. R. Alfarra, A. Metzger, I. Barmpadimos, A. S. H. Prevot, E. Weingartner, T. Tritscher, M. Gysel, A. C. Aiken, J. L. Jimenez, M. R. Canagaratna, D. R. Worsnop, D. R. Collins, J. Tomlinson, and U. Baltensperger (2011), Relating hygroscopicity and composition of organic aerosol particulate matter, *Atmos. Chem. Phys*., 11, 1155−1165, doi:10.5194/acp-11-1155-2011.

Dusek, U., et al. (2006), Size matters more than chemistry for nucleating ability of aerosol particles, *Science*, 312, 1375−1378, doi:10.1126/science.1125261.

Dusek, U., G. P. Frank, J. Curtius, F. Drewnick, J. Schneider, A. Kürten, D. Rose, M. O. Andreae, S. Borrmann, and U. Pöschl (2010), Enhanced orgamic mass fraction and

decreased hygroscopicity of cloud condensation nuclei (CCN) during new particle fprmation events, *Geophys. Res. Lett.,* 37, L03804, doi:10.1029/2009GL040930.

Dusek, U., G. P. Frank, A. Massling, K. Zeromskiene, Y. Iinuma, O. Schmid, G. Halas, T. Hennig, A. Wiedensohler, and M. O. Andreae (2011), Water uptake by biomass burning aerosol at sub- and supersaturated conditions: closure studies and implications for the role of organics, *Atmos. Chem. Phys*., 11, 9519−9532, doi:10.5194/acp-11-9519-2011.

Dzepina, K., R. M. Volkamer, S. Madronich, P. Tulet, I. M. Ulbrich, Q. Zhang, C. D. Cappa, P. J. Ziemann, and J. L. Jimenez (2009), Evaluation of recently-proposed secondary organic aerosol models for a case study in Mexico City, *Atmos. Chem. Phys*., 9, 5681−5709, doi:10.5194/acp-9-5681-2009.

Ehn, M., T. Petäjä, H. Aufmhoff, P. Aalto, K. Hämeri, F. Arnold, A. Laaksonen, and M. Kulmala (2007), Hygroscopic properties of ultrafine aerosol particles in the boreal forest: diurnal variation, solubility and the influence of sulfuric acid, *Atmos. Chem. Phys*., 7, 211−222, doi:10.5194/acp-7-211-2007.

Engelhart, G. J., A. Asa-Awuku, A. Nenes, and S. N. Pandis (2008), CCN activity and droplet growth kinetics of fresh and aged monoterpene secondary organic aerosol, *Atmos. Chem. Phys*., 8, 3937−3949, doi:10.5194/acp-8-3937-2008.

Engelhart, G. J., R. H. Moore, A. Nenes, and S. N. Pandis (2011), Cloud condensation nuclei activity of isoprene secondary organic aerosol, *J. Geophys. Res.*, 116, doi:10.1029/2010JD014706.

Ervens, B., G. Feingold, G. J. Frost, and S. M. Kreidenweis (2004a), A modeling study of aqueous production of dicarboxylic acids: 1. Chemical pathways and speciated organic mass production, *J. Geophys. Res*., 109, D15205, doi:10.1029/2003JD004387.

Ervens, B., G. Feingold, G. J. Frost, and S. M. Kreidenweis (2004b), A modeling study of aqueous production of dicarboxylic acids: 2. Implications for cloud microphysics, *J. Geophys. Res*., 109, D15206, doi:10.1029/2004JD004575.

Ervens, B., M. Cubison, E. Andrews, G. Feingold, J. A. Ogren, J. L. Jimenez, P. DeCarlo, and A. Nenes (2007), Prediction of cloud condensation nucleus number concentration using measurements of aerosol size distributions and comparison and light scattering enhancement due to humidity, *J. Geophys. Res*., 112, D10S32,

doi:10.1029/2006JD007426.

Ervens, B., M. J. Cubison, E. Andrews, G. Feingold, J. A. Ogren, J. L. Jimenez, P. K. Quinn, T. S. Bates, J. Wang, Q. Zhang, H. Coe, M. Flynn, and J. D. Allan (2010), CCN predictions using simplified assumptions of organic aerosol composition and mixing state: a synthesis from six different locations, *Atmos. Chem. Phys*., 10, 4795−4807, doi:10.5194/acp-10-4795-2010.

Facchini, M. C., M. Mircea, S. Fuzzi, and R. J. Charlson (1999), Cloud albedo enhancement by surface-active organic solutes in growing droplets, *Nature*, 401, 257−259, doi:10.1038/45758.

Facchini, M. C., S. Decesari, M. Mircea, S. Fuzzi, G. Loglio (2000), Surface tension of atmospheric wet aerosol and cloud/fog droplets in relation to their organic carbon content and chemical composition, *Atmos. Environ.,*34, 4853−4857.

Fors, E. O., J. Rissler, M. Mircea, A. Massling, B. Svenningsson, M. O. Andreae, U. Dusek, G. P. Frank, A. Hoffer, M. Bilde, G. Kiss, S. Janitsek, S. Henning, M. C. Facchini, S. Decesari, and E. Swietlicki (2010), Hygroscopic properties of Amazonian biomass burning and European background HULIS and investigation of their effects on surface tension with two models linking H-TDMA to CCNC data, *Atmos. Chem. Phys*., 10, 5625−5639, doi:10.5194/acp-10-5625-2010.

Fors, E. O., E. Swietlicki, B. Svenningson, A. Kristensson, G. P. Frank, and M. Sporre (2011), Hygroscopic properties of the ambient aerosol in southern Sweden – a two year study, *Atmos. Chem. Phys*., 11, 8343−8361, doi:10.5194/acp-11-8343-2011.

Fountoukis, C., A. Nenes, N. meskhidze, R. Bahreini, W. C. Conant, H. Jonsson, S. Murphy, A. Sorooshian, V. Varutbangkul, F. Brechtel, R. C. Flagan, and J. H. Seinfeld (2007), Aerosol–cloud drop concentration closure for clouds sampled during the International Consortium for Atmospheric Research on Transport and Transformation 2004 campaign, *J. Geophys. Res*., 112, D10S30, doi:10.1029/2006JD007272.

Frosch, M., M. Bilde, A. Nenes, A. P. Praplan, Z. Jurányi, J. Dommen, M. Gysel, E. Weingartner, and U. Baltensperger (2013), CCN activity and volatility of *β*-caryophyllene secondary organic aerosol, *Atmos. Chem. Phys*., 13, 2283−2297, doi:10.5194/acp-13-2283-2013.

Gasparini, R., D. R. Collins, E. Andrews, P. J. Sheridan, J. A. Ogren, and J. G. Hudson (2006), Coupling aerosol size distributions and size-resolved hygroscopicity to predict humidity-dependent optical properties and cloud condensation nuclei spectra, *J. Geophys. Res*., 111, D05S13, doi:10.1029/2005JD006092.

Good, N., D. O. Topping, J. D. Allan, M. Flynn, E. Fuentes, M. Irwin, P. I. Williams, H. Coe, and G. McFiggans (2010a), Consistency between parameterizations of aerosol hygroscopicity and CCN activity during the RHaMBLe discovery cruise, *Atmos. Chem. Phys*., 10, 3189−3203, doi:10.5194/acp-10-3189-2010.

Good, N., D. O. Topping, J. Duplissy, M. Gysel, N. K. Meyer, A. Metzger, S. F. Turner, U. Baltensperger, Z. Ristovski, E. Weingartner, H. Coe, and G. McFiggans (2010b), Widening the gap between measurement and modelling of secondary organic aerosol properties?, *Atmos. Chem. Phys*., 10, 2577−2593, doi:10.5194/acp-10-2577-2010.

Gunthe, S. S., S. M. King, D. Rose, Q. Chen, P. Roldin, D. K. Farmer, J. L. Jimenez, P. Artaxo, M. O. Andreae, S. T. Martin, and U. Pöschl (2009), Cloud condensation nuclei in pristine tropical rainforest air of Amazonia: size-resolved measurements and modelling of atmospheric aerosol composition and CCN activity, *Atmos. Chem. Phys*., 9, 7551−7575, doi:10.5194/acp-9-7551-2009.

Gunthe, S. S., D. Rose, H. Su, R. M. Garland, P. Achtert, A. Nowak, A. Wiedensohler, M. Kuwata, N. Takegawa, Y. Kondo, M. Hu, M. Shao, T. Zhu, M. O. Andreae, and U. Pöschl (2011), Cloud condensation nuclei (CCN) from fresh and aged pollution in the megacity region of Beijing, *Atmos. Chem. Phys*., 11, 11023−11039, doi:10.5194/acp-11-11023-2011.

Gysel, M., G. B. McFiggans, and H. Coe (2009), Inversion of tandem differential mobility analyser (TDMA) measurements, *Aerosol Science,* 40, 134−151, doi:10.1016/j.jaerosci.2008.07.013.

Hallquist, M., J. C. Wenger, U. Baltensperger, Y. Rudich, D. Simpson, M. Claeys, J. Dommen, N. M. Donahue, C. George, A. H. Goldstein, J. F. Hamilton, H. Herrmann, T. Hoffmann, Y. Iinuma, M. Jang, M. E. Jenkin, J. L. Jimenez, A. Kiendler-Scharr, W. Maenhaut, G. McFiggans, Th. F. Mentel, A. Monod, A. S. H. Prévôt, J. H. Seinfeld, J. D. Surratt, R. Szmigielski, and J. Wildt (2009), The formation, properties and impact of secondary organic aerosol: current and emerging issues, *Atmos. Chem. Phys*., 9, 5155−5236, doi:10.5194/acp-9-5155-2009.

Hämeri, K., M. Väkevä, P. P. Aalto, M. Kulmala, E. Swietlicki, J. Zhou, W. Seidl, E. Becker, and C. D. O'dowd (2001), Hygroscopic and CCN properties of aerosol particles in boreal forests, *Tellus*, 53B, 359-379.

Han, Y., Y. Iwamoto, T. Nakayama, K. Kawamura, T. Hussein, and M. Mochida (2013), Observation of new particle formation over a mid-latitude forest facing the North Pacific, *Atmos. Environ.,* 64, 77-84.

Han, Y., Y. Iwamoto, T. Nakayama, K. Kawamura, and M. Mochida (2014), Formation and evolution of biogenic secondary organic aerosol over a forest site in Japan, *J. Geophys. Res.*, 119, 259-273, doi:10.1002/2013JD020390.

Hänel, G.(1976) The properties of atmospheric aerosol particles as functions of the relative humidity at thermodynamic equilibrium with the surrounding moist air, *Rev. Geophys*., 17, 73−188.

Henning, S., T. Rosenørn, B. D'Anna, A.A.Gola, B. Svenningsson, and M. Blide (2005), Cloud droplet activation and surface tension of mixtures of slightly soluble organics and inorganic salt, *Atmos. Chem. Phys*., 5, 575−582, doi:1680-7324/acp/2005-5-575.

Henze, D. K. and J. H. Seinfeld (2006), Global secondary organic aerosol from isoprene oxidation, *Geophys. Res. Lett.,* 33, L09812, doi:10.1029/2006GL025976.

Hersey, S. P., J. S. Craven, K. A. Schilling, A. R. Metcalf, A. Sorooshian, M. N. Chan, R. C. Flagan, and J. H. Seinfeld (2011), The Pasadena Aerosol Characterization (PACO): chemical and physical analysis of the western Los Angeles basin aerosol, *Atmos. Chem. Phys*., 11, 7417−7443, doi:10.5194/acp-11-7417-2011.

Hong, J., S. A. K. Häkkinen, M. Paramonov, M. Äijälä, J. Hakala, T. Nieminen, J. Mikkilä, N. L. Prisle, M. Kulmala, I. Riipinen, M. Bilde, V.-M. Kerminen, and T. Petäjä (2014), Hygroscopicity, CCN and volatility properties of submicron atmospheric aerosol in a boreal forest environment during the summer of 2010, *Atmos. Chem. Phys*., 14, 4733−4748, doi:10.5194/acp-14-4733-2014.

Huff Hartz, K. E., T. Rosenørn, S. R. Ferchak, T. M. Raymond, M. Bilde, N. M. Donahue, and S. N. Pandis (2005), Cloud condensation nuclei activation of monoterpene and sesquiterpene secondary organic aerosol, *J. Geophys. Res.*, 110, D14208, doi:10.1002/2004JD005754.

IPCC: Climate Change 2007: The Physical Science Basis, Fourth Assessment Report of the Intergovernmental Panel on Climate Change, edited by: Solomon, S., Qin, D., Manning, M., Chen, Z., Marquis, M., Averyt, K., Tignor, M., and Miller, H. L., *Cambridge Univ. Press*, Cambridge and New York, 2007.

IPCC: Climate Change 2013: The Physical Science Basis, Fifth Assessment Report of the Intergovernmental Panel on Climate Change, http://ipcc.ch.

Irwin, M., N. Good, J. Crosier, T. W. Choularton, and G. McFiggans (2010), Reconciliation of measurements of hygroscopic growth and critical supersaturation of aerosol particles in central Germany, *Atmos. Chem. Phys*., *10*, 11737−11752, doi:10.5194/acp-10-11737-2010.

Irwin, M., N. Robinson, J. D. Allan, H. Coe, and G. McFiggans (2011), Size-resolved aerosol water uptake and cloud condensation nuclei measurements as measured above a Southern Asian rainforest during OP3, *Atmos. Chem. Phys*., *11*, 11157−11174, doi:10.5194/acp-11-11157-2010.

Jimenez, J. L., et al. (2009), Evolution of Organic Aerosols in the Atmosphere, *Science*, 326, 1525−1529, doi: 10.1126/science.1180353.

Jung, J., Y. J. Kim, S. G. Aggarwal, and K. Kawamura (2011), Hygroscopic property of water-soluble organic-enriched aerosols in Ulaanbaatar, Mongolia during the cold winter of 2007, *Atmos. Environ.,* 45, 2722−2729.

Jung, J., Y. Miyazaki, and K. Kawamura (2013), Different characteristics of new particle formation between urban and deciduous forest sites in Northern Japan during the summers of 2010-2011, *Atmos. Chem. Phys*., *13*, 51−68, doi:10.5194/acp-13-51-2013.

Jurányi, Z., M. Gysel, E. Weingartner, P. F. DeCarlo, L. Kammermann, and U. Baltensperger (2010), Measured and modeled cloud condensation nuclei number concentration at the high alpine site Jungfraujoch, *Atmos. Chem. Phys*., *10*, 7891−7906, doi:10.5194/acp-10-7891-2010.

Jurányi, Z., T. Tritscher, M. Gysel, M. Laborde, L. Gomes, G. Roberts, U. Baltensperger, and E. Weingartner (2013), Hygroscopic mixing state of urban aerosol derived from size-resolved cloud condensation nuclei measurements during the MEGAPOLI campaign in Paris, *Atmos. Chem. Phys*., *13*, 6431−6446, doi:10.5194/acp-13-6431-2013.

Kammermann, L., M. Gysel, E. Weingartner, H. Herich, D. J. Cziczo, T. Holst, B. Svenningsson, A. Arneth, and U. Baltensperger (2010), Subarctic atmospheric aerosol composition: 3. Measured and modeled properties of cloud condensation nuclei, *J. Geophys. Res.*, 115, D04202, doi:10.1029/2009JD012447.

Kanakidou, M., J. H. Seinfeld, S. N. Pandis, I. Barnes, F. J. Dentener, M. C. Facchini, R. Van Dingenen, B. Ervens, A. Nenes, C. J. Nielsen, E. Swietlicki, J. P. Putaud, Y. Balkanski, S. Fuzzi, J. Horth, G. K. Moortgat, R. Winterhalter, C. E. L. Muhre, K. Tsigaridis, E. Vignati, E. G. Stephanou, and J. Wilson (2005), Organic aerosol and global climate modelling: a review, *Atmos. Chem. Phys*., *5*, 1053−1123, doi:10.5194/acp-5-1053-2005.

Kawana, K. N. Kuba, and M. Mochida (2014), Assessment of cloud condensation nucleus activation of urban aerosol particles with different hygroscopicity and the application to the cloud parcel model, *J. Geophys. Res.*, 119, 3352−3371, doi:10.1002/2013JD020827.

Kim, J. H., S. S. Yum, S. Shim, S.-C. Yoon, J. G. Hudson, J. Park, and S.-J. Lee (2011), On aerosol hygroscopicity, cloud condensation nuclei (CCN) spectra and critical supersaturation measured at two remote islands of Korea between 2006 and 2009, *Atmos. Chem. Phys*., *11*, 12627−12645, doi:10.5194/acp-11-12627-2011.

King, S. M., T. Rosenoern, J. E. Shilling, Q. Chen, and S. T. Martin (2009), Increased cloud activation potential of secondary organic aerosol for atmospheric mass loading, *Atmos. Chem. Phys*., *9*, 2959−2971, doi:10.5194/acp-9-2959-2009.

Kiss. G., E. Tombácz, and H-C. Hansson (2005), Surface tension effects of humic-like substances in the aqueous extract of tropospheric fine aerosol, *J. Atmos. Chem*., 50, 279−294, doi:10.1007/s10874-005-5079-5.

Kondo, Y., Y. Miyazaki, N. Takegawa, T. Miyakawa, R. J. Weber, J. L. Jimenez, Q. Zhang, and D. R. Worsnop (2007), Oxygenated and water-soluble organic aerosols in Tokyo, *J. Geophys. Res*., 112, D01203 doi:10.1029/2006JD007056.

Kreidenweis, S. M., M. D. Petters., and P. J. DeMott (2008), Single-parameter estimates of aerosol water content, *Environ. Res. Lett*., 3, 2008, 035002, doi:10.1088/1748-9326/3/3/035002.

Kristensen, T. B., H. Wex, B. Nakat, J. K. Nøjgaard, D. van Pinxteren, D. H. Lowenthal, L. R. Mazzoleni, K. Dieckmann, C. B. Koch, T. F. Mentel, H. Herrmann, A. G.

Hallar, F. Stratmann, and M. Bilde (2012), Hygroscopic growth and CCN activity of HULIS from different environments, *J. Geophys. Res*., 117, D22203 doi:10.1029/2012JD018249.

Kuba, N., and T. Takeda (1983), Numerical study of the effect of CCN on the size distribution of cloud droplets, Part Ⅱ: Formation of large droplets, *J. Meteor. Soc. Japan.*, 61, 375−387.

Kuba, N., H. Iwabuchi, K. Maruyama, T. Hayasaka, T. Takeda, and Y. Fujiyoshi (2003), Parameterization of the Effect of Cloud Condensation Nuclei on Optical Properties of a Non-precipitating Water Layer Cloud, *J. Meteor. Soc. Japan.*, 81, 2, 393−414.

Kulmala, M., K. Hämeri, P. P. Aalto, J. M. Mäkelä, L. Pirjola, E. D. Nilsson, G. Buzorius, Ü. Rannik, M. Dal Maso, W. Seidl, T. Hoffmann, R. Janson, H.-C. Hansson, Y. Vllsanen, A. Laaksonen, and C. D. O'dowd (2001), Overview of the international project on biogenic aerosol formation in the boreal forest (BIOFOR), *Tellus*, 53B, 324−343.

Kulmala, M., T. Suni, K. E. J. Lehtinen, M. Dal Maso, M. Boy, A. Reissell, Ü. Rannik, P. Aalto, P. Keronen, H. Hakola, J. Bäck, T. Hoffmann, T. Vesala, and P. Hari (2004), A new feedback mechanism linking forests, aeerosols, and climate, *Atmos. Chem. Phys*., *4*, 557−562, doi:10.5194/acp-4-557-2004.

Kuwata, M., Y. Kondo, Y. Miyazaki, Y. Komazaki, H. H. Kim, S. S. Yum, H. Tanimoto, and H. Matsueda (2008), Cloud condensation nuclei activity at Jeju Island, Korea in spring 2005, *Atmos. Chem. Phys*., 8, 2933−2948, doi:10.5194/acp-8-2933-2008.

Kuwata, M., and Y. Kondo (2008), Dependence of size-resolved CCN spectra on the mixing state of nonvolatile cores observed in Tokyo, *J. Geophys. Res.*, 113, D19202, doi:10.1029/2007JD009761.

Lance, S., A. Nenes, and T. A. Rissman (2004), Chemical and dynamical effects on cloud droplet number: Implications for estimates of the aerosol indirect effect, *J. Geophys. Res.*, 109, D22208, doi:10.1029/2004JD004596.

Lance, S., J. Medina, J. N. Smith, and A. Nenes (2006), Mapping the operation of the DMT continuous flow CCN counter, *Aero. Sci. Technol.*, 40, 242-254, doi:10.1080/02786820500543290.

Lance, S., A. Nenes, C. Mazzoleni, M. K. Dubey, H. Gates, V. Varutbangkul, T. A.

Rissman, S. M. Murphy, A. Sorooshian, R. C. Flagan, J. H. Seinfeld, G. Feingold, and H. H. Jonsson (2009), Cloud condensation nuclei activity, closure, and droplet growth kinetics of Houston aerosol during the Gulf of Mexico Atmospheric Comparison and Climate Study (GoMACCS), *J. Geophys. Res.*, 114, D00F15, doi:10.1029/2008JD011699.

Lang-Yona, N., Y. Rudich, Th. F. Mentel, A. Buchholz, A. Kiendler-Scharr, E. Kleist, C. Spindler, R. Tillmann, and J. Wildt (2010), The chemical and microphysical properties of secondary organic aerosols from Holm Oak emissions, *Atmos. Chem. Phys*., *10*, 7253−7265, doi:10.5194/acp-10-7253-2010.

Lathem, T. L., A. J. Beyersdorf, K. L. Thornhill, E. L. Winstead, M. J. Cubison, A. Hecobian, J. L. Jimenez, R. J. Weber, B. E. Anderson, and A. Nenes (2013), Analysis of CCN activity of Arctic aerosol and Canadian biomass burning during summer 2008, *Atmos. Chem. Phys*., 13, 2735−2756, doi:10.5194/acp-13-2735-2013.

Leaitch, W. R., U. Lohmann, L. M. Russell, T. Garrett, N. C. Shantz, D. Toom-Sauntry, J. W. Strapp, K. L. Hayden, J. Marshall, M. Wolde, D. R. Worsnop, and J. T. Jayne (2010), Cloud albedo increase from carbonaceous aerosol, *Atmos. Chem. Phys*., 10, 7669−7684, doi:10.5194/acp-10-7669-2010.

Levin, E. J. T., A. J. Prenni, M. D. Petters, S. M. Kreidenweis, R. C. Sullivan, S. A. Atwood, J. Ortega, P. J. Demott, and J. N. Smith (2012), An annual cycle of size-resolved aerosol hygroscopicity at a forested site in Colorado, *J. Geophys. Res*., 117, D06201, doi:10.1029/2011JD016854.

Levin, E. J. T., A. J. Prenni, B. B. Palm, D. A. Day, P. Camouzano-Jost, P. M. Winkler, S. M. Kreidenweis, P. J. Demott, J. L. Jimenez, and J. N. Smith (2014), Size-resolved aerosol composition and its link to hygroscopicity at a forested site in Colorado, *Atmos. Chem. Phys*., *14*, 2657−2667, doi:10.5194/acp-14-2657-2014.

Liu, X., and J. Wang (2010), How important is organic aerosol hygroscopicity to aerosol indirect forcing?, *Environ. Res. Lett*., 5, 2010, 044010, doi:10.1088/1748-9326/5/4/044010.

Makkonen, R., A. Asmi, H. Korhonen, H. Kokkola, S. Järvenoja, P. Päisänen, K. E. J. Lehtinen, A. Laaksonen, V. –M. Kerminen, H. Järvinen, U. Lohmann, R. Bennartz, J. Feichter, and M. Kulmala (2009), Sensitivity of aerosol concentrations and cloud properties to nucleation and secondary organic distribution in ECHAMS5-HAM

global circulation model, *Atmos. Chem. Phys*., *9*, 1747−1766, doi:10.5194/acp-9-1747-2009.

Martin, S. T., M. O. Andreae, D. Althausen, P. Artaxo, H. Baars, S. Borrmann, Q. Chen, D. K. Farmer, A. Guenther, S. S. Gunthe, J. L. Jimenez, T. Karl, K. Longo, A. Manzi, T. Müller, T. Pauliquevis, M. D. Petters, A. J. Prenni, U. Pöschl, L. V. Rizzo, J. Schneider, J. N. Smith, E. Swietlicki, J. Tota, J. Wang, A. Wiedensohler, and S. R. Zorn (2010), An overview of the Amazonian Aerosol Characterization Experiment 2008 (AMAZE-08, *Atmos. Chem. Phys*., *10*, 11415−11438, doi:10.5194/acp-10-11415-2010.

Martin, M., R. Y.-W. Chang, B. Sierau, S. Sjogren, E. Swietlicki, J. P. D. Abbatt, C. Lesk, and U. Lohmann (2011), Cloud condensation nuclei closure study on summer arctic aerosol, *Atmos. Chem. Phys*., 11, 11335−11350, doi:10.5194/acp-11-11335-2011.

Massling, A., M. Stock, B. Wehner, Z. J. Wu, M. Hu, E. Brüggemann, T. Gnauk, H. Herrmann, and A. Wiedensohler (2009), Size segregated water uptake of the urban submicrometer aerosol in Beijing, *Atmos. Environ.,* 43, 1578−1589.

Massoli, P., A. T. Lambe, A. T. Ahern, L. R. Williams, M. Ehn, J. Mikkilä, M. R. Canagaratna, W. H. Brune, T. B. Onasch, J. T. Janye, T. Petäjä, M. Kulmala, A. Laaksonen, C. E. Kolb, P. Davidovits, and D. R. Worsnop (2010), Relationship between aerosol oxidation level and hygroscopic properties of laboratory generated secondary organic aerosol (SOA) particles, *Geophys. Res. Lett.,* 37, L24801, doi:10.1029/2010GL045258.

McFiggans, G., P. Artaxo, U. Baltensperger, H. Coe, M. C. Facchini, G. Feingold, S. Fuzzi, M. Gysel, A. Laaksonen, U. Lohmann, T. F. Mentel, D. M. Murphy, C. D. O'Dowd, J. R. Snider, and E. Weingartner (2006), The effect of physical and chemical aerosol properties on warm cloud droplet activation, *Atmos. Chem. Phys*., 6, 2593−2649, doi:10.5194/acp-6-2593-2006.

McMeeking, G. R., N. Good, M. D. Petters, G. McFiggans, and H. Coe (2011), Influences on the fraction of hydrophobic and hydrophilic black carbon in the atmosphere, *Atmos. Chem. Phys*., 11, 5099−5112, doi:10.5194/acp-11-5099-2011.

Medina, J., A. Nenes, R-E. P. Sotiropoulou, L. D. Cottrell, L. D. Ziemba, P. J. Beckman, and R. J. Griffin (2007), Cloud condensation nuclei closure during the international

consortium for atmospheric research on transport and transformation 2004 campaign: effects of size-resolved composition, *J. Geophys. Res*., 112, D10S31, doi:10.1029/2006JD007588.

Mei, F., A. Setyan, Q. Zhang, and J. Wang (2013a), CCN activity of organic aerosols observed downwind of urban emissions during CARES, *Atmos. Chem. Phys*., 13, 12155−12169, doi:10.5194/acp-13-12155-2013.

Mei, F., P. L. Hayes, A. Ortega, J. W. Taylor, J. D. Allan, J. Gilman, W. Kuster, J. de Gouw, J. L. Jimenez, and J. Wang (2013b), Droplet activation properties of organic aerosols observed at an urban site during CalNex-LA, *J. Geophys. Res*., 118, 2903−2917, doi:10.1002/jgrd.50285.

Menon, S., et al.(2002), Climate effects of black carbon aerosols in China and India, *Science*, 297, 2250−2253.

Merikanto, J., D. V. Spracklen, G. W. Mann, S. J. Pickering, and K. S. Carslaw (2009), Impact of nucleation on global CCN, *Atmos. Chem. Phys*., *9*, 8601−8616, doi:10.5194/acp-9-8601-2009.

Mircea, M., M. C. Facchini, S. Decesari, F. Cavalli, L. Emblico, S. Fuzzi, A. Vestin, J. Rissler, E. Swietlicki, G. Frank, M. O. Andreae, W. Maenhaut, Y. Rudich, and P. Artaxo (2005), Importance of the organic aerosol frcation for modeling aerosol hygroscopic growth and activation: a case study in the Amazon Basin, *Atmos. Chem. Phys*., *5*, 3111−3126, doi:10.5194/acp-5-3111-2005.

Miyazaki, Y., J. Jung, P. Fu, Y. Mizoguchi, K. Yamanoi, and K. Kawamura (2012a), Evidence of formation of submicrometer water-soluble organic aerosols at a deciduous forest site in northern Japan in summer, *J. Geophys. Res*., 117, D19213, doi:10.1029/2012JD018250.

Miyazaki, Y., J. Jung, P. Fu, Y. Mizoguchi, K. Yamanoi, and K. Kawamura (2012b), Seasonal variations of stable carbon isotopic composition and biogenic tracer compounds of water-soluble organic aerosols in a deciduous forest, *Atmos. Chem. Phys*., 12, 1367−1376, doi:10.5194/acp-12-1367-2012.

Mochida, M. and K. Kawamura (2004), Hygroscopic properties of levoglucosan and related organic compounds characteristic to biomass burning aerosol particles, *J. Geophys. Res*., 109, D21202, doi:10.1029/2004JD004962.

Mochida, M., T. Miyakawa, N. Takegawa, Y. Morino, K. Kawamura, and Y. Kondo

(2008), Significant alteration in the hygroscopic properties of urban aerosol particles by the secondary formation of organics, *Geophys. Res. Lett.,* 35, L02804, doi:10.1029/2007GL031310.

Mochida, M., C. Nishita-Hara, Y. Kitamori, S. G. Aggarwal, K. Kawamura, K. Miura, and A. Takami (2010), Size-segregated measurements of cloud condensation nucleus activity and hygroscopic growth for aerosols at Cape Hedo, Japan, in spring 2008, *J. Geophys. Res*., 115, D21207, doi:10.1029/2009JD013216.

Mochida, M., C. Nishita-Hara, H. Furutani, Y. Miyazaki, J. Jung, K. Kawamura, and M. Uematsu (2011), Hygroscopicity and cloud condensation nucleus activity of marine aerosol particles over the western North Pacific, *J. Geophys. Res*., 116, D06204, doi:10.1029/2010JD014759.

Moore, R. H., R. Bahreini, C. A. Brock, K. D. Froyd, J. Cozic, J. S. Holloway, A. M. Middlebrook, D. M. Murphy, and A. Nenes (2011), Hygroscopicity and composition of Alaskan Arctic CCN during April 2008, *Atmos. Chem. Phys*., 11, 11807−11825, doi:10.5194/acp-11-11807-2011.

Moore, R. H., K. Cerully, R. Bahreini, C. A. Brock, A. M. Middlebrook, and A. Nenes (2012), Hygroscopicity and composition of California CCN during summer 2010, *J. Geophys. Res*., 117, D00V12, doi:10.1029/2010JD017352.

Nakayama, T., Y. Ikeda, Y. Sawada, Y. Setoguchi, S. Ogawa, K. Kawana, M. Mochida, F. Ikemori, K. Matsumoto, and Y. Matsumi (2014), Properties of light-absorbing aerosols in the Nagoya urban area, Japan, in August 2011 and January 2012: Contributions of brown carbon and lensing effect, *J. Geophys. Res*., 119, doi:10.1002/2014JD021744.

Nenes, A., S. Ghan, H. Abdul-Razzak, P. Y. Chuang, and J. H. Seinfeld (2001), Kinetic limitations on cloud droplet formation and impact on cloud albedo, *Tellus*, 53B, 133−149.

Ng, N. L., M. R. Canagaratna, Q. Zhang, J. L. Jimenez, J. Tian, I. M. Ulbrich, J. H, Kroll, K. S. Docherty, P. S. Chhabra, R. Bahreini, S. M. Murphy, J. H. Seinfeld, L. Hildebrandt, N. M. Donahue, P. F. DeCarlo, V. A. Lanz, A. S. H. Prévôt, E. Dinar, Y. Rudich, and D. R. Worsnop (2010), Organic aerosol components observed in Northern Hemispheric datasets from aerosol mass spectrometer, *Atmos. Chem. Phys*., 10, 4625−4641, doi:10.5194/acp-10-4625-2010.

Ng, N. L., M. R. Canagaratna, J. L. Jimenez, P. S. Chhabra, J. H. Seinfeld, and D. R. Worsnop (2011), Changes in organic aerosol composition with aging inferred from aerosol mass spectra, *Atmos. Chem. Phys*., 11, 6465−6474, doi:10.5194/acp-11-6465-2011.

Padró, L.T., D. Tkacik, T. Lathem, C. J. Hennigan, A. P. Sullivan, R. J. Weber, L. G. Huey, and A. Nenes (2010), Investigation of cloud condensation nuclei properties and droplet growth kinetics of the water-soluble aerosol fraction in Mexico City, *J. Geophys.Res*., 115, D09204, doi:10.1029/2009JD013915.

Padró, L. T., R. H. Moore, X. Zhang, N. Rastogi, R. J. Weber, and A. Nenes (2012), Mixing state and compositional effects on CCN activity and droplet growth kinetics of size-resolved CCN in an urban environment, *Atmos. Chem. Phys*., 12, 10239−10255, doi:10.5194/acp-12-10239-2012.

Pang, Y., B. J. Turpin, and L. A. Gundel (2006), On the importance of organic oxygen for understanding organic aerosol particles, *Aerosol. Sci. Technol*., 40, 128−133, doi:10.1080/02786820500423790.

Petters, M. D., A. J. Prenni, S. M. Kreidenweis, P. J. Demott, A. Matsunaga, Y. B. Lim, and P. J. Ziemann (2006), Chemical aging and the hydrophobic-to-hydrophilic conversion of carbonaceous aerosol, *Geophys. Res. Lett.,* 33, L24806, doi:10.1029/2006GL027249.

Petters, M. D., and S. M. Kreidenweis (2007), A single parameter representation of hygroscopic growth and cloud condensation nucleus activity, *Atmos. Chem. Phys*., 7, 1961−1971, doi:10.5194/acp-7-1961-2007.

Pierce, J, R., K. Chen, and P. J. Adams (2007), Contribution of primary carbonaceous aerosol to cloud condensation nuclei: processes and uncertainties evaluated with a global aerosol microphysics model, *Atmos. Chem. Phys*., 7, 5447−5466, doi:10.5194/acp-7-5447-2007.

Pierce, J, R., W. R. Leaitch, J. Liggio, D. M. Westervelt, C. D. Wainwright, J. P. D. Abbatt, L. Ahlm, W. Al-Basheer, D. J. Cziczo, K. L. Hayden, A. K. Y. Lee, S.-M. Li, L. M. Russell, S. J. Sjpstedt, K. B. Strawbridge, M. Travis, A. Vlasenko, J. J. B. Wentzell, H. A. Wiebe, J. P. S. Wong, and A. M. Macdonald (2012), Nucleation and condensation growth to CCN sizes during a sustained pristine biogenic SOA event in a forested mountain valley, *Atmos. Chem. Phys*., 12, 3147−3163, doi:10.5194/acp-12-

3147-2012.

Pöschl. U. et al. (2010), Rainforest Aerosols as Biogenoc Nuclei of Clouds and Precipitation in the Amazon, *Science*, 329, 1513−1516.

Prenni, A. J., M. D. Petters, S. M. Kreidenweis, P. J. DeMott, and P. J. Ziemann (2007), Cloud droplet activation of secondary organic aerosol, *J. Geophys. Res*., 112, D10223, doi:10.1029/2006JD007963.

Pringle, K. J., H. Tost, A. Pozzer, U. Pöschl, and J. Lelieveld (2010), Global distribution of the effective aerosol hygroscopicity parameter for CCN activation, *Atmos. Chem. Phys*., 10, 5241−5255, doi:10.5194/acp-10-5241-2010.

Quinn, P. K., T. S. Bates, D. J. Coffman, and D. S. Covert (2008), Influence of particle size and chemistry on the cloud nucleating properties of aerosols, *Atmos. Chem. Phys*., 8, 1029−1042, doi:10.5194/acp-8-1029-2008.

Rader, D. J. and P. H. McMurry (1986), Application of the tandem differential mobility analyzer to studies of droplet growth or evaporation, *J. Aerosol. Sci.,* 17, 5, 771−787.

Ramanathan, V., P. J. Crutzen, J. T. Kiehl, and D. Rosenfeld (2001), Aerosol, climate, and the hydrological cycle, *Science*, 294, 2119−2124.

Reddington, C. L., G. McMeeking, G. W. Mann, H. Coe, M. G. Frontoso, D. Liu, M. Flynn, D. V. Spracklen, and K. S. Carslaw (2013), The mass and number size distributions of black carbon aerosol over Europe, *Atmos. Chem. Phys.*, 13, 4917−4939, doi:10.5194/acp-13-4917-2013.

Riipinen, I., J. R. Pierce, T. Yli-Juuti, T. Nieminen, S. Häkkinen, M. Ehn, H. Junninen, K. Lehtipalo, T. Petäjä, J. Slowik, R. Chang, N. C. Shantz, J. Abbatt, W. R. Leaitch, V.-M. Kerminen, D. R. Worsnop, S. N. Pandis, N. M. Donahue, and M. Kulmala (2011), Organic condensation: a vital link connecting aerosol formation to cloud condensation nuclei (CCN) concentrations, *Atmos. Chem. Phys.*, 11, 3865−3878, doi:10.5194/acp-11-3865-2011.

Rissler, J., E. Swietlicki, J. Zhou, G. Roberts, M. O. Andreae, L. V. Gatti, and P. Artaxo (2004), Physical properties of the sub-micrometer aerosol over the Amazon rain forest during the wet-to-dry season transition-comparison of modeled and measured CCN concentrations, *Atmos. Chem. Phys.*, 4, 2119−2143, doi:10.5194/acp-4-2119-2004.

Roberts, G., and A. Nenes (2005), A continuous-flow streamwise thermal-gradient CCN chamber for airborne measurements, *Aerosol. Sci. Technol*., 39, 206−221.

Rose, D., S. S. Gunthe, E. Mikhailov, G. P. Frank, U. Dusek, M. O. Andreae, and U. Pöschl (2008), Calibration and measurement uncertainties of a continuous-flow cloud condensation nuclei counter(DMT-CCNC): CCN activation of ammonium sulfate and sodium chloride aerosol particles in theory and experiment, *Atmos. Chem. Phys*., 8, 1153−1179, doi:10.5194/acp-8-1153-2008.

Rose, D., A. Nowak, P. Achtert, A. Wiedensohler, M. Hu, M. Shao, Y. Zhang, M. O. Andreae, and U. Pöschl (2010), Cloud condensation nuclei in polluted air and biomass burning smoke near the mega-city Guangzhou, China – Part 1: Size-resolved measurements and implications for the modeling of aerosol particle hygroscopicity and CCN activity, *Atmos. Chem. Phys*., 10, 3365-3383, doi:10.5194/acp-10-3365-2010.

Rose, D., S. S. Gunthe, H. Su, R. M. Garland, H. Yang, M. Berghof, Y. F. Cheng, B. Wehner, P. Achtert, A. Nowak, A. Wiedensohler, N. Takegawa, Y. Kondo, M. Hu, Y. Zhang, M. O. Andreae, and U. Pöschl (2011), Cloud condensation nuclei in polluted air and biomass burning smoke near the mega-city Guangzhou, China – Part 2: Size-resolved aerosol chemical composition, diurnal cycles, and externally mixed weakly CCN-active soot particles, *Atmos. Chem. Phys*., 11, 2817-2836, doi:10.5194/acp-11-2817-2011.

Rosenfeld, D (1999), TRMM observed first direct evidence of smoke from forest fires inhibiting rainfall, *Geophys. Res. Lett.,* 26, 20, 3105−3108.

Rosenfeld, D (2000), Suppression of rain and snow by the urban and industrial air pollution, *Science*, 287, 1793−1796, 2000.

Ruetter, P., H. Su, J. Trentmann, M. Simmel, D. Rose, S. S. Gunthe, H. Wernli, M. O. Andreae, and U.Pöschl (2009), Aerosol– and updraft–limited regimes of cloud droplet formation: influence particle number, size and hygroscopicity on the activation of cloud condensation nuclei (CCN), *Atmos. Chem. Phys*., 9, 7067−7080, doi:10.5194/acp-9-7067-2009.

Salma, I., T. Borsós, T. Weidinger, P. Aalto, T. Hussein, M. Dal Maso, and M. Kulmala (2011), Production, growth and properties of ultrafine atmospheric aerosol particles in an urban environment, *Atmos. Chem. Phys*., 11, 1339−1353, doi:10.5194/acp-11-

1339-2011.

Shantz, N.C., W. R. Leaitch, P. F. Caffrey (2003), Effect of organics of low solubility on the growth rate of cloud droplets, *J. Geophys. Res*., 108, D54168, doi:10.1029/2002JD002540.

Shinozuka, Y., A. D. Clarke, P. F. DeCarlo, J. L. Jimenez, E. J. Dunlea, G. C. Roberts, J. M. Tomlinson, D. R. Collins, S. G. Howell, V. N. Kapustin, C. S. McNaughton, and J. Zhou (2009), Aerosol optical properties relevant to regional remote sensing of CCN activity and links to their organic mass fraction: airborne observations over central Mexico and the US west coast during MILAGRO/INTEX-B, *Atmos. Chem. Phys*., 9, 6727−6742, doi:10.5194/acp-9-6727-2009.

Shulman M. L., M. C. Jacobson, R. J. Carlson, R. E. Synovec, and T. E. Young (1996), Dissolution behavior and surface tension effects of organic dompounds in nucleating cloud droplets, *Geophys. Res. Lett.,* 23, 3, 277−280.

Sihto, S.-L., J. Mikkilä, J. Vanhanen, M. Ehn, L. Liao, K. Lehtipalo, P. P. Aalto, J. Duplissy, T. Petäjä, V.-M. Kerminen, M. Boy, and M. Kulmala (2011), Seasonal variation of CCN concentrations and aersol activation properties in boreal forest, *Atmos. Chem. Phys*., 11, 13269−13285, doi:10.5194/acp-11-13269-2011.

Sjogren, S., M. Gysel, E. Weingartner, U. Baltensperger, M.J.Cubison, H.Coe, A.A.Zadini, C.Marcolli, U.K.Krieger, and T.Peter (2007), Hygroscopic growth and water uptake kinetics of two-phase aerosol particles consisting of ammonium sulfate, adipic and humic acid mixtures, *Aerosol Science,38,* doi:10.1016/j.jaerosci.2006.11.005.

Slowik, J. G., K. Stainken, P. Davidovits, L. R. Williams, J. T. Jayne, C. E. Kolb, D. R. Worsnop, Y. Rudich, P. F. DeCarlo, and J. L. Jimenez (2004), Particle morphology and density characterization by combined mobility and aerodynamic diameter measurements, Part 2: Application to combustion-generated soot aerosols as a function of fuel equivalence ratio, *Aerosol. Sci. Technol.,* 38, 1206-1222, doi:10.1080/027868290903916.

Slowik, J. G., C. Stroud, J. W. Bottenheim, P. C. Brickell, R. Y.-W. Chang, J. Liggio, P. A. Makar, R. V. Martin, M. D. Moran, N. C. Shantz, S. J. Sjostedt, A. van Donkelaar, A. Vlasenko, H. A. Wiebe, A. G. Xia, J. Zhang, W. R. Leaitch, and J. P. D. Abbatt (2010), Characterization of a large biogenic secondary organic aerosol event from

eastern Canadian forests, *Atmos. Chem. Phys*., 10, 2825−2845, doi:10.5194/acp-10-2825-2010.

Song, C., R. A. Zaveri, M. L. Alexander, J. A. Thornton, S. Madronich, J. V. Ortega, A. Zelenyuk, X-Y. Yu., A. Laskin, and D. A. Maughan (2007), Effect of hydrophobic primary organic aerosols on secondary organic aerosol formation from ozonolysis of α-pinene, *Geophys. Res. Lett.,* 34, L20803, doi:10.1029/2007GL030720.

Spracklen, D. V., K. S. Carslaw, M. Kulmala, V-M. Kerminen, S-L. Sihto, I. Riipinen, J. Marikanto, G. W. Mann, M. P. Chipperfield, A. Wiedensohler, W. Birmmili, and H. Lihavainen (2008), Aerosol mass spectrometer constraint on the global secondary organic aerosol budget, *Geophys. Res. Lett.,* 35, L06808, doi:10.1029/2007GL033038.

Spracklen, D. V., J. L. Jimenez, K. S. Carslaw, D. R. Worsnop, M. J. Evans, G. W. Mann, Q. Zhang, M. R. Canagaratna, J. Allan, H. Coe, G. McFiggans, A. Rap, and P. Forster (2011), Aerosol mass spectrometer constraint on the global secondary organic aerosol budget, *Atmos. Chem. Phys*., 11, 12109−12136, doi:10.5194/acp-11-12109-2011.

Sun, Y., Q. Zhang, A. M. Macdonald, K. Hayden, S. M. Li, J. Liggio, P. S. K. Liu, K. G. Anlauf, W. R. Leaitch, A. Steffen, M. Cubison, D. R. Worsnop, A. van Donkelaar, and R. V. Martin (2009), Size-resolved aerosol chemistry on Whistler Mountain, Canada with a high-resolution aerosol mass spectrometer during INTEX-B, *Atmos. Chem. Phys*., 9, 3095−3111, doi:10.5194/acp-9-3095-2009.

Takeda, T., and N. Kuba (1982), Numerical study of the effect of CCN on the size distribution of cloud droplets, Part Ⅰ: Cloud droplets in the stage of condensation growth, *J.Metero.Soc. Japan*, 60, 978−993.

Takegawa, N., T. Miyakawa, Y. Kondo, J. L. Jimenez, Q. Zhang, D. R. Worsnop, and M. Fukuda (2006), Seasonal and diurnal variations of submicron organic aerosol in Tokyo observed using the Aerodyne aerosol mass spectrometer, *J. Geophys. Res*., 111, D11206, doi:10.1029/2005JD006515.

Takemura, T., T. Nozawa, S. Emori, T. Y. Nakajima, and T. Nakajima (2005), Simulation of climate response to aerosol direct and indirect effects with aerosol

transport-radiation model, *J.Geophys. Res*., 110, D02202, doi:10.1029/2004JD005029.

Tang, I. N., and H. R. Munkelwitz (1994), Water activities, densities, and refractive indices of aqueous sulfates and sodium nitrate droplets of atmospheric importance, *J. Geophys. Res.,* 99, 18801−18808.

Topping, D. O., and G. McFiggans (2012), Tight coupling of particle size, number and composition in atmospheric cloud droplet activation, *Atmos. Chem. Phys*., 12, 3253−3260, doi:10.5194/acp-12-3253-2012.

Tunved, P. et al. (2006), High Natural Aerosol Loading over Boreal Forests, *Science*, 312, 261−263.

Tritscher, T., Z. Jurányi, M. Martin, R. Chirico, M. Gysel, M. F. Heringa, P. F. DeCarlo, B. Sierau, A.S. H. Prévôt, E. Weingartner, and U. Baltensperger (2011), Changes of hygroscopicity and morphology during aging of diesel soot, *Environ. Res. Lett*., 6, 2011, 0434026, doi:10.1088/1748-9326/6/3/034026.

TSI Incorporated (2006), Model 3936 Scanning Mobility Particles Sizer^{TM} (SMPS^{TM}) Spectrometer, Operation and Service Manual, *P/N 1933796*, Revision L. Shoreview, Minn.

Twomey, S. A (1977), The influence of pollution on the shortwave albedo of clouds, *J. Atmos. Sci.,*34, 1149−1152.

VanReken, T. M., N. L. Ng, R. C. Flagan, and J. H. Seinfeld (2005), Cloud condensation nucleus activation properties of biogenic secondary organic aerosol, *J. Geophys. Res*., 110, D07206, doi:10.1029/2004JD005465.

Varutbangkul, V., F. J. Brechtel, R. Bahreini, N. L. Ng, M. D. Keywood, J. H. Kroll, R. C. Flagan, J. H. Seinfeld, A. Lee, and A. H. Goldstein (2006), Hygroscopicity of secondary organic aerosols formed by oxidation of cycloalkenes, monoterpenes, sesquiterpenes, and related compounds, *Atmos. Chem. Phys*., 6, 2367−2388, doi:10.5194/acp-6-2367-2006.

Vestin, A., J. Rissler, E. Swietlicki, G. P. Frank, and M. O. Andreae (2007), Cloud-nucleating properties of the Amazonian biomass burning aerosol: Cloud condensation nuclei measurements and modeling, *J. Geophys. Res*., 112, D14201, doi:10.1029/2006JD008104.

Volkamer, R., J. L. Jimenez, F. S. Martini, K. Dzepina, Q. Zhang, D. Salcedo, L. T.

Molina, D. R. Worsnop, and M. J. Molina (2006), Secondary organic aerosol formation from anthropogenic air pollution: Rapid and higher than expected, *Geophys. Res. Lett.,* 33, L17811, doi:10.1029/2006GL026899.

Wang, J., Y. –N. Lee, P. H. Daum, J. Jayne, and M. L. Alexander (2008), Effects of aerosol organics on cloud condensation nucleus (CCN) concentration and first indirect aerosol effect, *Atmos. Chem. Phys*., 8, 6325−6339, doi:10.5194/acp-8-6325-2008.

Wang, M. and J. E. Penner (2009), Aerosol indirect forcing in a global model with particle nucleation, *Atmos. Chem. Phys*., 9, 236−260, doi:10.5194/acp-9-239-2009.

Wang, J., M. J. Cubison, A.C. Aiken, J. L. Jimenez, and D. R. Collins (2010), The importance of aerosol mixing state and size-resolved composition on CCN concentration and the variation of the importance with atmospheric aging of aerosols, *Atmos. Chem. Phys*., 10, 7267−7283, doi:10.5194/acp-10-7267-2010.

Westervelt, D. M., J. R. Pierce, and P. J. Adams (2014), Analysis of feedbacks between nucleation rate, survival probability and cloud condensation nuclei formation, *Atmos. Chem. Phys*., 14, 5577−5597, doi:10.5194/acp-14-5577-2014.

Wex. H., F. Stratmann, D. Topping, and G. McFiggans (2008), The Kelvin versus the Raoult Term in the Kohler Equation, *J. Aerosol Sci*.,65, 4004−4016, doi:10.1175/2008JAS2720.1

Wex, H., M. D. Petters, C. M. Carrico, E. Hallbauer, A. Massling, G. R. McMeeking, L. Poulain, Z. Wu, S. M. Kreidenweis, and F. Stratmann (2009), Towards closing the gap between hygroscopic growth and activation for secondary organic aerosol: Part 1 – Evidence from measurements, *Atmos. Chem. Phys*., 9, 3987−3997, doi:10.5194/acp-9-3987-2009.

Wex, H., G. McFiggans, S. Henning, and F. Stratmann (2010), Influence of the external mixing state of atmospheric aerosol on derived CCN number concentrations, *Geophys. Res. Lett.,* 37, L10805, doi:10.1029/2010GL043337.

Wiedensohler, A., (1988), Technical Note: An Approximation of the Bipolar Charge Distribution for Particles in the Submicron Range, *J. Aero. Sci.,*19, 387−389.

Wittbom, C., A. C. Eriksson, J. Rissler, J. E. Carlsson, P. Roldin, E. Z. Nordin, P. T. Nilsson, E. Swietlicki, J. H. Pagels, and B. Svenningsson (2014), Cloud droplet activity changes of soot aerosol upon smog chamber ageing, *Atmos. Chem. Phys*., 14,

9831−9854, doi:10.5194/acp-14-9831-2014.

Wonaschuetz. A.,A. Sorooshian, B. Ervens, P. Y. Chuang, G. Feingold, S. M. Murphy, J. de Gouw, C. Warneke, and H. H. Jonsson (2012), Aerosol and gas re-distribution by shallow cumulus clouds: An investigation using airborne measurements, *J. Geophys. Res.*, 117, D17202, doi:10.1029/2012JD018089.

Wu, Z. J., L. Poulain, S. Henning, K. Dieckmann, W. Birmili, M. Merkel, D. van Pinxteren, G. Spindler, K. Müller, F. Stratmann, H. Herrmann, and A. Wiedensohler (2013), Relating particle hygroscopicity and CCN activity to chemical composition during the HCCT-2010 field campaign, *Atmos. Chem. Phys*., 13, 7983−7996, doi:10.5194/acp-13-7983-2013.

Yoshitomi. M, O. Wild, and H. Akimoto (2011), Contributions of regional and intercontinental transport to surface ozone in the Tokyo area, *Atmos. Chem. Phys*., 11, 7583−7599, doi:10.5194/acp-11-7583-2011.

Yu, F. and G. Luo (2009), Simulation of particle size distribution with a global aerosol model: contribution of nucleation to aerosol and CCN number concentrations, *Atmos. Chem. Phys*., 9, 7691−7710, doi:10.5194/acp-9-7691-2009.

Zaveri. R. A., J. C. Barnard, R. C. Easter, N. Riemer, and M. West (2010), Particle-resolved simulation of aerosol size, composition, mixing state, and the associated optical and cloud condensation nuclei activation properties in an evolving urban plume, *J. Geophys. Res*., 115, D17210, doi:10.1029/2009JD013616.

Zhang, Q. M. R. Canagaratna, J. T. Jayne, D. R. Worsnop, J-L. Jimenez (2005a), Time- and size-resolved chemical composition of submicron particles in Pittsburgh: Implications for aerosol sources and processes, *J. Geophys. Res*., 110, D07S09, doi:10.1029/2004JD004649.

Zhang, Q. D. R. Worsnop, M. R. Canagaratna, and J-L. Jimenez (2005b), Hydrocarbon-like and oxygenated aerosols in Pittsburgh: insights into sources and processes of organic aerosols, *Atmos. Chem. Phys*., 5, 3289−3311, doi:1680-7324/acp/2005-5-3289.

Zhang, Q., J. L. Jimenez, M. R. Canagaratna, J. D. Allan, H. Coe, I. Ulbrich, M. R. Alfarra, A. Takami, A. M. Middlebrook, Y. L. Sun, K. Dzepina, E. Dunlea, K. Docherty, P. F. DeCarlo, D. Salcedo, T. Onasch, J. T. Jayne, T. Miyoshi, A. Shimono, S. Hatakeyama, N. Takegawa, Y. Kondo, J. Schneider, F. Drewnick, S. Borrmann, S.

Weimer, K. Demerjian, P. Williams, K. Bower, R. Bahreini, L. Cottrell, R. J. Griffin, J. Rautiainen, J. Y. Sun, Y. M. Zhang, and D. R. Worsnop (2007), Ubiquity and dominance of oxygenated species in organic aerosols in anthropogenically-influenced Northern Hemisphere midlatitudes, *Geophys. Res. Lett.,* 34, L13801, doi:10.1029/2007GL029979.

Acknowledgments

I would like to thank Prof. Michihiro Mochida for providing an opportunity to do the research and giving a lot of valuable suggestions, and supporting research life on this study. I would also like to thank Dr. Tomoki Nakayama, Dr. Naomi Kuba, Dr. Yoko Iwamoto, and Dr. Yuemei Han for assisting field research and giving valuable comments for the research paper. I am grateful to laboratory members, Dr. Yoko Iwamoto, Dr. Toshiyuki Mihara, Dr. Yuemei Han, Mr. Akio Shigei, Ms. Saori Murase, Mr. Yoshitaka Setoguchi, Mr. QingCai Chen, Ms. Yange Deng, and Ms. Sara Kagami. I also thank Mr. Kazuji Suzuki for his technical support and all staffs in Wakayama Research Forest station for their cooperation of forest aerosol research. I acknowledge the Japan Meteorological Agency and the National Instistute for Environmental Studies for provising the data of meteorological conditions and the gaseous species in Nagoya. I also acknowledge the National Oceanic and Atmospheric Administration (NOAA) Air Resources Laboratory for using the HYbrid Single-Particle Lagrangian Integrated Trajectory (HYSPLIT) model. This study was supported partly by a Grant-in-Aid for Young Scientists (S) (20671001).